3

Basic theory of collisionless reconnection

3.1 Fundamentals of collisionless reconnection

J. F. Drake and M. A. Shay

There are a number of well-documented deficiencies of the present resistive MHD models of magnetic reconnection (Section 2.1) that have motivated the exploration of reconnection models based on either a two-fluid or a kinetic description: the long energy release time, the absence of a well-defined mechanism for breaking the frozen-in condition, the onset problem, and the particle heating problem. As discussed in Section 2.1, the Sweet–Parker model of reconnection yields an inflow velocity of plasma into the dissipation region given by

$$v_{\mathrm{in}} \sim (\delta/\Delta) v_{\mathrm{A}}, \tag{3.1}$$

where v_{A} is the Alfvén speed just upstream of the dissipation region and the width of the current layer, $\delta \sim \eta^{1/2}$, is small compared with its length Δ. In the Sweet–Parker model Δ is given by the macroscopic system size L. As a consequence, the rate of reconnection given in Eq. (3.1) is small. In contrast, in Petschek's model (Section 2.1), the outflow region from the X-line opens up as a fan, leaving a relatively short dissipation region Δ in Eq. (3.1), and therefore boosting the reconnection rate dramatically. However, computations revealed that the open Petschek outflow geometry cannot be sustained in a model with a simple uniform resistivity (Biskamp, 1986). A model resistivity that increases sharply in regions with high current density, such as might be expected from current-driven turbulence, facilitates a Petschek-like reconnection configuration (Sato and Hayashi, 1979). However, the establishment and role of such *anomalous resistivity* during reconnection is not yet well understood (Papadopoulos, 1977; Galeev and Sagdeev, 1984; Drake *et al.*, 2003; see also Section 3.5) in spite of the wide use of anomalous resistivity models in MHD computations. New insight into processes driving the macroscale Sweet–Parker current layer has been recently developed. This current layer reflects an underlying singularity in the post-reconnection MHD state (Waelbroeck, 1989; Jemella *et al.*, 2003, 2004). Mechanisms that suppress this tendency toward singularity must compete with the ideal MHD processes that create the singularity.

Changing the topology of magnetic field lines, which is necessary for releasing energy during magnetic reconnection, requires some form of dissipation to break the frozen-in condition. The dissipation mechanisms, which have been identified largely on the basis of computer simulations, will be discussed in greater detail in Sections 3.2

and 3.5. Section 3.2 focuses on mechanisms that operate even in the absence of modes that vary in the main current direction, while Section 3.5 discusses potential effects of such modes. In planetary magnetospheres such as that of the Earth, where the plasma density is only a few particles per cubic centimeter or less, the collisional mean free path is large enough that classical collisions are negligible. In the absence of collisions the finite mass of electrons limits their response to a parallel electric field and allows magnetic field lines to reconnect. In a generalized fluid model these finite mass effects take the form of electron inertia and a nondiagonal pressure tensor (Section 3.2). In the intense current layers that define the dissipation region, instabilities generated by the relative streaming of electrons and ions may drive turbulence sufficient to produce anomalous resistivity (Section 3.5). In the solar corona, where the plasma is much less tenuous, collisions may play a role in facilitating reconnection, especially during the early stages of reconnection. However, the fast release of magnetic energy observed in the corona produces inductive electric fields that typically exceed the Dreicer runaway field (Miller *et al.*, 1997). For typical reconnection electric fields corresponding to reconnection inflow velocities of $0.1v_{\mathrm{A}}$, with v_{A} the Alfvén speed, the runaway criterion becomes

$$v_{\mathrm{A}} > 10 v_{\mathrm{te}} \frac{\nu_{\mathrm{ei}}}{\Omega_{\mathrm{e}}}, \tag{3.2}$$

where v_{te} and Ω_{e} denote the electron thermal velocity and cyclotron frequency, respectively, and ν_{ei} is the electron–ion collision rate. When the runaway condition is satisfied, the local dynamics becomes effectively collisionless. Thus, understanding collisionless reconnection remains critical to modeling the dynamics of both solar and magnetospheric systems.

An essentially universal feature of magnetized plasma systems is the storage-release cycle (Chapter 1). Magnetic energy slowly builds up due to input from external drivers, remains essentially quiescent, possibly for long periods (hundreds to thousands of Alfvén times), and then abruptly releases through topological changes in the magnetic configuration facilitated by reconnection. In all systems in which magnetic reconnection can be studied in detail, including disruptions in laboratory fusion experiments, substorms in the Earth's magnetosphere, and solar and stellar flares, a similar cycle is observed yet the underlying reasons for this universal behavior remain unclear. Is there a common mechanism underlying the sudden onsets of magnetic reconnection in this variety of systems or is the commmonality of the observations merely accidental? Is the absence of progress on the reconnection onset problem because the MHD modeling of such systems is missing key physics?

There is strong evidence that a significant fraction of the magnetic energy released during magnetic reconnection is channeled into energetic electrons and ions. Solar observations in particular have suggested that at least 50% of the energy released during flares is in the form of energetic electrons (Lin and Hudson, 1971; Miller *et al.*, 1997). Energetic electrons and ions have been measured in the Earth's magnetosphere (Terasawa and Nishida, 1976; Baker and Stone, 1976) and in disruptions in laboratory fusion experiments (Savrukhin, 2001). Since MHD is a single fluid model, it cannot describe the energy branching ratio between electrons and ions nor can it describe the production of energetic particles, causing high-energy tails of the particle distributions (Section 3.6) that have been observed, for instance, in recent magnetotail satellite data (Øieroset *et al.*, 2002). Such heating processes can only be treated with kinetic models. The focus of this section is to introduce some of the non-MHD concepts that have emerged as dominant players in the dynamics of reconnection, including relevant spatial scales, to provide the basis for more detailed discussions in subsequent sections.

3.1.1 Basic kinetic processes and scales

The dynamics of magnetic reconnection is controlled by the dissipation region, the narrow boundary layer where dissipative processes allow the magnetic field to change topology. Understanding and modeling this layer has been challenging because collisions are typically weak and collisionless kinetic processes dominate. The intense currents driven by local electric fields can drive turbulence and nonlinear structures such as electron holes, solitary waves, and double-layers. In spite of these challenges significant progress has been made in identifying the dissipative mechanisms that break the frozen-in condition and the processes that control the structure of this layer (Section 3.2).

As outlined in Section 2.1, the aspect ratio of the dissipation region, the ratio of its width δ to its length Δ, controls the rate of reconnection based on the inflow–outflow condition in Eq. (3.1). In the MHD model δ is controlled by resistivity while Δ is linked to the macroscopic system scale length L, independent of the dissipation processes. A fundamental question is what physical processes control these scale lengths in a kinetic model. Specifically, what dissipative process controls the width of the dissipation region and what is the physics that determines the length of the dissipation region. If the length of the dissipation region remains macroscopic as in the MHD model, it is unlikely that even large values of the kinetic dissipation will be sufficient to raise the rate of reconnection to levels that can explain the observations.

An important yet perhaps unexpected result of the efforts to understand kinetic reconnection was the discovery that the motions of the electrons and ions, because of their very different masses, decouple at the small spatial scales defining the dissipation region (Sonnerup and Ledley, 1979; Mandt *et al.*, 1994; Horiuchi and Sato, 1994). This behavior can be understood from the electron equation of motion,

$$m_{\mathrm{e}}\frac{\mathrm{d}\mathbf{v}_{\mathrm{e}}}{\mathrm{d}t} = -e\mathbf{E} - e\mathbf{v}_{\mathrm{e}}\times\mathbf{B} - \frac{1}{n}\nabla\cdot\mathsf{P}_{\mathrm{e}} - m_{\mathrm{e}}\nu_{\mathrm{ei}}(\mathbf{v}_{\mathrm{e}}-\mathbf{v}), \tag{3.3}$$

where $\mathbf{v}$ is the bulk ion velocity, P_{e} is the electron pressure tensor (in the electron rest frame), and $\mathrm{d}/\mathrm{d}t \equiv \partial/\partial t + \mathbf{v}_{\mathrm{e}}\cdot\nabla$ is the time derivative in the electron rest frame. This equation appears like an Ohm's law if $\mathbf{v}_{\mathrm{e}}$ is replaced with $\mathbf{v}_{\mathrm{e}} = \mathbf{v} - \mathbf{j}/ne$ and terms of order $m_{\mathrm{e}}/m_{\mathrm{i}}$ are neglected,[1]

$$\frac{m_{\mathrm{e}}}{ne^2}\left[\frac{\partial\mathbf{j}}{\partial\mathbf{t}} + \nabla\cdot\left(\mathbf{jv}+\mathbf{vj}-\frac{\mathbf{jj}}{ne}\right)\right] = \mathbf{E}+\mathbf{v}\times\mathbf{B} - \frac{\mathbf{j}\times\mathbf{B}}{ne} + \frac{\mathbf{1}}{ne}\nabla\cdot\mathsf{P}_{\mathrm{e}} - \eta\mathbf{j}. \tag{3.4}$$

---

[1] The $\mathbf{jj}$ term on the left-hand side of (3.4) can be combined with the electron pressure term to yield the electron pressure tensor in the plasma rest frame, $\mathsf{P}_{\mathrm{e}}^{\mathrm{CM}}$, which leads to

$$\frac{m_{\mathrm{e}}}{ne^2}\left[\frac{\partial\mathbf{j}}{\partial\mathbf{t}} + \nabla\cdot(\mathbf{jv}+\mathbf{vj})\right] = \mathbf{E}+\mathbf{v}\times\mathbf{B} - \frac{\mathbf{1}}{ne}\mathbf{j}\times\mathbf{B} + \frac{\mathbf{1}}{ne}\nabla\cdot\mathsf{P}_{\mathrm{e}}^{\mathbf{CM}} - \eta\mathbf{j}.$$

This is the form discussed by Vasyliūnas (1975).

The *generalized* Ohm's law (3.4) contains three terms that are not present in the resistive MHD limit, the electron inertia term on the left of (3.4), and the terms proportional to $\mathbf{j}\times\mathbf{B}$ (*Hall term*) and $\nabla\cdot\mathbf{P}_\mathrm{e}$. The Hall term brings whistler dynamics into the system while the electron pressure term brings in kinetic Alfvén wave dynamics and unmagnetized electron dynamics when the pressure tensor is nongyrotropic.

At large spatial scales Eq. (3.4) reduces to $\mathbf{E}+\mathbf{v}\times\mathbf{B}=0$, the ideal MHD "Ohm's" law. From this relation it is easily shown that the magnetic field is frozen-in to the ion fluid (Section 2.2). The ideal MHD equations are scale invariant, meaning that they do not define a spatial scale. The other terms in Ohm's law are associated with specific spatial scales and are important when those spatial scales are reached. The electron inertial term is associated with the electron skin depth $d_\mathrm{e}\equiv c/\omega_\mathrm{pe}$, which can be derived by comparing the convective portion of the inertia term with the $\mathbf{j}\times\mathbf{B}$ term. At the spatial scales where electron inertia is important typically $v_\mathrm{e}\gg v$ so that the $\nabla\cdot(\mathbf{jj}/ne)$ portion of the inertia dominates. The scale where the $\mathbf{j}\times\mathbf{B}$ (Hall) term becomes important is calculated by comparing it with the $\mathbf{v}\times\mathbf{B}$ term,

$$|\mathbf{v}\times\mathbf{B}|\sim v_\mathrm{A}\mathbf{B}<\frac{|\mathbf{j}\times\mathbf{B}|}{ne}\sim\frac{\mathbf{1}}{\mu_0 ne}\frac{B^2}{\Delta} \tag{3.5}$$

or

$$\Delta<d_\mathrm{i}\equiv c/\omega_\mathrm{pi}. \tag{3.6}$$

If Δ is smaller than the ion inertial length d_i, j/ne exceeds v so that v_e exceeds v, which implies that electrons and ions no longer move together, unlike in the MHD regime, where $\mathbf{v}_\mathrm{e}\sim\mathbf{v}$. The isotropic pressure term brings in the effective ion Larmor scale $\rho_\mathrm{s}=(T_\mathrm{e}/m_\mathrm{i})^{1/2}/\Omega_\mathrm{i}$ (based on the *ion–sound speed*, $v_\mathrm{s}=(T_\mathrm{e}/m_\mathrm{i})^{1/2}$ for the limit where $T_\mathrm{e}\gg T_\mathrm{i}$). Since this scale does not follow from Ohm's law alone, we discuss this scale later.

The decoupling of electron and ion motion at small spatial scales implies that the Alfvén wave no longer controls the collective behavior of the plasma motion below these scales. In particular, the Alfvén wave no longer drives the acceleration of the plasma away from the X-line, allowing the bent, newly reconnected field lines to release their stored magnetic energy. Close to the X-line this role is taken over by either the whistler or kinetic Alfvén wave.

The issue of what breaks the frozen-in condition is of fundamental importance for the understanding of collisionless reconnection. The details of this mechanism will be discussed in Section 3.2. Very close to the X-line the convective portion of the inertial term can be neglected because the local velocity is nearly zero (from symmetry considerations) so only the nongyrotropic pressure can balance the reconnection electric field (Vasyliūnas, 1975). This result is true both with and without a guide magnetic field (the field component in the direction of the main current), which implies that the current layer driven by the reconnection electric field must scale with the electron Larmor radius even when the guide field becomes very large (Hesse *et al.*, 2002, 2004). Away from the X-line the convective portion of the inertia can be important, especially for the case with a guide field, where large parallel electric fields map the magnetic separatrices, extending outward far from the X-line (Pritchett and Coroniti, 2004; Drake *et al.*, 2005b).

A final question is how strongly the rate of reconnection depends on the dissipation mechanism. An important result of the *GEM Reconnection Challenge* (Birn *et al.*, 2001) and some earlier papers (Shay and Drake, 1998; Hesse *et al.*, 1999) is that the rate of late-time reconnection is insensitive to dissipation when whistler and kinetic Alfvén waves drive the outflow from the X-line. For simplicity, we break the more detailed discussion of these various issues into the case of antiparallel and guide-field (component) reconnection.

Reconnection with antiparallel magnetic fields

The case of antiparallel reconnection has been extensively explored because of its relevance to collisionless reconnection in the Earth's magnetotail and because the current layers that develop in the vicinity of the X-line are relatively broad in comparison with the case of a guide field and therefore computationally less challenging to model. In Fig. 3.1 is a schematic of the basic structure of the X-line region, including the field structure and electron and ion flows. At distances greater than d_i upstream from the X-line the electrons and ions flow together. At a distance around d_i upstream the electron and ion motion decouples and the ions are diverted into the outflow direction, forming an outflow jet and current layer of width around d_i. Inside of this region the ions are essentially demagnetized and respond mostly to electric rather than magnetic fields. The electrons remain frozen-in to the magnetic field and continue to move toward the X-line. The electrons decouple from the magnetic field when they approach within d_e of the X-line and are accelerated in the outflow direction in an outflow channel of width d_e. The peak outflow velocity of the electrons

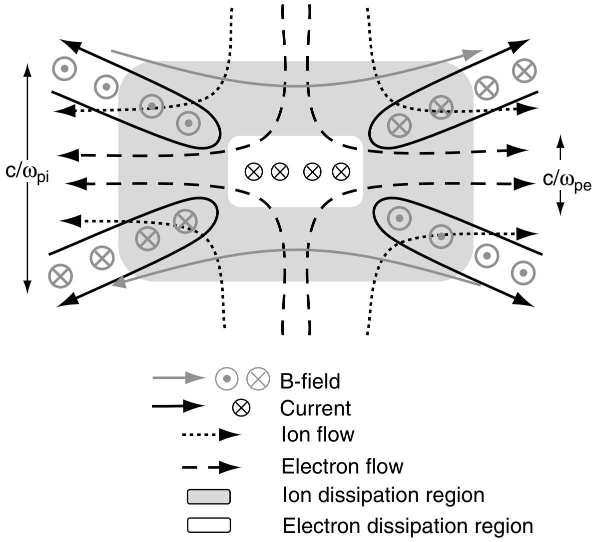

Fig. 3.1. Schematic of the multiscale structure of the dissipation region during antiparallel reconnection. Electron (ion) dissipation region in white (gray) with scale size c/ω_pe (c/ω_pi). Electron (ion) flows in long (short) dashed lines. In-plane currents marked with solid dark lines and associated out-of-plane magnetic quadrupole field in gray.

reaches the electron Alfvén speed $v_{\mathrm{Ae}} = B/\sqrt{\mu_0 m_{\mathrm{e}} n}$ and then drops sharply to match the ion outflow speed v_{A}. The different trajectories of the electrons and ions in the reconnection plane produce closed current loops that generate a self-consistent out-of-plane magnetic field B_y. This field is the signature of the standing whistler wave that drives the electron outflow from the X-line.

For consistency with the remainder of this chapter, and the predominant applications to the Earth's magnetotail (Chapter 4), we adopt a cartesian coordinate system, where x is the coordinate in the direction of the main magnetic field, which reverses sign across the current sheet, y is the direction of the main current (the ignorable coordinate in 2D models), and z is the direction perpendicular to the current sheet. We note that these coordinates may differ from those in the original papers cited.

Shown in Fig. 3.2 are data from a 2D simulation of antiparallel reconnection with a particle-in-cell (PIC) code (Zeiler *et al.*, 2002). The data are consistent with the schematic shown in Fig. 3.1. A key discovery that is manifest in all models that include the Hall term in Ohm's law is that the dissipation region (broadly defined to include all of the regions where either the ions or electrons decouple from the magnetic field) remains spatially localized in the outflow direction – that is, unlike the Sweet–Parker model, the dissipation region is determined by the kinetic scales ($\Delta \sim 10 d_{\mathrm{i}}$) rather than the macroscale L. It is this scaling for Δ that facilitates fast reconnection ($v_{\mathrm{in}} \sim 0.1\, v_{\mathrm{A}x}$) from Eq. (3.1) even in large systems (Shay *et al.*, 1999, 2004; Huba and Rudakov, 2004). The reason for the different scaling of the Hall versus the MHD reconnection is linked to the dispersive character of the whistler wave (Rogers *et al.*, 2001). The insensitivity of the rate of reconnection to dissipation is also linked to the dispersive property (Birn *et al.*, 2001). Thus, how reconnection couples to the whistler wave is a crucial scientific issue.

Coupling to whistler waves The coupling of dispersive waves to reconnection is complicated by the 2D structure of the dissipation region and there has to date been no rigorous analytical model to describe the essential physics. A good qualitative understanding can be gleaned from a simple 1D picture as illustrated in Fig. 3.3, showing the magnetic field of a standing wave that is periodic in the z direction along a uniform magnetic field in the y and z directions. As suggested by the magnetic field line segments shaded dark, a segment of the field line can be treated as a newly reconnected field line formed as a result of reconnection and the resulting flow in the x direction treated as a proxy for the outflow generated during reconnection. In the case of the MHD model the solution of this standing Alfvén wave is

$$\tilde{B}_x = \tilde{B}_0 \sin(kz)\cos(kv_{\mathrm{p}}t), \tag{3.7}$$

$$\tilde{v}_x = v_{\mathrm{p}} \frac{\tilde{B}_0}{B_z} \cos(kz)\sin(kv_{\mathrm{p}}t), \tag{3.8}$$

$$v_p = v_{\mathrm{A}z}, \tag{3.9}$$

with v_{p} the wave phase speed. The amplitude of the x component of the velocity, $\tilde{B}_0/\sqrt{\mu_0 m_{\mathrm{i}} n}$, is simply the upstream Alfvén velocity, the usual outflow condition for magnetic reconnection. A similar calculation carried out with $B_y = 0$ at

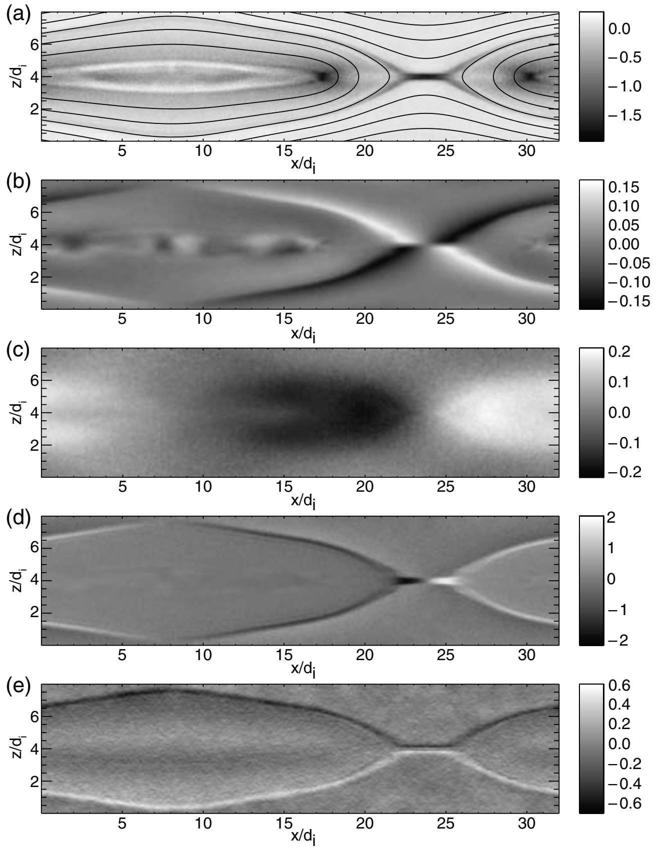

Fig. 3.2. Data from a PIC simulation of antiparallel reconnection with $m_\mathrm{i}/m_\mathrm{e} = 100$, $T_\mathrm{i}/T_\mathrm{e} = 12.0$, and $c = 20.0$ showing: (a) the current J_z and in-plane magnetic field lines; (b) the self-generated out-of-plane field B_z; (c) the ion outflow velocity v_x; (d) the electron outflow velocity $v_{x\mathrm{e}}$; and (e) the Hall electric field E_y. Noticeable are the distinct spatial scales of the electron and ion motions, the substantial value of B_z which is the signature of the standing whistler, and the strong Hall electric field, E_y, which maps the magnetic separatrix. The overall reconnection geometry reflects the open outflow model of Petschek rather than the elongated current layers of Sweet–Parker.

scales below d_i yields the fields for the whistler wave and the electron outflow velocity,

$$\tilde{B}_y = \tilde{B}_0 \sin(kz)\cos(kv_\mathrm{p}t), \tag{3.10}$$

$$v_\mathrm{p} = kd_\mathrm{e}v_{\mathrm{Ae}z}, \tag{3.11}$$

where $\tilde{B}_x$ and $\tilde{v}_x$ are the same as in Eqs. (3.7) and (3.8) with the whistler phase speed replacing that of the Alfvén wave. The whistler wave generates a magnetic field $\tilde{B}_y$ as the electron flow $\tilde{v}_{y\mathrm{e}}$ drags the field $\tilde{B}_x$ out of the reconnection plane (Terasawa, 1983; Hassam, 1984). Associated with $\tilde{B}_y$ is the electron outflow $\tilde{v}_x$, which drives the electrons away from the X-line. Thus, the whistler wave replaces the Alfvén wave in

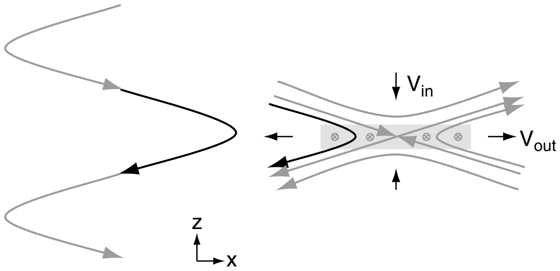

Fig. 3.3. Schematic showing how a newly reconnected field line can be represented as a segment of a simple 1D wave. The horizontal velocity v_x generated as the wave evolves corresponds to the outflow velocity from the reconnection site. The ratio of the peak horizontal velocity v_x to the horizontal magnetic field perturbation B_x is a constant in the case of the Alfvén wave but depends on the wave vector k_z in the case of whistler and kinetic Alfvén waves and is related to the dispersive property of these waves.

driving reconnection (Mandt *et al.*, 1994) and the characteristic outflow speed is the whistler phase speed based on the upstream magnetic field $\tilde{B}_0$.

Importantly, for a given value of $\tilde{B}_0$ the outflow velocity increases with k (see Eqs. (3.8) and (3.11)) or inversely with the width of the dissipation region δ. This is very different from reconnection driven by the Alfvén wave. A consequence is that the total flux of electrons from the dissipation region $n\tilde{v}_x$ is insensitive to δ and therefore the mechanism that breaks the frozen-in condition. The implication of this result is that the rate of reconnection should also not depend on the mechanism that breaks the frozen-in condition. Computer simulations of reconnection support this hypothesis (Shay and Drake, 1998; Hesse *et al.*, 1999; Birn *et al.*, 2001). In Fig. 3.4 we show results from the GEM Reconnection Challenge project (Birn *et al.*, 2001), in which the reconnected flux is shown as a function of time for a series of simulations with an MHD model, a Hall MHD model (including the $\mathbf{j}\times\mathbf{B}$ and $\nabla\cdot\mathbf{P}_e$ terms in Ohm's law), a hybrid model (massless, fluid electrons and particle ions), and a PIC model. All of the models but MHD include the dynamics of whistlers and the runs were carried out with identical Harris equilibria with finite initial field perturbations. The rate of reconnection is the slope of the curve of reconnected flux. All models but MHD have indistinguishable rates of reconnection, which greatly exceed the MHD rate (obtained with uniform resistivity corresponding to a Lundquist number of 200). Since the mechanism that breaks the frozen-in condition in the various models differs (finite electron mass in the case of the PIC simulation and a hyper-resistivity in the other non-MHD models) these simulations confirm the insensitivity of the rate of reconnection to the dissipation mechanism if dispersive whistlers are included in the dynamics.

The GEM challenge did not address the question how the thin current sheet and the initial island were formed. Therefore, another collaborative study was performed to address this question (Birn *et al.*, 2005). This study grew out of a workshop on Magnetic Reconnection Theory, held in 2004 at the Isaac Newton Institute, Cambridge, UK, and was therefore dubbed the *Newton Challenge*. The simulations started from a current sheet that was four times thicker, in relation to the ion inertia

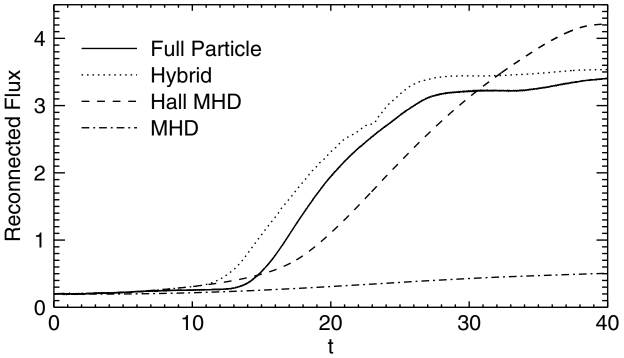

Fig. 3.4. Reconnected magnetic flux as function of time for various simulations of the GEM Reconnection Challenge project (Birn *et al.*, 2001), including an MHD model, a PIC model, a hybrid model, and a Hall MHD model, using the same initial conditions and parameters. The slope of the curves is the reconnection rate and is essentially the same for all models that include the Hall term (whistler dynamics).

length, than that in the GEM challenge, and current sheet thinning and the onset of fast reconnection was initiated by temporally limited, spatially varying inflow of magnetic flux. The simulations showed again fast reconnection, independent of the dissipation mechanism, when the Hall/whistler dynamics was included, consistent with the GEM study. Further evidence comes from PIC simulations where it has also been shown that the rate of reconnection is insensitive to the value of the electron mass (Shay and Drake, 1998; Hesse *et al.*, 1999; Pritchett, 2001b; Ricci *et al.*, 2002).

Thus, the dispersive property of the whistler, which controls the outflow of electrons from the dissipation region in antiparallel reconnection, renders reconnection insensitive to the mechanism that breaks the frozen-in condition. This result has the desirable consequence that the details of a kinetic model might not be required to model reconnection in large systems.

Structure of the electron dissipation region In the case of reconnection with no initial guide field the electron dissipation region is the narrow region around the reversal region where the electrons become demagnetized and decouple from the magnetic field. The width δ_e of this demagnetized electron region can be obtained using the conservation of canonical momentum, $p_y = m_\mathrm{e} v_y - eB'_x z^2/2c$, and energy, where $B'_x = \mathrm{d}B_x/\mathrm{d}z$. For a typical particle with the thermal velocity v_te,

$$\delta_\mathrm{e} = \sqrt{\frac{2v_\mathrm{te}}{\Omega'_{\mathrm{e}x}}}, \tag{3.12}$$

which is a hybrid of the electron Larmor radius based on the asymptotic magnetic field and the magnetic scale length $L_B = B_x/B'_x$ (Laval *et al.*, 1966). This expression, however, does not pin down the characteristic scale of the dissipation region because both the magnetic scale length and possibly the thermal velocity have to be determined self-consistently. For example, even if the inflowing electrons are very cold, the dissipation region is still expected to have a finite scale. The self-consistent scaling can be determined by requiring that the electrons bouncing in the unmagnetized region balance the magnetic pressure and at the same time requiring that the current carried by the electrons within the dissipation region generate the jump in magnetic field across the layer. These two conditions, $B_x^2/2\mu_0 = m_\mathrm{e} n v_\mathrm{b}^2/2$ and $\delta_\mathrm{e} v_\mathrm{b} = d_\mathrm{e} v_{\mathrm{A}\mathrm{e}x}$, yield the width of the current layer δ_e and the electron bounce velocity v_b in the dissipation region,

$$\delta_\mathrm{e} = d_\mathrm{e}, \tag{3.13}$$

$$v_\mathrm{b} = v_{\mathrm{Ae}x}, \tag{3.14}$$

where the electron Alfvén velocity $v_{\mathrm{Ae}x}$ should be evaluated just upstream of the electron current layer. This width is consistent with the data shown in Fig. 3.2. Note that the width of the electron current layer is independent of the magnetic field jump across the layer. If the electron thermal velocity of the inflowing plasma exceeds the electron Alfvén speed, the layer will be broader than in Eq. (3.13) so d_e is the minimum value of the width of the electron dissipation region. Simulations reveal that the minimum width is actually around $2d_\mathrm{e}$ (Zeiler *et al.*, 2002).

How the electrons trapped in the unmagnetized region reach velocities as high as the electron Alfvén speed is not obvious. The inflow velocity associated with reconnection is a small fraction of $v_{\mathrm{Ae}x}$ and is therefore not the driver. This inner electron region develops a substantial electric field E_z due to excess electrons at the turning points of their bounce motion in the unmagnetized region. This field points outward from the neutral line and accelerates the electrons into the unmagnetized region, producing the counterstreaming electron beams that make up distribution function at the X-line (Zeiler *et al.*, 2002; Swisdak *et al.*, 2005). Thermal spreading blurs the fine-scale structure of this layer when the electron thermal velocity approaches the electron Alfvén speed.

With the width of the dissipation region given in Eq. (3.13), an estimate of the electron outflow velocity from the electron dissipation region can be obtained. Equations (3.8) and (3.11) yield $k \sim 1/d_\mathrm{e}$ so that

$$\tilde{v}_{\mathrm{e}x} \sim v_{\mathrm{Ae}x}. \tag{3.15}$$

The scaling of the electron outflow velocity with the electron Alfvén speed was demonstrated in 2D hybrid simulations by varying the electron mass (Shay *et al.*, 2001). Outflow velocities consistent with this scaling have also been measured in full particle simulations (Hoshino *et al.*, 2001a).

Reconnection with a guide field

The introduction of an ambient magnetic field in the out-of-plane direction (the *guide field*), along the current direction, substantially changes the structure of the dissipation region even at rather low values of the guide field. With this additional magnetic field the out-of-plane inductive electric field that drives reconnection has a component parallel to the magnetic field and the resulting parallel acceleration of electrons produces strong out-of-plane currents, in contrast to the cross-field currents that dominate the antiparallel reconnection dynamics. The in-plane components of the parallel electron flows along newly reconnected field lines drive a pronounced density asymmetry across the reconnection layer that couples reconnection to a kinetic Alfvén wave (Aydemir, 1992; Kleva *et al.*, 1995; Cafaro *et al.*, 1998). Thus, it is the kinetic Alfvén wave that drives the electron outflow from the X-line rather than the whistler. The guide field also suppresses the unmagnetized bounce motion of electrons that defines the width of the electron current layer in the antiparallel reconnection case. The result is that the electron current layer narrows substantially and surprisingly has a width that scales with the electron Larmor radius (Hesse *et al.*, 2002, 2004). A consequence is that the nongyrotropic behavior of electrons survives even when the guide field is large (see Section 3.2).

Coupling to kinetic Alfvén waves In Fig. 3.5 we show the out-of-plane current density j_y, the electron density $n_{\rm e}$, and the parallel electric field from a simulation with an ambient guide field equal to the reversed field. Clearly seen in the plot of the density is the depletion of the density along two of the separatrices and enhancements along the remaining separatrices (Tanaka, 1996; Pritchett and Coroniti, 2004; Drake *et al.*, 2005). This density asymmetry is the signature of the kinetic Alfvén wave. A diagram showing the essential physics appears in Fig. 3.6 (Kleva *et al.*, 1995). A parallel electric field on newly reconnected field lines drives a parallel electron flow across the current layer, depleting the electron density on one side of the current layer and enhancing it on the other. The resulting electric field causes the ions to polarization drift across the current layer to charge neutralize the electrons. A surprise is the magnitude of the electron density depletion, which yields cavity densities as low as a few percent of the ambient background. The separatrix with the enhanced density in Fig. 3.5 carries most of the current and the result is a distinct twist of the current layer that is in contrast with the distinctly symmetric layer in the case of zero guide field. The perturbations of the kinetic Alfvén wave can be calculated as in the case of no guide field,

$$\tilde{B}_y = \sqrt{\mu_0 n T}\,\frac{\tilde{B}_0}{B_y}\sin(kz)\sin(kv_{\rm p}t), \tag{3.16}$$

$$v_{\rm p} = kd_{\rm e}\frac{B_z}{B}c_{\rm se}, \tag{3.17}$$

$$\tilde{n}T = -B_y\tilde{B}_y, \tag{3.18}$$

where $c_{\rm se} = \sqrt{T/m_{\rm e}}$ is the electron sound speed. As in the case of the whistler and Alfvén waves the outflow velocity $\tilde{v}_x$ is given in Eq. (3.8) but with the phase speed given in Eq. (3.17). In the case of a strong guide field the flow speeds are below the magnetosonic speed so the density and out-of-plane magnetic field perturbations are in pressure balance as given in Eq. (3.18). As in the case of the whistler wave, the kinetic Alfvén wave speed increases as the layer width decreases for a fixed value of the upstream magnetic field $\tilde{B}_0$. While there have been no reported scaling studies of the electron outflow velocity in the case of guide-field reconnection, the phase speed of the wave in Eq. (3.17) suggests that the outflow speed should scale with the electron sound speed.

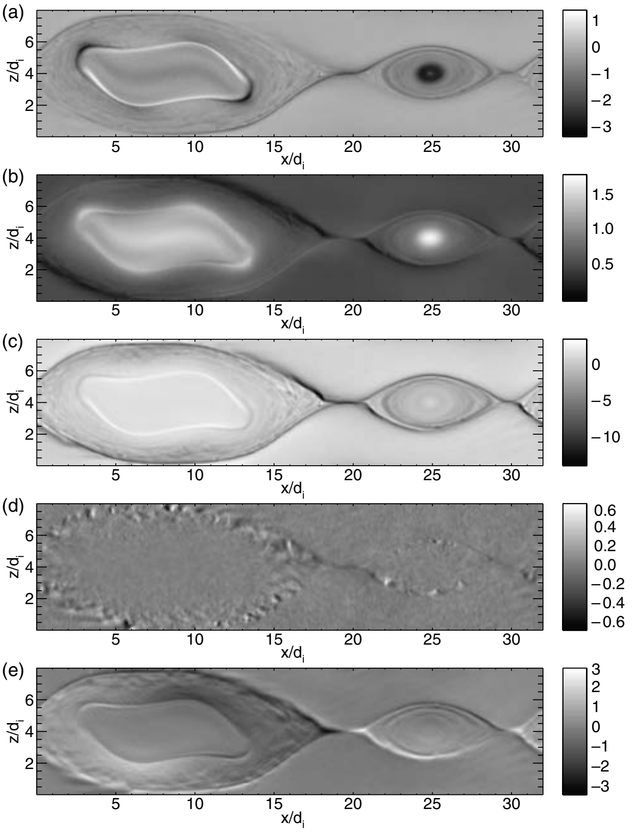

Fig. 3.5. Data from a PIC simulation of reconnection with a guide field (initially uniform) equal in magnitude to the reversed field. Other parameters are $m_{\mathrm{i}}/m_{\mathrm{e}} = 100$, $T_{\mathrm{i}}/T_{\mathrm{e}} = 12.0$, and $c = 20.0$. Shown are: (a) the current density j_y; (b) the electron density; (c) the electron parallel velocity $v_{\|\mathrm{e}}$; (d) the parallel electric field $E_{\|}$; and (e) the Hall electric field E_z. Noticeable are the canting and narrowing of the current layer at the X-line compared with the antiparallel case in Fig. 3.2, the density cavities that map two of the four separatrices connected to the X-line, the localization and structuring of the parallel electric field in the low-density cavities, the large parallel electron velocities that are a conseqence of acceleration by the parallel electric field in the low-density cavities, and the strong transverse Hall electric fields that maintain charge neutrality in the density cavities. The density asymmetry across the dissipation region reflects the coupling to the kinetic Alfvén wave. The development of the secondary magnetic island is typical during reconnection with a guide field.

Based on the simple 1D wave model, the values of the guide field and plasma β where the dispersive whistler and kinetic Alfvén waves dominate the dynamics of the inner dissipation region or where there are no dispersive waves have been identified (Rogers *et al.*, 2001). A detailed computational exploration remains to be completed.

An important remaining question is how large the guide field has to be in order to magnetize the electrons in the dissipation region and therefore impact the dynamics

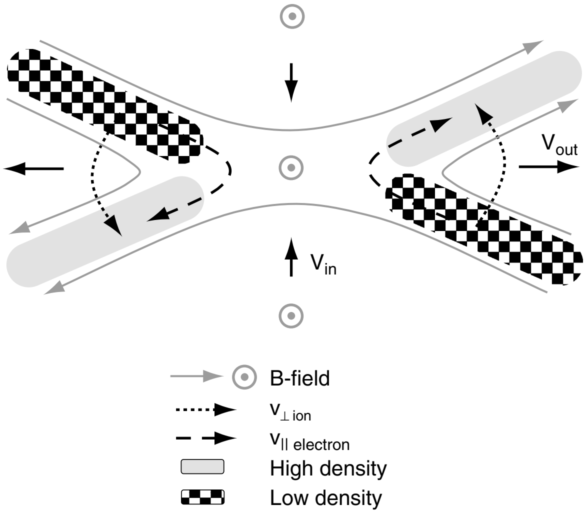

Fig. 3.6. Schematic of the structure of the dissipation region during reconnection with a guide field. Compression of parallel electron flows on newly reconnected field lines leads to a density asymmetry across the dissipation region in contrast to the symmetric system with no guide field. Ions polarization drift across the magnetic field to charge neutralize the electrons.

from that in an ideal system with no guide field. The dynamics of the antiparallel system should significantly change if the ambient guide field is sufficient to magnetize electrons injected into the reversal region. The inflow velocity of electrons is around $0.1v_{\mathrm{A}ex}$ – that is, around 0.1 of the outflow velocity of the electrons. The effective Larmor radius ρ_{g} of electrons with this velocity in the guide field is $\rho_{\mathrm{g}} = 0.1v_{\mathrm{A}ex}/\Omega_{\mathrm{e}y}$, where $\Omega_{\mathrm{e}y} = eB_y/m_{\mathrm{e}}$ is the cyclotron frequency in the guide field. The condition $\rho_{\mathrm{g}} < d_{\mathrm{e}}$ yields

$$B_y > 0.1B_x \tag{3.19}$$

as the condition for which the guide field can no longer be neglected in *antiparallel* reconnection (Swisdak *et al.*, 2005). Thus, only very small guide fields are required to alter the electron dynamics. We emphasize that much larger guide fields are required to alter the dynamics of ions.

Structure of the parallel electric field and the electron dissipation region In the absence of a guide field the electron dissipation region has a width that is comparable to the electron skin depth. A guide field can prevent the bounce motion of electrons across the current layer that controls the dynamics in the antiparallel field case, resulting in even narrower current layers. The electron dissipation region in the case of a guide field is controlled by the parallel electron current and therefore the parallel electric field. This parallel field is given approximately by

$$E_{\|} = -\partial A_y/\partial t - \nabla_{\|}\Phi, \tag{3.20}$$

where A_y is the y component of the vector potential that defines the in-plane magnetic field $\nabla A_y \times \hat{y}$, and $\nabla_{\|}\Phi$ is the parallel component of the electrostatic field. The latter is generated due to the parallel bunching of electrons. At a location where the in-plane magnetic field reverses, the parallel electrostatic field vanishes ($\nabla_{\|}\Phi = 0$) and reconnection generates a finite parallel electric field. The structure of Φ controls the spatial localization of $E_{\|}$. If the charge perturbation associated with electron parallel bunching can be balanced by the cross-field motion of either the electrons or ions, the parallel electric field can remain nonzero. Otherwise the electrostatic field cancels the inductive field and the electrons short out the parallel reconnection electric field (Drake and Lee, 1977). The electrons satisfy a kinetic equation based on drift orbits given by

$$\frac{\partial \tilde{f}}{\partial t} + v_{\|}\nabla_{\|}\tilde{f} + \frac{f_0}{B\Omega_{\mathrm{e}}}\frac{\mathrm{d}}{\mathrm{d}t}\nabla_{\perp}^2\Phi + \frac{e}{m_{\mathrm{e}}}E_{\|}\frac{\partial f_0}{\partial v_{\|}} = 0, \tag{3.21}$$

where $f(\mathbf{x}, v_{\perp}, v_{\|}) = f_0 + \tilde{f}$ is the distribution function and the third term arises from the polarization drift. Because the electron layer is typically much smaller than an ion Larmor radius, the ion response to the potential must include the full ion orbital dynamics. Only the motion perpendicular to the magnetic field must be included. The ion density perturbation, $\tilde{n}_{\mathrm{i}}$, is given by

$$\tilde{n}_{\mathrm{i}} = [\Gamma_0(b) - 1]\frac{e\Phi}{T_{\mathrm{i}}}n_0, \tag{3.22}$$

$$\Gamma_0(b) = I_0(b)e^{-b}, \qquad b = -\rho_{\mathrm{i}}^2\partial^2/\partial z^2, \tag{3.23}$$

where $\rho_{\mathrm{i}} = \sqrt{T_{\mathrm{i}}/m_{\mathrm{i}}}/\Omega_{\mathrm{i}}$ is the ion Larmor radius and I_0 is the modified Bessel function. Equating this density perturbation with that of the electrons by solving Eq. (3.21), we find an equation for the potential as follows:

$$\nabla_{\|}H\Phi = -\frac{T_{\mathrm{i}}}{T_{\mathrm{e}} + T_{\mathrm{i}}}E_{\|}(0) + \frac{T_0}{n_0 e}\int \mathrm{d}v_{\|}\nabla_{\|}\tilde{h}, \tag{3.24}$$

$$\left(\frac{\partial}{\partial t} + v_{\|}\nabla_{\|}\right)\tilde{h} = \frac{e}{T_{\mathrm{e}}}f_0\dot{E}_{\|}, \tag{3.25}$$

where

$$\nabla_{\|}\tilde{h} \equiv \nabla_{\|}\tilde{f} + \frac{ef_0}{T_{\mathrm{e}}}\left(E_{\|} + \rho_{\mathrm{e}}^2\nabla_{\|}\frac{\partial^2\Phi}{\partial z^2}\right), \tag{3.26}$$

$$H = \Gamma_0\frac{T_0}{T_{\mathrm{i}}} - 1 + \rho_{\mathrm{e}0}^2\frac{\partial^2}{\partial z^2}, \tag{3.27}$$

$$T_0 = \frac{T_{\mathrm{e}}T_{\mathrm{i}}}{T_{\mathrm{e}} + T_{\mathrm{i}}}, \qquad \rho_{\mathrm{e}0}^2 = T_0\rho_{\mathrm{e}}^2/T_{\mathrm{e}}, \tag{3.28}$$

and $\rho_{\mathrm{e}0}$ is the effective electron Larmor radius based on the hybrid temperature T_0. The operator H in Eq. (3.27) controls the response of the potential Φ to the parallel inductive electric field. The spatial structure of the parallel electric field therefore is controlled by this operator and the basic scales involved can be deduced from its zeros. Taking $\partial/\partial z \sim 1/\delta$ the zeros of H yield two distinct scales δ: the effective electron Larmor radius $\rho_{\mathrm{e}0}$ based on the hybrid temperature T_0; and the effective ion Larmor radius $\rho_{\mathrm{s}} = \sqrt{T_{\mathrm{e}}}/m_{\mathrm{i}}$. Earlier models of reconnection with a guide field had suggested that the transverse scale of $E_\|$ was the ion scale ρ_{s}, which is inconsistent with recent simulations (Hesse *et al.*, 2002, 2004; Swisdak *et al.*, 2005) that suggest that the parallel electric field is much more localized with a transverse scale given by the electron Larmor radius.

The structure of $E_\|$ can be deduced from Eqs. (3.24) and (3.25). For simplicity we consider simple linear tearing perturbations for which $\nabla_\| = ik_x z B_x'/B_y$. At $z=0$ the $\tilde{h}$ term in Eq. (3.25) balances the inductive drive term but for $z \gtrsim \rho_{\mathrm{e}0}$, $\tilde{h} \to 0$ and $\rho_{\mathrm{e}0}^2 \partial^2/\partial z^2 \ll 1$. Since $\Gamma_0 \sim 0$ at scales below the ion Larmor radius, we find that $\nabla_\| \Phi \sim eq - (T_{\mathrm{i}}/(T_{\mathrm{i}} + T_{\mathrm{e}}))\dot{A}_y/c$ or

$$E_\| = E_\|(0)\frac{T_{\mathrm{e}}}{T_{\mathrm{i}} + T_{\mathrm{e}}}. \tag{3.29}$$

For $T_{\mathrm{i}} \gg T_{\mathrm{e}}$ the parallel electric field has dropped to a small fraction of its value at $z=0$. $E_\|$ remains approximately constant at this level until $z \gtrsim \rho_{\mathrm{s}}$ when $\Gamma_0 \sim 1$ and $\nabla_\| \phi \sim eqE_\|(0)$ so that $E_\| \sim eq0$. Earlier theories in which $E_\|$ remained constant out to ρ_{s} were valid only in the limit of zero ion temperature. In most space physics applications $T_{\mathrm{i}} \gg T_{\mathrm{e}}$ so the tranverse scale of $E_\|$ is effectively $\rho_{\mathrm{e}0}$.

This analysis of the transverse structure of $E_\|$ does not provide information about the structure of $E_\|$ along the magnetic field. For example, after reconnection has approached quasi-steady conditions in a large system, what is the spatial extent of the region where $E_\| = 0$? Is this region localized to the X-line or does it extend large distances along the magnetic separatrices? The spatial extent of this region impacts the number of electrons that can be accelerated by the parallel electric field during magnetic reconnection and therefore the fraction of energy transferred from the magnetic field into electrons, a broadly important issue in essentially all reconnection applications.

The spatial extent of $E_\|$ is controlled by the dynamics of the standing kinetic Alfvén wave that is driven in the vicinity of the X-line. The deep density cavities produced along two of the four separatrices emanating from the X-line shown in Fig. 3.5 are regions where the reconnection electric field can maintain a finite $E_\|$ that extends a significant distance from the X-line (Pritchett and Coroniti, 2004). This is because the very low density of these cavities makes it more difficult for electrons to bunch and short out the parallel electric field. The spatial extent of $E_\|$ is therefore linked to the spatial extent of the density cavities. The cavities are formed as electrons approach the separatrix and are accelerated toward the X-line by the parallel electric field. The high parallel mobility of these low-mass particles allows the electric field to nearly evacuate the separatrix. The limit on the length of these density cavities has been linked to the upper limit on the in-plane current that results from the flow of electrons toward the X-line – that is, longer cavities require more current for their formation (Drake *et al.*, 2005). The in-plane current produces a self-consistent field $\tilde{B}_y$ whose pressure must be balanced by depressions in the local pressure and in-plane magnetic field. The result is an upper limit on the length $L_{\rm c}$ of the cavities and a corresponding upper limit on the electron velocity $v_{\|}$ that results from parallel acceleration in these cavities,

$$L_{\rm c} = 5d_{\rm i}(1+\beta_x)B_x/B_y, \tag{3.30}$$

$$v_{\|} = \alpha\frac{(1+\alpha^2/4c^2)^{1/2}}{1+\alpha^2/2c^2}, \tag{3.31}$$

$$\alpha \equiv v_{{\rm Ae}x}(1+\beta_x)^{1/2}, \quad \beta_x = n(T_{\rm e}+T_{\rm i})/B_x^2. \tag{3.32}$$

The energetic beams that are produced in these acceleration cavities are injected into the X-line so that the total current driven at the X-line during reconnection with a guide field is not just a result of local acceleration but is a more complex nonlocal process. The high-velocity beams produced in these acceleration cavities can also generate fluctuations over a broad range of frequencies (Cattell *et al.*, 2005). The impact of these fluctuations on the electron beams and reconnection remains an ongoing research topic. Can, for example, the electron-ion drag induced by these fluctuations compete with the nongyrotropic pressure in balancing the reconnection electric field at the X-line during steady reconnection?

3.1.2 Scaling of kinetic reconnection to macroscale systems

A second important result of the kinetic modeling concerns the scaling of the dissipation region with the system size. As discussed earlier, the reconnection rate is strongly dependent on the aspect ratio of the dissipation region, δ/Δ as defined in Eq. (3.1). In the Sweet–Parker model the dissipation region has a length that scales with the macroscopic system length L (Section (2.1)) and the small aspect ratio, δ/Δ leads to slow reconnection. In contrast, in Petschek's model, slow shocks bound the plasma flowing away from the X-line and are responsible for the outflow acceleration. Since in this model most of the outflowing plasma does not need to pass through the dissipation region, the length of the dissipation region Δ can be small compared with the system size, and according to Eq. (3.1) this allows for an enormous increase in the reconnection rate. Flux conservation through the slow shocks yields $v_{\rm in}\sim v_{\rm out}\tan\theta\sim v_{{\rm A}x}\theta$, where θ is the angle that the slow shocks make with the x axis. Comparing this relation with Eq. (3.1), we find that the opening angle of the outflow is directly related to the aspect ratio of the dissipation region.

While this open geometry does not appear in uniform-resistivity MHD models (Biskamp, 1986), it does appear in all of the models that couple to dispersive waves in the dissipation region (Shay *et al.*, 1999; Rogers *et al.*, 2001; Shay *et al.*, 2004). Why does wave dispersion allow the outflow region to open up as proposed by Petschek? The opening process is shown in Fig. 3.7 in a time sequence of the out-of-plane current from a numerical simulation of the transition from Sweet–Parker to Hall reconnection. The out-of-plane current is directly linked to the ion acceleration away from the X-line (via $\mathbf{j}\times\mathbf{B}$ force) and provides a good visualization tool for the reconnection geometry. In this simulation a system with steady Sweet–Parker reconnection was taken as an initial condition. The resistivity was reduced so that the width of the Sweet–Parker dissipation region fell below $d_{\rm i}$. The transition was then triggered as the outflow jet opened sharply and the corresponding rate of reconnection increased.

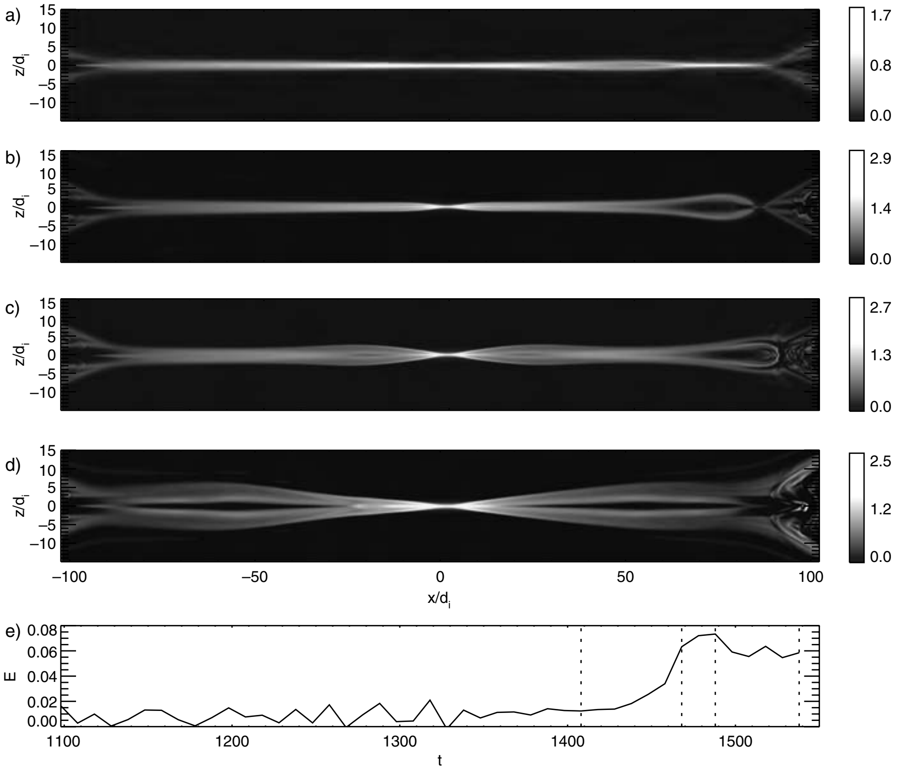

Fig. 3.7. Transition from Sweet–Parker to Hall reconnection. From a double current sheet simulation with system size $409.6c/\omega_{\mathrm{pi}} \times 204.8c/\omega_{\mathrm{pi}}$. Initially the system has a resistivity, or inverse Lundquist number, of $\eta = 0.015$ (based on a normalization using the length scale c/ω_{pi} and the time scale $1/\Omega_{\mathrm{ci}}$). At $t = 1098$, the resistivity is lowered to 0.007. In (a)–(d) the total current along y as time progresses and in (e) the reconnection electric field versus time. The time of each figure in (a)–(d) is denoted by a dashed vertical line in (e). Figure provided by Paul Cassak.

Again, a rigorous theory of the connection between the X-line and the Petschek outflow solution has not been carried out but the essential physics of this transition can be understood from arguments similar to those used to analyze the outflow from the 1D waves. Instead of a simple 1D system depending only on z, we consider an initial condition with slow variation in the x direction corresponding to an open outflow geometry. Taking x to be the distance downstream of the X-line, $B_z \sim x$, $\tilde{B}_0 \sim x$ and the width of the outflow region $\delta \sim x$ so that $k \sim x^{-1}$. Through the incompressibility condition $\nabla \cdot \mathbf{v} = 0$ the x variation of the outflow velocity $\tilde{v}_x$ with distance from the X-line controls the contraction or expansion of the outflow jet in the z direction. If $\tilde{v}_x$ increases with x, then $\partial \tilde{v}_z / \partial z < 0$ and the outflow jet will constrict, reducing the rate of reconnection. On the other hand, if $\tilde{v}_x$ decreases with x, the outflow jet will expand into the Petschek open outflow configuration. Along the symmetry line $z = 0$ the outflow velocity scales like $v_{\mathrm{p}} \sin(k v_{\mathrm{p}} t)$ so the variation of the phase speed $v_{\rm p}$ with distance x controls the structure of the outflow jet. In the MHD case $v_{\rm p} \sim x$ so that

$$\partial \tilde{v}_z / \partial z < 0 \tag{3.33}$$

and the outflow jet contracts in the z direction as was seen in earlier MHD simulations (Uzdensky and Kulsrud, 2000). In the case of whistler driven outflow $v_{\rm p}$ is a constant and $\tilde{v}_x$ decreases with x so that

$$\partial \tilde{v}_{z{\rm e}} / \partial z > 0. \tag{3.34}$$

In this case the outflow jet expands in the z direction as shown in Fig. 3.7 and leads to the open outflow configuration of Petschek and fast reconnection.

Thus, in the case of the whistler the increase of the width of the outflow jet and the increase of the magnetic field with distance downstream counterbalance so that the whistler phase speed is nearly constant, allowing the outflow jet to remain open. This behavior is, of course, linked to the dispersive property of the whistler.

The simulations performed showing this open outflow geometry via Hall physics are quite small compared to the actual physical systems which exhibit reconnection such as the solar corona and the Earth's magnetosphere. It is therefore important to show that the length of the dissipation region Δ is independent of system size L. Even a weak dependence can cause an extreme slowdown of reconnection when extrapolated to real systems. For the antiparallel case, a study using hybrid simulations of the double tearing mode yielded reconnection inflow velocities of $0.1 v_{\rm A}$ with no dependence on system size (Shay *et al.*, 1999). Recently, this result has been confirmed with two-fluid simulations of a system with open boundary conditions (Huba and Rudakov, 2004). The independence of the rate of reconnection from system size can be visualized in Figs. 3.7c and d. In these figures, the angle θ that the open current wedge makes with the x axis is established locally around the X-line and then propagates outwards. By the time of Fig. 3.7d, this wedge of current has propagated about 1/2 of the total system size, with no appreciable change in the angle θ. The angle θ, therefore, is set up locally at the X-line, independent of system size.

Reconnection rates on the order of $0.1 v_{\rm A}$ yield time scales for global energy release and magnetic reconfiguration that are consistent with those seen in solar flares and magnetospheric substorms. In a typical X-class flare, reconnection drives a global energy release, in the form of hard and soft X-ray emissions that last around 100 seconds. With rough estimates of the magnetic field and density in the solar corona ($B \approx 100\,{\rm G}$ and $n \approx 10^{10}\,{\rm cm}^{-3}$), the reconnection inflow velocity is around $2 \cdot 10^7\,{\rm cm/s}$. A typical magnetic flux tube involved in a flare has an area of $10^{18}\,{\rm cm}^2$ and a length of $10^9\,{\rm cm}$, giving a time of 50 s to reconnect much of the magnetic field in the flux tube, which is consistent with the duration of typical flares (Miller *et al.*, 1997). During a substorm, a significant fraction of magnetotail lobe flux is reconnected causing a massive dipolarization of the magnetotail. Typical values of lobe properties ($B \approx 15\,{\rm nT}$ and $n \approx 0.05\,{\rm cm}^{-3}$) yield a reconnection inflow speed of 150 km/s. In around 10 minutes, a typical time scale for the expansion phase of a substorm, about 15 $R_{\rm E}$ of magnetic flux in the lobes can reconnect.

The results that the reconnection rate is insensitive to system size and electron dissipation are not without controversy. The above results have been questioned in studies of forced reconnection and double tearing mode reconnection, where it has been found that either the reconnection rate or the time scales of reconnection have a dependence on electron dissipation and system size ($d_{\rm i}/L$ and $\rho_{\rm s}/L$) (Grasso *et al.*, 1999; Wang *et al.*, 2001; Porcelli *et al.*, 2002; Fitzpatrick, 2004; Bhattacharjee *et al.*, 2005). An example will be discussed in Section 3.4. Some of the disparities may arise from differences in the definition of the reconnection time – whether or not to include the initiation phase when the island width $w \sim d_{\rm i}, \rho_{\rm s}$ – or from the difficulty in identifying weak dependencies, such as a 1/6-th power electron mass dependence discussed in Section 3.4. It is also not clear to what extent simulations with contrasting results cover identical regimes of the evolution. More studies with $w \gg d_{\rm i}, \rho_{\rm s}$ will be necessary to settle this question.

3.1.3 Transitions from slow to fast reconnection

The structure and rate of reconnection in the collisional MHD model differ drastically from that of the Hall reconnection model. An important question is how systems with finite resistivity undergoing reconnection transition between the two states. Do the rates of reconnection change continuously between the two regimes or is there a sharp transition? Is the transition related to the observed onset of reconnection, e.g., in the onset of solar flares or of sawtooth events in laboratory tokamak experiments? In the environment of the Earth's magnetosphere this issue is probably of less importance because of the absence of resistivity.

For a given plasma resistivity, rather general arguments suggest that there are two stable solutions (fast and slow) to the reconnection problem for a given value of the plasma resistivity (Cassak *et al.*, 2005). The Sweet–Parker solution, governing slow reconnection, is valid provided the half-width of the current layer δ exceeds the relevant kinetic scale lengths,

$$\frac{\delta}{L} = \sqrt{\frac{\eta}{\mu_0 v_{\rm A} L}} > \frac{d_{\rm i}}{L}, \frac{\rho_{\rm s}}{L}, \tag{3.35}$$

where the magnetic field is to be evaluated immediately upstream of the current layer. For the antiparallel reconnection case, this reduces to

$$\frac{\eta_{\rm sf}}{\mu_0} \sim \frac{v_{\rm A} d_{\rm i}^2}{L}, \tag{3.36}$$

so Sweet–Parker reconnection is valid for $\eta > \eta_{\rm sf}$. For example, in the solar corona, $n \sim 10^{16}\,{\rm m}^{-3}$, $L \sim 10^7\,{\rm m}$ and $B \sim 10^{-2}\,{\rm T}$ (Miller *et al.*, 1997), so $\eta_{\rm sf} \sim 10^{-6}\,{\rm ohm/m}$ in MKS units, corresponding to a temperature of $10^2\,{\rm eV} \sim 10^6\,{\rm K}$.

The converse condition, that resistivity be sufficiently small to not impact the whistler or kinetic Alfvén dynamics that drive kinetic reconnection, yields a distinct condition. As in the Sweet–Parker analysis, we balance resistive diffusion with convection at the electron inertial scale $d_{\rm e}$,

$$\frac{\eta_{\rm fs}}{\mu_0 d_{\rm e}^2} \sim \frac{v_{\rm in,e}}{d_{\rm e}} \sim 0.1 \frac{v_{\rm Ae}}{d_{\rm e}},$$

or

$$\frac{\eta_{\rm fs}}{\mu_0} \sim 0.1 v_{\rm A} d_{\rm i}, \tag{3.37}$$

with $v_{\rm A}$ evaluated upstream of the electron current layer. The fast reconnection solution is valid if $\eta < \eta_{\rm fs}$. The value of $\eta_{\rm fs}$ is independent of system size and is enormous for most physical systems. Equation (3.37) suggests that once fast reconnection onsets, resistive effects are unlikely to influence the dynamics.

In typical systems of interest the ratio of $\eta_{\rm sf}$ to $\eta_{\rm fs}$ is very small,

$$\frac{\eta_{\rm sf}}{\eta_{\rm fs}} \sim 10 \frac{d_{\rm i}}{L} \ll 1, \tag{3.38}$$

because $d_{\rm i} \ll L$ for most systems of physical interest. For example, the ratio in Eq. (3.38) is 10^{-6} for the data from the solar corona presented earlier. Thus, transitions from fast to slow reconnection occur at much higher resistivities than the reverse, so for a large range of resistivity $\eta_{\rm sf} < \eta < \eta_{\rm fs}$ there are two stable solutions to the reconnection problem.

These theoretical predictions were tested with numerical simulations using a two-fluid code (Cassak *et al.*, 2005). The electron to ion mass ratio was $m_{\rm e}/m_{\rm i} = 1/25$. For a $409.6 d_{\rm i} \times 204.8 d_{\rm i}$ computational domain, the critical resistivities are $\eta'_{\rm sf} \sim 0.01$ and $\eta'_{\rm fs} \sim 0.03$, where $\eta' = \eta/\mu_0 v_{\rm A} d_{\rm i}$ is the normalized resistivity. Larger systems would produce greater separations of $\eta_{\rm sf}$ and $\eta_{\rm fs}$. Shown in Fig. 3.8 are plots of the out-of-plane plasma current from two quasi-steady reconnection simulations of the two-fluid equations. The upper (lower) simulation has a normalized reconnection rate $E' = E/(v_{\rm A} B) = 0.055$ (0.014), corresponding to the fast (slow) reconnection solution. At the time shown both of these simulations have identical parameters: $\eta' = 0.015$. The separate solutions were obtained through differing initial conditions: the slow solution being initialized with resistive initial conditions (adding the Hall terms after

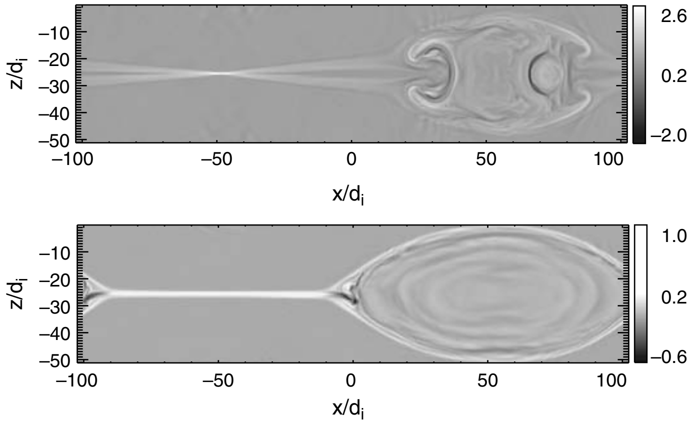

Fig. 3.8. Current density j_y for fast (upper panel) and slow (lower panel) reconnection solutions for a resistivity $\eta' = 0.015$. The parameters of the two runs are identical and each solution remains stable until all of the available flux has reconnected.

a transient initial period); and the fast solution being initialized as collisionless (no resistivity but subsequently including it). The range of resistivity over which there are dual reconnection solutions is apparent in Fig. 3.9, where the reconnection rates and current layer widths are shown versus plasma resistivity. The solid (open) circles correspond to the resistive (collisionless) initial conditions. The range of dual solutions matches well the theoretical estimates. The important result is that the slow solution disappears when the width of the Sweet–Parker current layer falls below d_i and at this point the rate of reconnection abruptly increases. Since the Sweet–Parker reconnection rate decreases with the system size L but the fast rate is independent of L, the jump in the rate of reconnection will be enormous for large-scale systems such as the solar corona. From the condition for the disappearance of the Sweet–Parker solution in Eq. (3.35), a reduction of the local resistivity or an increase in the local Alfvén velocity can trigger the transition. The upstream Alfvén velocity typically increases with time as large magnetic fields convect into the X-line during reconnection so this model yields a clear mechanism for the transition from slow to fast reconnection. Possible applications of such an onset model are the solar corona and disruptions in tokamak fusion experiments. Because of the absence of collisional resistivity in the Earth's magnetosphere, this model cannot explain onset in this system.

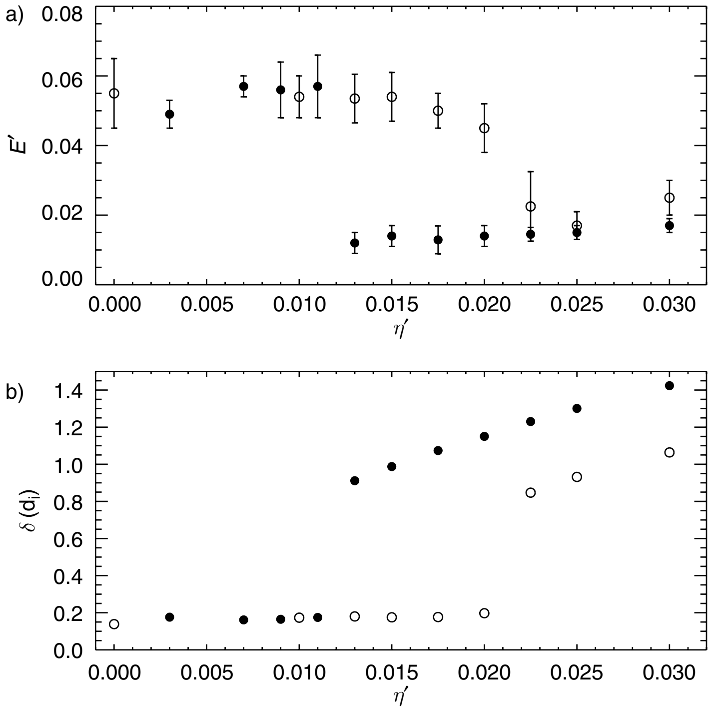

Fig. 3.9. (a) Normalized reconnection rate, $E' = E/Bv_\mathrm{A}$ and (b) current sheet width, δ, as a function of normalized resistivity, $\eta' = \eta/\mu_0 v_\mathrm{A} d_\mathrm{i}$, for runs analogous to those in Fig. 3.8.

3.2 Diffusion region physics

M. Hesse

As discussed in Sections 2.1 and 3.1, in standard resistive MHD models the structure of the reconnection site is characterized by a resistive diffusion region, where dissipation is governed by the Ohmic term ηj^2, embedded in a wide, essentially dissipation-free, region governed by ideal MHD. In the collisonless regime the structure and the dissipation mechanism become more complicated, as illustrated schematically in Fig. 3.1. This is most easily demonstrated by the generalized Ohm's law, derived from the equation of motion of the electron fluid (3.3)

$$\mathbf{E} = -\mathbf{v}_\mathrm{e} \times \mathbf{B} - \frac{1}{ne}\nabla \cdot \mathbf{P}_\mathrm{e} - \frac{m_\mathrm{e}}{e}\left(\frac{\partial \mathbf{v}_\mathrm{e}}{\partial t} + \mathbf{v}_\mathrm{e} \cdot \nabla \mathbf{v}_\mathrm{e}\right), \tag{3.39}$$

where now the ion–electron collision term is neglected. Again, the pressure tensor is defined in the rest frame of the electrons. Joule dissipation is generally defined by $\mathbf{j} \cdot \mathbf{E}'$, where $\mathbf{E}' = \mathbf{E} + \mathbf{v} \times \mathbf{B}$ is the electric field in the plasma rest frame. Since the first term on the right-hand side (RHS) of (3.39) can also be expressed approximately by $-\mathbf{v} \times \mathbf{B} + \mathbf{j} \times \mathbf{B}/ne$ (assuming one singly charged ion species, for simplicity), and the Hall term, $\mathbf{j} \times \mathbf{B}$, does not contribute to the dissipation, it is obvious that the dissipation mechanism must rely on either thermal, i.e., pressure-based (second term on the RHS of Eq. 3.39), or inertial effects (last term on the RHS of Eq. 3.39). Of these, the pressure-based dissipation might rely on current-aligned pressure gradients, or, in regions of sufficiently small magnetic field, on nongyrotropies of the distribution function (Vasyliūnas, 1975; Lyons and Pridmore-Brown, 1990; Hesse and Winske, 1993).

We should note that equations equivalent to (3.39) hold self-consistently for all plasma species, so that, in principle, dissipation could also be derived from the ion pressure and inertia terms. However, these terms are approximately balanced by the Lorentz force $\mathbf{j} \times \mathbf{B}$, so that the net dissipation is given by very small differences between large ion terms, which are in fact related to electron effects. Therefore it is much better to discuss the dissipation directly on the basis of the electron terms.

Owing to its very small size and to a lack of sufficiently fast plasma measurements, the properties of the electron diffusion region have not been clearly identified in spacecraft observations. Thus the physics of the dissipation region remained a mystery until very recently when highly sophisticated computer simulations of collisionless plasmas permitted the study of electron effects. In this section we present an overview of our present understanding of how particles become demagnetized in the diffusion region of the reconnection process. The emphasis of the discussion will be on electrons; however, many results apply equally to ions, after a suitable change of charge and mass. The section focuses primarily on the thermal- or bulk-inertia-based dissipation processes that have been validated in a large number of numerical models.

The structure of this section follows the historical evolution of theoretical research of the diffusion region. Following an introduction of the base model for most simulations in Section 3.2.1, we discuss antiparallel magnetic reconnection in Section 3.2.2. Section 3.2.3 presents an analysis of our present knowledge of guide-field magnetic reconnection, which is arguably the more generic of the two cases. Both sections include summaries of translationally invariant and fully three-dimensional models.

3.2.1 The model and initial configuration

Most of the results presented in this overview are based on the application of particle-in-cell codes. The system studied by many researchers is similar to that selected in the GEM reconnection challenge (Birn *et al.*, 2001). This system is described in the following.

In most of our analysis we employ dimensionless quantities. For this purpose, we normalize densities by a typical density n_0 in the current sheet, and the magnetic field by the asymptotic value of the reconnection magnetic field B_0. Ions are assumed to be protons (mass m_p) throughout, and length scales are normalized by the ion inertial length c/ω_pi, where the ion plasma frequency $\omega_\mathrm{pi} = \sqrt{e^2 n_0/\varepsilon_0 m_\mathrm{p}}$ is evaluated for the reference density. Velocities are measured in units of the ion Alfvén velocity $v_\mathrm{A} = B_0/\sqrt{\mu_0 m_\mathrm{p} n_0}$, based on the reference magnitudes of magnetic field and density. The electric field is measured in units of $E_0 = v_\mathrm{A} B_0$, the pressure in units of $p_0 = B_0^2/\mu_0$, and the current density is normalized to $j_0 = \omega_\mathrm{pi} B_0/c\mu_0$.

The magnetic field represents a modified Harris sheet (Harris, 1962) of the following form:

$$B_x = \tanh(2z) + a_0\pi/L_z \cos(2\pi x/L_x)\sin(\pi z/L_z), \tag{3.40}$$

$$B_z = -a_0 2\pi/L_z \sin(2\pi x/L_x)\cos(\pi z/L_z). \tag{3.41}$$

The perturbation amplitude $\mathrm{a}_0 = 0.1$ leads to an initial value of the normal magnetic field of about 3% of B_0. The system size matches that of the GEM reconnection challenge by $\mathrm{L}_x = 25.6$ and $\mathrm{L}_z = 12.8$. In addition, we here employ a constant magnetic field component directed along the main current flow,

$$B_y = B_{y0}, \tag{3.42}$$

where B_{y0} is the initial value of the guide field magnitude. The choice of ion–electron mass ratio varies for different studies; it ranges from $m_\mathrm{i}/m_\mathrm{e} = 25$ in the original GEM challenge problem to $m_\mathrm{i}/m_\mathrm{e} = 1836$ in some recent implicit particle-in-cell calculations (Ricci *et al.*, 2002).

The system evolution is modeled by particle-in-cell codes similar to the one used by Hesse *et al.* (1999). Particle orbits are calculated in the electromagnetic fields, and the electromagnetic fields are integrated on a two- or three-dimensional grid.

3.2.2 Antiparallel reconnection

Previous analyses of time-dependent magnetic reconnection (Hewett *et al.*, 1988; Horiuchi and Sato, 1994, 1997; Pritchett, 1994; Hesse *et al.*, 1995; Tanaka, 1995b,a; Cai and Lee, 1997; Hesse and Winske, 1998; Kuznetsova *et al.*, 1998; Shay and Drake, 1998; Hesse *et al.*, 1999; Shay *et al.*, 1999; Hoshino *et al.*, 2001a,b) have begun to shed light on the electron behavior in different parameter regimes, primarily in the regions of low magnetic field. It was found that, for antiparallel magnetic reconnection, deviations from gyrotropy in the electron distribution function can give rise to reconnection electric fields via nongyrotropic electron pressure terms

$$E_y = -\frac{1}{n_e e}\left(\frac{\partial P_{xy}}{\partial x} + \frac{\partial P_{yz}}{\partial z}\right). \tag{3.43}$$

This process can be understood as an inertial effect of thermal electrons which bounce in the field reversal region. It is therefore equivalent to a *thermal inertia* effect, i.e., a mechanism by which particle thermal motion rather than bulk fluid inertia balances the reconnection electric field. This bounce motion was first described by Horiuchi and Sato (1994). Hesse and Winske (1998) performed a particle-in-cell simulation of collisionless reconnection in the GEM geometry. Their analysis showed indeed the presence of electron pressure nongyrotropies near the X-point. The magnitude of these tensor components proved to be sufficient to provide the reconnection electric field via the expression (3.39).

These studies were taken a step further by Hesse *et al.* (1999), who investigated the effect of different electron masses on the collisionless dissipation process in the reconnection region. The target of the investigation was to study whether different physics in the diffusion region might lead to different dissipation, thereby influencing and potentially changing the larger scale behavior of the system under investigation. In order to test the dependence of the reconnection process on the assumed electron mass, Hesse *et al.* (1999) performed a set of simulations with varying ion/electron mass ratio, ranging from $m_i/m_e = 9$ to $m_i/m_e = 100$. Figure 3.10 shows the magnetic field evolution for the run with $m_i/m_e = 25$ with the current density in gray scale. The figure shows that magnetic reconnection, initiated by the initial perturbation, causes large changes of the magnetic field and current density distribution. Figure 3.10 demonstrates two features: The current sheet thickness in the reconnection region is, at all times, somewhat larger than the electron skin depth, and the current density exhibits a saddle-point at the location of the reconnection region. The latter feature becomes most prominent at later times. Similar features were also found in hybrid and particle simulations of a similar system.

The relevant off-diagonal components of the pressure tensor are shown in Fig. 3.11, for a PIC simulation using an ion–electron mass ratio of $m_i/m_e = 256$ (M. Hesse, unpublished). This figure demonstrates that electron pressure nongyrotropies are found even for large mass ratios. Similar results were also found by Pritchett (2001b).

It is apparent from the discussion above that the processes responsible for these electron pressures rely on the inertia of individual electrons, which contributes to all of the fluid terms on the RHS of Eq. (3.39). Heavier electrons should spend more time in the region of low magnetic field, leading to more acceleration and thus stronger reconnection electric fields. Intuitively, one might expect that the electron mass should have a significant impact on the evolution of the system. Figure 3.12 proves that this expectation is essentially incorrect. Figure 3.12 shows, for each of the runs described above, the time evolution of the reconnected magnetic flux, defined by

$$F_{\text{rec}} = \int_{\text{X}-\text{O}} B_z \mathrm{d}x, \tag{3.44}$$

where the integral is taken between the major X- and O-points, if there are more than one of each. Each graph consists of an initial slow growth, typically for the first seven to eight ion cyclotron times, followed by a rapid time evolution. After

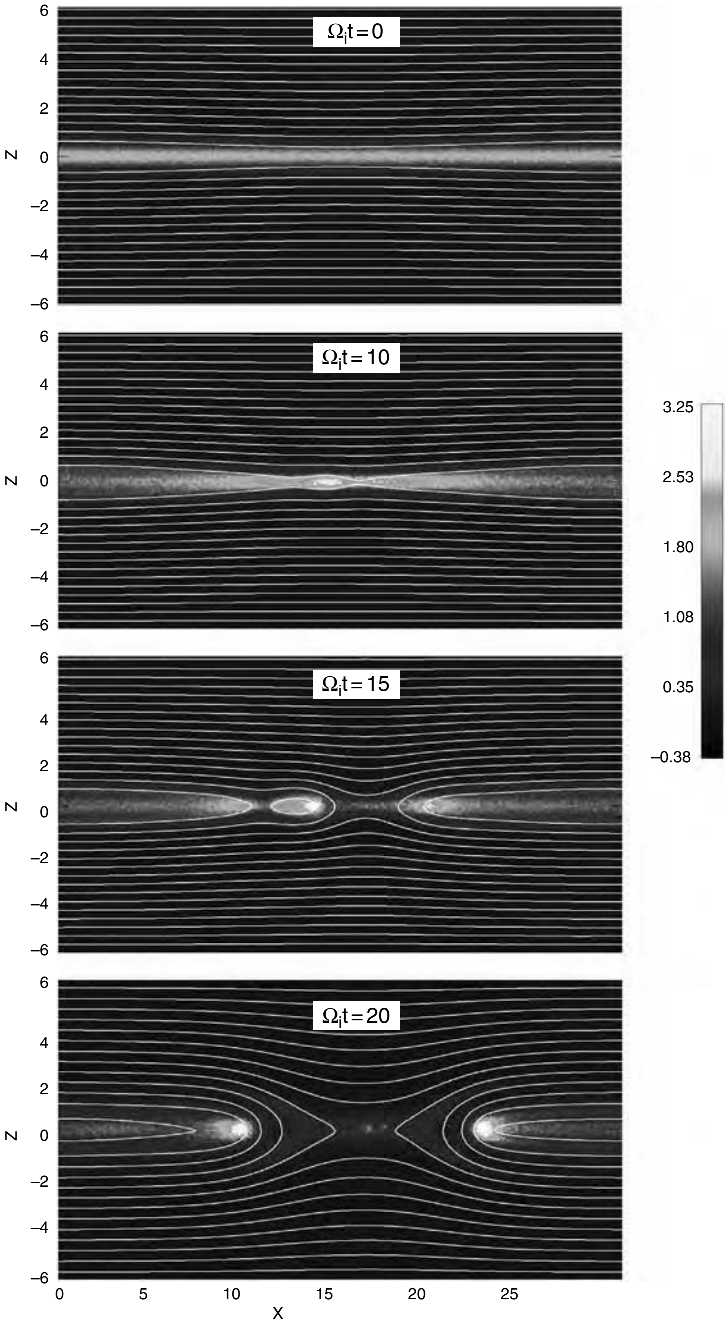

Fig. 3.10. Evolution of the magnetic field and current density (shown in gray scale) in the x, z plane for a simulation with $m_i/m_e = 25$, in the absence of a magnetic guide field. After Hesse *et al.* (1999).

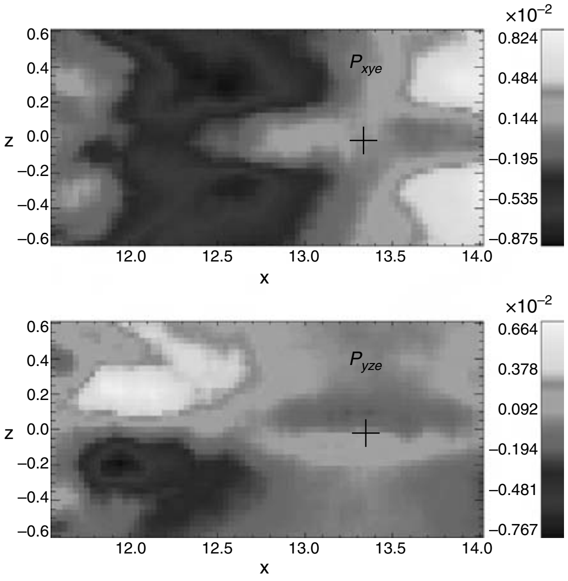

Fig. 3.11. Electron pressure tensor components at the central reconnection site (indicated by the cross-shaped symbol). The tensor tensor components are taken from a calculation with $m_\mathrm{i}/m_\mathrm{e} = 256$. (M. Hesse, unpublished). See also color plate.

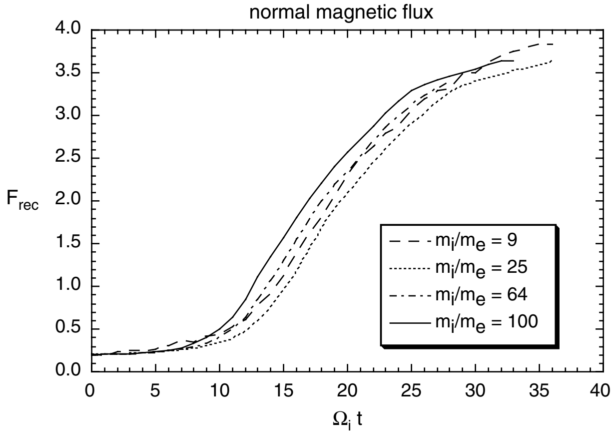

Fig. 3.12. Evolution of the reconnected magnetic flux for different ion–electron mass ratios. After Hesse *et al.* (1999).

that time, the evolution slows down considerably. This is due to a depletion of the magnetic flux in the source regions adjacent to the current sheet which reduces the energy available to power the reconnection process, and a build-up of plasma and magnetic pressure in the magnetic island, which reduces the "pulling" of plasma away from the reconnection region.

A comparison between the different graphs reveals a surprising result: With the exception of a small difference in the duration of the slow evolution, all graphs look essentially alike. This result showed that the electron mass appears to be of little importance to the large-scale evolution, as has been suggested on the basis of hybrid simulations with electron inertia (Shay and Drake, 1998; Shay *et al.*, 1999). In fact, a comparison of other parameters such as velocities and current densities shows striking similarities also (Hesse *et al.*, 1999).

Figure 3.12 shows that the large-scale evolution is apparently controlled by the inertia of the ions and might therefore occur on similar time scales independent of the local electron physics. Hesse *et al.* (1999) used this result to derive an approximate scaling equation for the electric field in the diffusion region. They began with the realization that the electron orbit excursion in a field reversal, and thus the scale of the electron diffusion region, is given by Eq. (3.12) (Biskamp and Schindler, 1971)

$$\delta_{\mathrm{e}} = \left[\frac{2v_{\mathrm{te}}}{\Omega'_{\mathrm{ex}}}\right]^{1/2} = \left[\frac{2m_{\mathrm{e}}T_{\mathrm{e}}}{e^2 B'^2_x}\right]^{1/4}, \tag{3.45}$$

where $\Omega'_{\mathrm{ex}} = eB'_x/m_{\mathrm{e}}$ and B'_x denotes the derivative of B_x with respect to the z direction normal to the current sheet. The corresponding bounce orbit is sketched in Fig. 3.13. This result, combined with the corresponding scale length in the x direction can be used for an estimate of the electric field from (3.43):

$$E_y = -\frac{1}{n_{\mathrm{e}}e}\left(\frac{\partial P_{xy\mathrm{e}}}{\partial x} + \frac{\partial P_{yz\mathrm{e}}}{\partial z}\right) \approx \frac{1}{n_{\mathrm{e}}e}\left(\frac{P_{xy\mathrm{e}}}{\delta_{\mathrm{e}}} + \frac{P_{yz\mathrm{e}}}{\delta_{\mathrm{e}}}\right). \tag{3.46}$$

Here the values of the pressure tensors are to be taken at the edges of the current sheet, where electrons begin to become magnetized. In these regions, the pressure tensor components can be approximated by (Kuznetsova *et al.*, 1998)

$$P_{xy\mathrm{e}} \approx \frac{p_{\mathrm{e}}}{2\Omega_{\mathrm{e}z}}\frac{\partial v_{\mathrm{e}x}}{\partial x} \tag{3.47}$$

and

$$P_{yz\mathrm{e}} \approx -\frac{p_{\mathrm{e}}}{2\Omega_{\mathrm{e}x}}\frac{\partial v_{\mathrm{e}z}}{\partial z}. \tag{3.48}$$

Here the cyclotron frequencies $\Omega_{\mathrm{e}} = eB/m_{\mathrm{e}}$ are evaluated in the z and x components of the magnetic field, at the diffusion region boundary in the x and z directions,

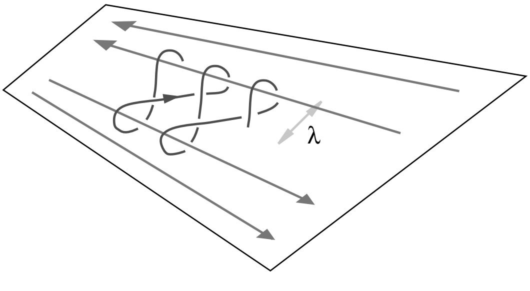

Fig. 3.13. Schematic of the electron meandering orbits in a magnetic field reversal.

respectively. The two velocity derivates are related via an approximate, incompressible, equation of continuity. By relating, e.g., $B_x = B_x' \delta_\mathrm{e}$, a small amount of algebra leads to

$$E_y \approx \frac{1}{e} \frac{\partial v_{\mathrm{e}x}}{\partial x} \sqrt{2 m_\mathrm{e} T_\mathrm{e}} \tag{3.49}$$

for the electric field in the electron diffusion region. This electric field is essentially constant throughout the electron demagnetization region (Hesse *et al.*, 1999).

Since our simulations indicate that the reconnection electric field appears to be independent of the electron mass, (3.49) indicates that the gradient of the electron flow velocity needs to scale like the inverse square root of the electron mass, assuming no substantial changes in the electron temperature. Similarly, by combining (3.49) and (3.45) one finds that the peak electron outflow velocity scales with the inverse fourth root of the electron mass. For an Alfvénic ion outflow velocity, the peak electron outflow will therefore be of the order of $v_\mathrm{e} \sim 6.5\, v_\mathrm{A}$.

The importance of this bounce motion-based dissipation mechanism was verified in a number of further investigations. Comprising one element of the GEM challenge studies, Pritchett (2001b) found electron pressure tensor components of the necessary magnitudes in translationally invariant particle-in-cell models. Similar results were also found by Hesse *et al.* (2001a) and Kuznetsova *et al.* (2001). Pressure tensor-based dissipation was also seen in implicit particle-in-cell simulation with realistic ion–electron mass ratios (Ricci *et al.*, 2002).

The next step consisted of extending the modeled domain to three spatial dimensions. Pritchett (2001a) performed a set of three-dimensional simulations of open and closed magnetic field configurations. Although Pritchett did not investigate electron anisotropies explicitly, he noted that the structure of the reconnection diffusion region is essentially identical to the one found in translationally invariant models. Tanaka (2001) found similar results: reconnection regions that start as two-dimensional structures remain so even in a fully three-dimensional simulation. In addition, Hesse *et al.* (2001b) found that reconnection, when forming out of noise, tends to self-organize into quasi-two-dimensional channels. The prominent dissipation mechanism appeared to be electron nongyrotropy, unchanged from translationally invariant models. Finally, Zeiler *et al.* (2002) found in a high mass ratio simulation that lower-hybrid drift modes do not destroy the quasi-two-dimensional nature of the electron current layer.

Thus, the diffusion region in antiparallel reconnection appears fairly well understood. Nevertheless, there are other modes and instabilities that may change the reconnecting system substantially, without necessarily changing the bounce motion-based dissipation process. These modes and their effects are discussed in Section 3.5.

3.2.3 Guide field reconnection

In principle it is to be expected that the presence of a guide magnetic field, aligned with the current direction, may destroy the bounce motion of the electrons (and ions) in the inner dissipation region. Electron orbits become strongly modified once the thermal electron Larmor radius $r_\mathrm{L} = v_\mathrm{te}/\Omega_\mathrm{e}$ is smaller than or equal to the bounce width in the reconnecting magnetic field component, given by (3.45). After a small amount of algebra, one finds that this condition is equivalent to

$$B_y \geq B'_x \delta_{\mathrm{e}}. \tag{3.50}$$

Equation (3.50) states that electron bounce orbits in the field reversal region become affected by the presence of a finite guide magnetic field once the magnitude of the latter is as big as that of the reconnecting magnetic field at the location of the farthest excursion of an electron bounce motion.

The question of how kinetic dissipation operates if the guide field exceeds the condition (3.50) remains a subject of much debate today. Similar to the antiparallel reconnection case, a set of theory and modeling analyses have been performed, however, without a final conclusion. While some early calculations (e.g, Hesse *et al.*, 1999, 2002; Pritchett, 2001b) indicate that thermal inertial effects may again be the main contributor to the dissipation process, there are many indications that processes that involve variations in the current direction may play a role, too (e.g., Pritchett and Coroniti, 2004; Swisdak *et al.*, 2003). In this section, we provide some detail on the present understanding of the mechanism supporting electron thermal dissipation. However, we will also discuss the present understanding of alternate dissipation processes.

In a situation where B_y exceeds the threshold (3.50), electron nongyrotropies need to be based on perturbations of the dominant Larmor motion about the guide magnetic field. In the wake of earlier results pertaining to electron thermal dissipation (Hesse *et al.*, 1999, 2002; Pritchett, 2001b), Hesse *et al.* (2004) generated a high-resolution numerical calculation of the GEM challenge system for $m_{\mathrm{i}}/m_{\mathrm{e}} = 256$, and a guide magnetic field of 80% of the reconnection magnetic field component. An overview of the evolution of this system, shown in Fig. 3.14, demonstrates the

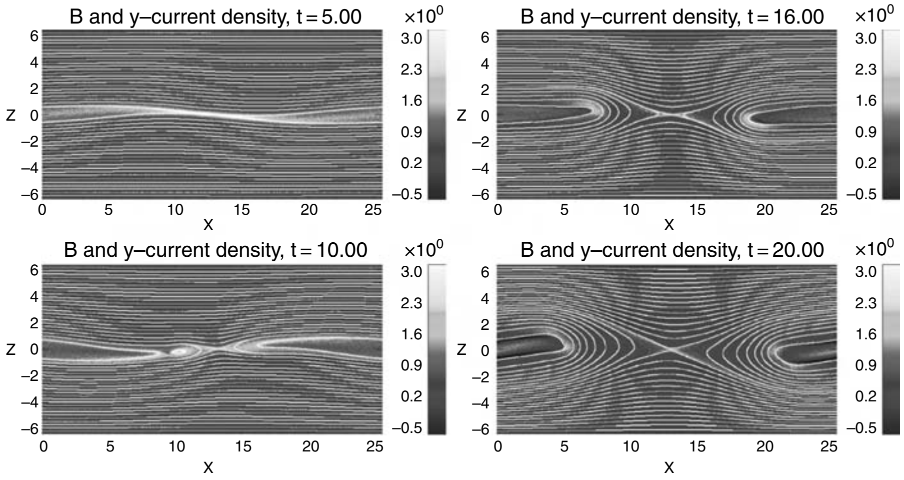

Fig. 3.14. Evolution of the magnetic field and current density for a guide field of 80% and an ion–electron mass ratio of $m_{\mathrm{i}}/m_{\mathrm{e}} = 256$. After Hesse *et al.* (2004). See also color plate.

similarity of the reconnecting system to that found in calculations without guide field components. The initial, X-type perturbation leads to a reconfiguration. The most prominent difference to antiparallel merging is the inclination of the reconnecting current sheet with respect to the x axis. The figure also indicates the presence of a very thin current sheet in the central reconnection region, which is likely associated with electron demagnetization.

The panels of Fig. 3.15 show a blow-up of the inner reconnection region, taken at $t = 16$. The top panel shows magnetic field lines and the total current density in the x, z plane, as well as electron flow velocities. The center panel shows that strong electron flows are associated with strong gradients of the magnetic guide field component B_y. The plot demonstrates the presence of a quadrupole-like magnetic perturbation, albeit strongly distorted and on top of the underlying guide field magnitude of

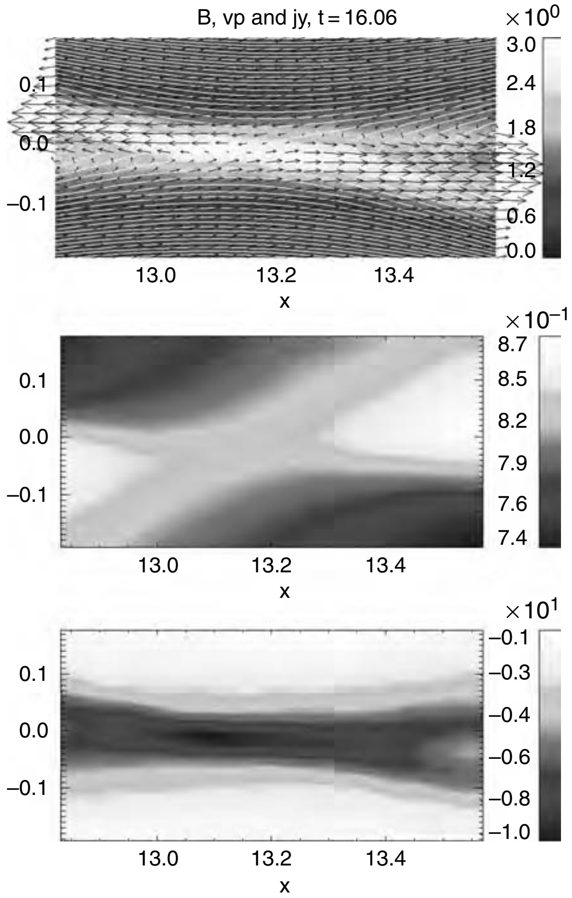

Fig. 3.15. Detailed analysis of the reconnection region in the guide field case. Shown are: Magnetic field and electron flow velocity in the x, z plane with the y component of the current density (top panel); out-of-plane magnetic field B_y and electron flow velocity v_{ey} (center and bottom panels, respectively). After Hesse *et al.* (2004). See also color plate.

$B_{y0} = 0.8$. Finally, the lower panel of Fig. 3.15 displays the electron flow speed in the y direction. While flow velocity magnitudes are similar to those found in simulations of antiparallel merging, the layer is strongly concentrated on a scale substantially smaller than the ion inertial length. We point out that the relative drift between ions and electrons in the present calculation is, for the temperatures encountered in the simulation, close to but not larger than the marginally Buneman-unstable threshold.

The relevant pressure tensor components, $P_{xy\mathrm{e}}$ and $P_{yz\mathrm{e}}$, are shown in the top two panels of Fig. 3.16. The top panels indicate that, despite the magnetizing effect of the guide magnetic field, strong gradients exist particularly in $P_{yz\mathrm{e}}$, which provide

Simulation Output

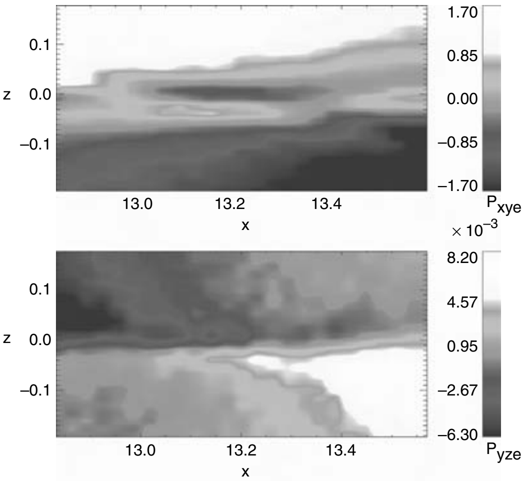

Approximation

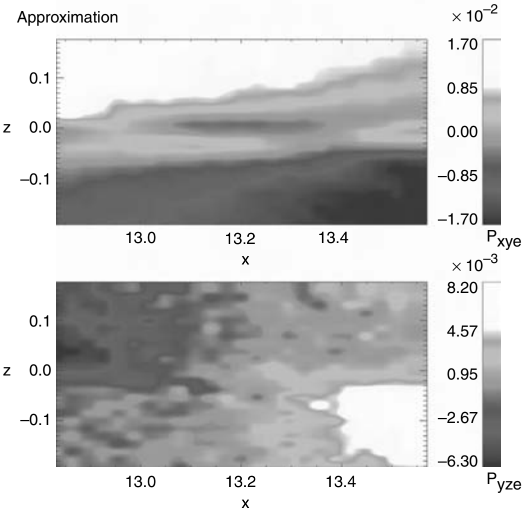

Fig. 3.16. Electron pressure tensor components, derived directly from the particle information (top panels), or from the approximation (3.52) (bottom panels). While the xy components match very well, the yz components show a noticeable difference near $z = 0$ and $x = 13.15$. After Hesse *et al.* (2004). See also color plate.

a sufficiently large reconnection electric field by virtue of (3.46), with an adjacent additional contribution from the electron inertia term (Hesse *et al.*, 2004).

The bottom two panels display the results of the approximation (Hesse *et al.*, 2002)

$$P_{xy\mathrm{e}} \approx -\frac{P_{zz\mathrm{e}}}{\Omega_\mathrm{e}}\frac{\partial v_{\mathrm{e}y}}{\partial z} + (P_{yy\mathrm{e}} - P_{zz\mathrm{e}})\frac{B_x}{B_y}, \tag{3.51}$$

$$P_{yz\mathrm{e}} \approx \frac{P_{xx\mathrm{e}}}{\Omega_\mathrm{e}}\frac{\partial v_{\mathrm{e}y}}{\partial x} + (P_{yy\mathrm{e}} - P_{xx\mathrm{e}})\frac{B_z}{B_y}. \tag{3.52}$$

The panels of Fig. 3.16 show a reasonable agreement between the direct simulation output and the approximation based on (3.51) and (3.52). However, a closer inspection of Fig. 3.16 reveals an important difference: While the particle data-derived value of $P_{yz\mathrm{e}}$ features a clear gradient in the z direction at the reconnection location, at approximately $x = 13.15$, this is not the case in the approximation. This deficiency leads to a substantially reduced value of the reconnection electric field, if calculated based on (3.52). While $P_{xy\mathrm{e}}$ appears to be remarkably well represented by its (3.51), we thus find that (3.52) does not represent the entire, dominant components of the pressure tensor component $P_{yz\mathrm{e}}$.

Investigating this discrepancy further, Hesse *et al.* (2004) found that heat flux tensor effects had to be added into (3.52), with the result

$$P_{yz\mathrm{e}} \approx \frac{P_{xx\mathrm{e}}}{\Omega_\mathrm{e}}\frac{\partial v_{\mathrm{e}y}}{\partial x} + (P_{yy\mathrm{e}} - P_{xx\mathrm{e}})\frac{B_z}{B_y} + \frac{1}{\Omega_\mathrm{e}}\left(\frac{\partial Q_{xxy\mathrm{e}}}{\partial x} + \frac{\partial Q_{xyz\mathrm{e}}}{\partial z}\right), \tag{3.53}$$

where Q_{xxy} and Q_{xyz} are components of the heat flux tensor defined below in (3.55).

The second heat flux-related term in (3.53) is dominant in the immediate vicinity of the reconnection region. Therefore, (3.53) can be simplified

$$P_{yz\mathrm{e}} \approx \frac{P_{xx\mathrm{e}}}{\Omega_\mathrm{e}}\frac{\partial v_{\mathrm{e}y}}{\partial x} + (P_{yy\mathrm{e}} - P_{xx\mathrm{e}})\frac{B_z}{B_y} + \frac{1}{\Omega_e}\frac{\partial Q_{xyz\mathrm{e}}}{\partial z}. \tag{3.54}$$

The result of this approximation, depicted in Fig. 3.17, shows an excellent match with the direct determination of $P_{yz\mathrm{e}}$ from the particle data. Thus, an appropriate approximation of the pressure nongyrotropy in the immediate vicinity of the neutral

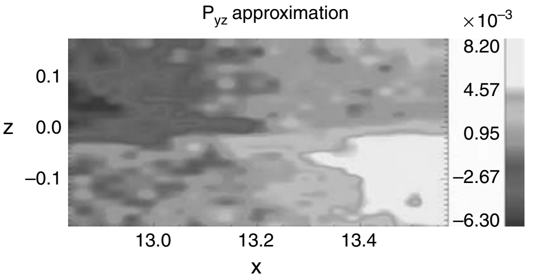

Fig. 3.17. Approximation of the pressure tensor component $P_{yz\mathrm{e}}$ that includes heat flux contributions. This approximation shows an excellent match with Fig. 3.16. After Hesse *et al.* (2004). See also color plate.

point of the magnetic field in the x, z plane cannot be found without inclusion of a heat flux tensor component.

Derivation of a scaling law of the reconnection process therefore requires an analytic expression of an evolution equation for the entire heat flux tensor. Hesse *et al.* (2004) developed this expression for collisionless systems. The heat flux tensor is defined in the electron center-of-mass system as

$$\mathbf{Q} = m_s \int \mathrm{d}^3 u (\mathbf{u} - \mathbf{v})(\mathbf{u} - \mathbf{v})(\mathbf{u} - \mathbf{v}) f_s. \tag{3.55}$$

Here, f_s and m_s denote the distribution function and mass of plasma species s, $\mathbf{u}$ the phase space velocity, and $\mathbf{v}$ the bulk flow speed. An evolution equation for $\mathbf{Q}$ is obtained by multiplying the Vlasov equation by **uuu** and integrating over phase space. The result needs to be transformed into the center-of-mass frame of species s in order to derive an evolution equation for $\mathbf{Q}$. After a considerable amount of algebra, one finds for the components of the heat flux tensor (index e omitted for simplicity)

$$\begin{aligned} &\tfrac{\partial}{\partial t} Q_{ijk} \\ &+ \sum_l \tfrac{\partial}{\partial x_l} (\Gamma_{ijkl} + P_{kl} v_i v_j + P_{il} v_j v_k + P_{jl} v_i v_k + Q_{ijk} v_l) \\ &+ \sum_l Q_{lij} \tfrac{\partial}{\partial x_l} v_k + \sum_l Q_{ljk} \tfrac{\partial}{\partial x_l} v_i + \sum_l Q_{lik} \tfrac{\partial}{\partial x_l} v_j \\ &+ \tfrac{e_s}{m_s} \sum_{r>s} \left[\begin{array}{l} [Q_{ijs} B_r - Q_{ijr} B_s] \varepsilon_{rsk} \\ +[Q_{iks} B_r - Q_{ikr} B_s] \varepsilon_{rsj} \\ +[Q_{jks} B_r - Q_{jkr} B_s] \varepsilon_{rsi} \end{array} \right] = 0. \end{aligned} \tag{3.56}$$

Here e_s denotes the charge of species s, and ε_{ijk} is the usual, totally antisymmetric tensor. Equation (3.56) relates the time evolution of Q_{ijk} to lower order moments such as pressure and velocities, as well as to the fourth order tensor Γ_{ijkl}. The last term in (3.56) represents the effects of particle cyclotron motion on the heat flux tensor. Clearly, (3.56) is invariant under change of order of indices, leading to a totally symmetric heat flux tensor.

Further progress toward a simple scaling relation requires simplifying assumptions. Neglecting time dependence and the 4-tensor, an expression for Q_{xyz} can be obtained from the x, y, x component of (3.56)

$$\begin{aligned} &\sum_l \tfrac{\partial}{\partial x_l} (2 P_{xl} v_x v_y + P_{yl} v_x v_x + Q_{xyx} v_l) \\ &+ \sum_l Q_{lxy} \tfrac{\partial}{\partial x_l} v_x + \sum_l Q_{lyx} \tfrac{\partial}{\partial x_l} v_x + \sum_l Q_{lxx} \tfrac{\partial}{\partial x_l} v_y \\ &- \tfrac{e}{m_{\mathrm{e}}} (2 Q_{xyy} B_z - 2 Q_{xyz} B_y + Q_{xxx} B_z - Q_{xxz} B_x) = 0. \end{aligned} \tag{3.57}$$

Neglecting magnetic field components other than B_y, the convection term $\sum_l \frac{\partial}{\partial x_l} (Q_{xyx} v_l)$, and assuming Q_{rst}¡$P_{rs} v_t$ (a reasonable assumption for a nearly gyrotropic plasma) near the reconnection region, reduces (3.57) to the simple expression

$$Q_{xyz} \approx -\frac{1}{\Omega_y} \left[\frac{\partial}{\partial x} \left(P_{xx} v_x v_y + 0.5 P_{xy} v_x^2 \right) + \frac{\partial}{\partial z} \left(P_{xz} v_x v_y + 0.5 P_{yz} v_x^2 \right) \right]. \tag{3.58}$$

The leading order terms in (3.58) are

$$Q_{xyz} \approx -\frac{1}{\Omega_y}\frac{\partial}{\partial x}(P_{xx}v_x v_y) \approx -\frac{P_{xx}v_y}{\Omega_y}\frac{\partial v_x}{\partial x} \tag{3.59}$$

for the relevant component of the electron heat flux tensor. This approximation was found to be adequate in the electron current sheet.

The reconnection region now has two transitions, the first, where the convection electric field becomes equal to the inertial electric field, at a scale L_1, and a second, L_2, where the inertial electric field is matched to the pressure tensor-derived electric field. L_1 is readily determined by the expansion (e.g., Vasyliūnas, 1975)

$$\begin{aligned} |E_{\text{inertial}}| &\sim \frac{m_\text{e}}{e} v_{\text{e}z} \frac{\partial v_{\text{e}y}}{\partial z} \sim \frac{1}{L_1^2}\frac{B_0 v_{\text{e}z}}{\mu_0}\frac{m_\text{e}}{e^2 n_\text{e}} \\ &= B_0 v_{\text{e}z}\frac{c^2}{\omega_{\text{pe}}^2}\frac{1}{L_1^2} = |E_{\text{convection}}|\frac{c^2}{\omega_{\text{pe}}^2}\frac{1}{L_1^2}. \end{aligned} \tag{3.60}$$

The pressure electric field is derived from the first term of (3.45). With the addition of (3.61), the pressure tensor y, z component (3.57) becomes

$$P_{yz\text{e}} \approx \frac{P_{xx\text{e}}}{\Omega_{\text{e}y}}\frac{\partial v_{\text{e}y}}{\partial x} + (P_{yy\text{e}} - P_{xx\text{e}})\frac{B_z}{B_y} - \frac{1}{\Omega_{\text{e}y}}\frac{\partial}{\partial z}\left(\frac{P_{xx\text{e}}v_{\text{e}y}}{\Omega_{\text{e}y}}\frac{\partial v_{\text{e}x}}{\partial x}\right), \tag{3.61}$$

where the last term dominates the reconnection electric field near the zero of the magnetic field in the x, z plane. Ignoring lower order terms, and assuming a divergence-free electron velocity, the pressure electric field can be scaled

$$\begin{aligned} |E_{\text{pressure}}| &\sim \frac{1}{n_\text{e} e}\frac{1}{\Omega_{\text{e}y}}\frac{\partial^2}{\partial z^2}\left(\frac{P_{xxy}v_{\text{e}y}}{\Omega_{\text{e}y}}\frac{\partial v_{\text{e}x}}{\partial x}\right) \\ &\sim \frac{1}{n_\text{e} e}\frac{1}{\Omega_{\text{e}y}}\frac{\partial^2}{\partial z^2}\left(\frac{P_{xx\text{e}}v_{\text{e}y}}{\Omega_{\text{e}y}}\frac{\partial v_{\text{e}z}}{\partial z}\right) \\ &\sim |E_{\text{inertial}}|\frac{1}{L_2^2}\frac{P_{xx\text{e}}}{\Omega_{\text{e}y}^2}\frac{1}{n_\text{e} m_\text{e}} = |E_{\text{inertial}}|\frac{r_\text{L}^2}{L_2^2}. \end{aligned} \tag{3.62}$$

Equation (3.62) states that the transition from inertia-based to pressure-based dissipation occurs at a scale length equal to the electron Larmor radius in the guide magnetic field component.

Thus we find that there may be two scale lengths associated with collisionless magnetic reconnection in the presence of moderate guide fields. The first, well-known scale is reached when the inertial electric field equates the magnitude of the convection electric field. This scale length is the collisionless skin depth. For values of the electron $\beta = \mu_0 p_{\text{e}\perp}/B^2$ of less than unity, the second transition occurs at a scale length of an electron Larmor radius in the guide magnetic field. The very small scales associated with the electron Larmor radius permit the heat flux to take on an unprecedented role in the electron dissipation process.

Physically, electron scattering can occur if the Larmor radius in the guide field is comparable to the gradient scale length in the reconnecting electric field. The situation is sketched in Fig. 3.18. Electron scattering occurs due to the interaction of field-aligned and gyromotions with the ambient reconnecting electric field components.

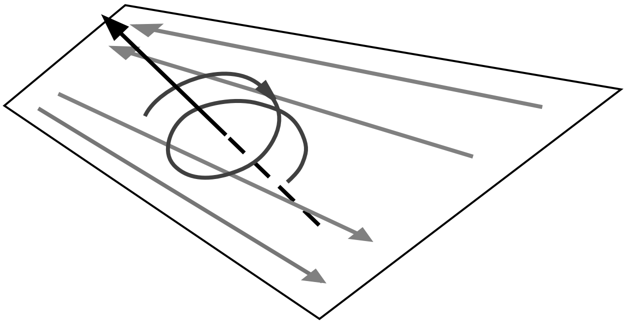

Fig. 3.18. Schematic of the interaction of the electron Larmor motion about the guide field with the reconnection magnetic field component.

It should be noted that the electron-based electric field expression

$$E_y \approx \frac{1}{en_\mathrm{e}} \frac{1}{\Omega_{\mathrm{e}y}} \frac{\partial}{\partial z} \left(\frac{P_{xx\mathrm{e}} v_{\mathrm{e}y}}{\Omega_{\mathrm{e}y}} \frac{\partial v_{\mathrm{e}x}}{\partial x} \right) \sim \frac{1}{e} \frac{\partial v_{\mathrm{e}x}}{\partial x} T_\mathrm{e} \frac{1}{\Omega_{\mathrm{e}y}^2} \frac{\partial^2 v_{\mathrm{e}y}}{\partial z^2} \tag{3.63}$$

may equally well be expressed through the ions, which exhibit similar dynamics, albeit on the larger scale of an ion Larmor radius. The result is the same as (3.63), but with an index change, and a sign change.

While this analysis presents a consistent solution to the reconnection dissipation problem in the presence of a guide field, the question remains whether the additional freedom of a fully three-dimensional evolution might enable other dissipative processes such as discussed in Section 3.5. While Silin and Büchner (2003b) find that lower-hybrid drift, kink, and sausage modes appear suppressed in the presence of a guide field, and Scholer *et al.* (2003) saw the formation of essentially two-dimensional reconnection channels, a candidate process is based on the formation of electrostatic, solitary structures associated with the nonlinear evolution of the Buneman instability (Drake *et al.*, 2003). Drake *et al.* argue that correlations of electron density fluctuations that are associated with these *electron holes* provide a mechanism for anomalous resistivity. The modeled electrostatic solitons are well matched by observations of the magnetopause current layer (Cattell *et al.*, 2002a), which reveal the presence of electrostatic solitary waves that propagate rapidly along the current direction. Although the overall morphology and reconnection rates of Drake *et al.*'s (2003) three-dimensional simulations are very similar to translationally invariant calculations, and Pritchett and Coroniti (2004) advocate inertial processes, the Buneman mode-based dissipation process deserves further studies to clarify its viability in guide-field magnetic reconnection.

3.3 Onset of magnetic reconnection

P. L. Pritchett

As discussed in Chapter 1 and in Section 3.1, many scenarios of the occurrence of reconnection involve a sudden transition from a quiescent, slowly evolving state to a rapid energy release. A critical problem hence is not only to explain fast reconnection rates, responsible for the energy release, but also to identify the mechanism for this transition, that is, the mechanism for the onset of reconnection, or the onset of fast reconnection. This holds particularly for the onset of reconnection in the terrestrial magnetotail, which appears to be closely related to the onset of magnetospheric substorms (Section 1.2). To lowest order, the magnetotail current sheet configuration resembles the classical Harris (1962) neutral sheet. It was proposed very early in the space era (Coppi *et al.*, 1966) that collisionless reconnection could occur in the Earth's magnetotail as a result of an electron tearing mode driven by the electron Landau interaction. It was hypothesized that this tearing instability could serve as the triggering mechanism that powers the sudden onset of magnetic reconnection associated with the expansion phase of substorms in the terrestrial magnetotail.

This simple one-dimensional picture of the magnetotail must fail, however, inasmuch as the field lines must connect to the intrinsic dipolar magnetic field of the planet. For the Earth there is a small northward component of the magnetic field in the region of the current sheet whose magnitude is typically a few nanoteslas, which is about 10% of the asymptotic (lobe) field strength (e.g., Fairfield and Ness, 1970). As we shall discuss, the presence of this *normal* magnetic field component has profound implications for the possibility of magnetic reconnection in a planetary magnetotail; the investigation of these consequences is generally referred to as the *onset* problem for magnetic reconnection. On the most fundamental level, the resulting cyclotron motion of electrons in even a very weak normal field removes the electron Landau resonance (Galeev and Zelenyi, 1976), thus ruling out the possibility of an electron tearing mode.

More general consequences of a two-dimensional (2D) isotropic equilibrium configuration were deduced by Schindler (1972) and Birn *et al.* (1975). Let $z = a(x) > 0$ be the location of the magnetopause (assumed to be a field line). There are then two possible situations depending on the sign of $\mathrm{d}a/\mathrm{d}x$ (assuming that x increases in the tailward direction): (1) $\mathrm{d}a/\mathrm{d}x > 0$ (i.e., the tail diverges as one moves away from the planet) is a necessary (but not sufficient) condition for instability of the tail. (2) If $\mathrm{d}a/\mathrm{d}x < 0$ (i.e., the tail converges), then the tail is stable. With $B_{0z}(x, z = 0) > 0$, then $\mathrm{d}a/\mathrm{d}x > 0$ requires that B_{0z} change sign somewhere. If B_{0z} has the same sign everywhere, then the tail equilibrium is stable. For the Earth, it is known that B_{0z} does indeed change sign as one moves into the lobes (e.g., Fairfield, 1979). Thus the flaring of the Earth's lobe field could allow for the possibility of some kind of tearing instability.

The outline of this section is as follows. In Section 3.3.1 we discuss the consequences of the finite normal magnetic field for what is known as the pure ion tearing instability. In Section 3.3.2 we review the stabilizing effects of electron dynamics in the presence of the normal field on the tearing instability. In Section 3.3.3 we consider the implications of the third dimension (out-of-plane coordinate) on the tearing instability. In Section 3.3.4 we describe some recent results on externally driven reconnection. Section 3.3.5 contains a summary and outlook.

3.3.1 The pure ion tearing instability

The tearing hypothesis for the magnetotail was resurrected by Schindler (1974) who suggested that ion Landau damping could drive a pure ion tearing instability in which the electron dynamics was presumed to be unimportant due to the small value of the electron temperature ($T_\mathrm{e}/T_\mathrm{i} \ll 1$). He noted that the characteristic scaling of the ion tearing growth rate in the absence of the normal field, valid for $\rho_{\mathrm{i}0}/\lambda \ll 1$, would be of the form (Laval *et al.*, 1966)

$$\gamma/\Omega_{\mathrm{i}0} \sim (\rho_{\mathrm{i}0}/\lambda)^{5/2}, \tag{3.64}$$

where λ is the half-thickness of the current sheet and $\rho_{\mathrm{i}0}$ ($\Omega_{\mathrm{i}0}$) is the ion gyroradius (cyclotron frequency) in the asymptotic field B_0. During quiet times, the ratio $\rho_{\mathrm{i}0}/\lambda \sim 0.03$. Thus the scaling (3.64) would give $\gamma/\Omega_{\mathrm{i}0} \sim 2\times 10^{-4}$ or $1/\gamma \sim 1\,\mathrm{h}$, which is too long to be relevant to substorm onset times. It was expected, however, that as the current sheet thinned during the growth phase, the growth time for the tearing instability would decrease substantially. This is particularly significant, since it was expected that the condition $\gamma/\Omega_{\mathrm{i}0} > B_\mathrm{n}/B_0$ would need to be satisfied in order that the free-streaming particle motion which drives the tearing instability would not be destroyed by the gyromotion in the normal field B_n. The scaling (3.64) suggests that for $\rho_{\mathrm{i}0}/\lambda \approx 1$, this condition easily would be satisfied for $B_\mathrm{n}/B_0 \sim 0.1$.

Subsequent investigations, however, showed that the basic reconnection growth rate increases much less rapidly as $\rho_{\mathrm{i}0}/\lambda \to 1$ than suggested by the scaling (3.64). Pritchett *et al.* (1991) and Brittnacher *et al.* (1995) considered the case of pure ion tearing (alternatively, electron–ion tearing with a mass ratio $m_\mathrm{i}/m_\mathrm{e} = 1$) for the case of very thin current sheets with $\rho_{\mathrm{i}0}/\lambda \approx 1$. They obtained a maximum underlying growth rate

$$\gamma_\mathrm{max}/\Omega_{\mathrm{i}0} \approx 0.50(\rho_{\mathrm{i}0}/\lambda)^{5/2}/(1+2\rho_{\mathrm{i}0}^2/\lambda^2). \tag{3.65}$$

The term $1+2\rho_{\mathrm{i}0}^2/\lambda^2$ in the denominator arises from the inclusion of the particle drift in the cross-tail direction in the particle orbits. For $\rho_{\mathrm{i}0}/\lambda \sim 1$, this term clearly differs significantly from unity, and the maximum growth rate for $\rho_{\mathrm{i}0}/\lambda = 1$ is only $\gamma_\mathrm{max}/\Omega_{\mathrm{i}0} \approx 0.17$, roughly a factor of 6 smaller than expected from (3.64). Thus even for a sheet as thin as the ion gyroradius (~400 km), the maximum tearing growth rate is only marginally larger than the typical value of $B_\mathrm{n}/B_0 \sim 0.1$. Particle-in-cell (PIC) simulations have confirmed that the stabilization of the pure ion tearing mode in a thin current sheet does indeed occur when $B_\mathrm{n}/B_0 \sim \gamma/\Omega_{\mathrm{i}0}$ (Pritchett *et al.*, 1991).

The tearing growth rate as a function of $m_\mathrm{i}/m_\mathrm{e}$ has been calculated by Daughton (1999b) for the case of the Harris neutral sheet. The maximum growth rate decreases slowly with increasing $m_\mathrm{i}/m_\mathrm{e}$; for $\rho_{\mathrm{i}0}/\lambda = 1$ and $T_\mathrm{i}/T_\mathrm{e} = 1$, it falls to $\gamma/\Omega_{\mathrm{i}0} = 0.07$ at $m_\mathrm{i}/m_\mathrm{e} = 1836$. It thus seems that it would be very difficult to excite the spontaneous ion tearing instability unless B_n were reduced considerably below its normal value.

3.3.2 Electron stabilization of ion tearing

Traditionally, the analysis of electron stabilization for the ion tearing instability has been carried out using an idealized 2D plasma sheet configuration in the noon–midnight meridional (x,z) plane; no variation in the y direction is considered. In such a configuration and assuming a tearing perturbation $A_{1y} = A_1(x,z)\mathrm{e}^{\gamma t}$ and an electrostatic potential $\Phi_1 = \Phi_1(x,z)\mathrm{e}^{\gamma t}$, the completely general energy principle is (Laval and Pellat, 1964; Schindler, 1966)

$$\delta W = \int \mathrm{d}^3x \Big[|\nabla A_1|^2 - \mu_0 \frac{\mathrm{d}J_0}{\mathrm{d}A_0} |A_1|^2 + \sum_{i,e} 4\pi T \int \mathrm{d}^3v \frac{|\tilde{f}_1|^2}{f_0} \Big]. \tag{3.66}$$

Here, f_0 is the equilibrium distribution function, J_0 is the equilibrium current density, and $\tilde{f}_1 = f_1 - A_1 \partial f_0/\partial A_0$ is the nonadiabatic part of the perturbed distribution f_1. The first term in (3.66) represents the stabilizing effect of field-line tension, the second term is the destabilizing free energy associated with the adiabatic response to the equilibrium currents, and the last term represents the compressibility effect arising from the perturbed current density due to $\tilde{f}_1$. Various assumptions have been made regarding the nature of the electron dynamics.

Adiabatic electrons

Lembège and Pellat (1982) used a drift-kinetic analysis (which should be valid for time and space scales long compared to the electron cyclotron period and electron Larmor radius) and assumed adiabatic motion for the electrons. They demonstrated that the tearing mode electromagnetic field produces a strong compression of the electron density which is independent of T_e. This perturbation also forces a large electrostatic potential in order to maintain charge neutrality. In the energy principle (3.66), the energy associated with the electron compression exceeds the free energy available from the reversed magnetic field configuration provided that the condition

$$k_x\lambda > (4/\pi)B_\mathrm{n}/B_0 \tag{3.67}$$

is satisfied. In order to violate (3.67) and thus to permit instability, the wavelength of the mode would have to exceed $\sim 60\lambda$. On such a large scale the conditions necessary for the WKB approximation to be valid would be violated, and so Lembège and Pellat concluded that the ion tearing mode was stable.

Effects of turbulence

Several attempts to circumvent this result were made by appealing to the effects of turbulence. Coroniti (1980) argued that, since the plasma sheet contains modest to high levels of electromagnetic turbulence, it is possible that pitch angle scattering by background wave turbulence could invalidate the assumption of adiabatic electron motion. His analysis found an electron tearing mode growth rate proportional to a bounce-averaged pitch angle diffusion coefficient.

Adopting Coroniti's formalism, Büchner and Zelenyi (1987) replaced wave pitch-angle scattering by the stochastic changes in the first adiabatic invariant (μ) which can occur when the plasma sheet thins and the adiabaticity parameter

$$\kappa_\mathrm{e} = (B_\mathrm{n}/B_0)(\lambda/\rho_{\mathrm{e}0})^{1/2} \tag{3.68}$$

becomes less than or of the order of 1. Here $\rho_{\mathrm{e}0}$ is the electron Larmor radius based on B_0. They suggested that the resulting diffusion in μ should permit tearing growth rates comparable to Schindler's estimate (3.64) for the ion tearing mode. With $\kappa_\mathrm{e} \sim 1$, they argued that the electron dynamics would be unimportant.

Canonical momentum conservation

Pellat *et al.* (1991) pointed out that the analysis by Coroniti (1980) contained an error in that it relied on an approximate form of a Green's function solution. The exact solution has the property that the perturbed number of particles on a flux tube is conserved. They showed that this result followed directly from the conservation of the canonical momentum P_y in a 2D system, independent of any assumption of electron adiabaticity. P_y conservation alone was sufficient to constrain the cyclotron excursion in the direction transverse to the magnetic surface. They demonstrated further that neither wave turbulent pitch-angle scattering nor nonadiabatic stochastic first-invariant diffusion would alter the number of particles on a flux tube. They recovered the Lembège–Pellat stability criterion (3.67) under the very mild assumption that $k_x\rho_{\mathrm{en}} < 1$, where ρ_{en} is the electron Larmor radius in the B_{n} field. Assuming the proton/electron value for the mass ratio, $T_{\mathrm{i}}/T_{\mathrm{e}} \approx 7$, $\rho_{\mathrm{i0}}/\lambda \sim 1$, and a wavenumber $k_x\lambda \approx 0.5$, one finds that this condition is satisfied for a normal field of only $B_{\mathrm{n}}/B_0 \sim 5 \times 10^{-3}$.

2D PIC simulations provided direct confirmation of this electron stabilization effect (Pritchett, 1994). These simulations used a value $B_{\mathrm{n}}/B_0 = 0.02$ so that the ion tearing mode was still unstable. With $\rho_{\mathrm{i0}}/\lambda$ held fixed at 1, simulations were performed with $m_{\mathrm{i}}/m_{\mathrm{e}}$ varying from 1 to 64 and $T_{\mathrm{i}}/T_{\mathrm{e}}$ from 1 to 8. As $k_x\rho_{\mathrm{en}}$ approached unity, the tearing mode growth decreased dramatically. Qualitatively similar results were obtained in simulations by Dreher *et al.* (1996) for a mass ratio $m_{\mathrm{i}}/m_{\mathrm{e}} = 10$ and temperature ratios up to $T_{\mathrm{i}}/T_{\mathrm{e}} = 20$.

Brittnacher *et al.* (1994) reexamined use of the energy principle as applied to ion tearing. They treated the case of intrinsic pitch-angle diffusion using a Vlasov description and recovered the Lembège–Pellat result (3.67). For the case of external pitch-angle diffusion they employed a drift-kinetic description and found that the energy principle contains an additional term. This new term is stabilizing, however, and thus at best the marginal stability criterion is still the same.

An alternative Vlasov treatment of the onset problem is given in Section 4.3.2. The approach discussed there treats a larger class of distribution functions, avoids the use of inequalities, and introduces the small electron gyroscale regime by considering the formal limit $m_{\mathrm{e}} \to 0$. This more refined approach confirms the strong electron stabilization in the appropriate limit.

Fluid treatment

Further insight into the physics of the electron stabilization effect was provided by Quest *et al.* (1996). They employed the standard energy principle formalism given in (3.66). In evaluating the perturbed particle density on a flux tube, they used fluid equations assuming that the electrons were *frozen-in* to the magnetic field. They argued that if the effective gyroradius of the electrons is small compared to both the half-width λ and $1/k_x$ and if spatial diffusion and electron resonance effects are negligible, then it is justifiable to neglect both the inertial term and the off-diagonal pressure tensor elements in the electron momentum equation. There was no requirement that the electron orbits be adiabatic, merely that they were confined to the proximity of a field line, as is required by conservation of P_y (Pellat *et al.*, 1991). This fluid analysis also recovered the Lembège–Pellat result (3.67), and it further demonstrated that the compressional stabilization is independent of the presence of a (uniform) guide field component B_{0y} in the initial configuration. The electron stabilization is thus a macroscopic fluid effect, independent of the specifics of the electron orbits.

Exact particle orbits

In none of the energy principle analyses described so far was the linear stability problem solved directly. Instead, techniques such as the Schwartz inequality were employed to obtain marginal stability limits; the exact particle orbits were not used. Brittnacher *et al.* (1998) devised a new approach in which the energy equation was solved using a finite element procedure where the quantities that depend on the details of the particle orbits were determined by standard PIC simulation methods. Since the exact orbits were considered, it was possible to take into account the effects of pitch-angle scattering (both intrinsic and induced by an external wave source) and spatial diffusion. They found that none of these effects could destabilize the ion mode. For $k_x \rho_{\mathrm{en}} < 1$, the mode was stabilized by the electron compressibility effects. For weaker values of B_{n}, finite Larmor radius effects (Galeev and Zelenyi, 1976) were sufficient to stabilize the mode. Thus, the spontaneous ion mode should not occur in the tail current sheet. They found that the electron tearing mode could be reestablished by pitch-angle diffusion, but only for values of $B_{\mathrm{n}}/B_0 \approx 10^{-4}$ too small to apply to the near-Earth tail.

Transient electrons

All the previous stability analyses have treated the electron population as basically a single fluid. Sitnov *et al.* (1998) reexamined the tearing stability analysis including the effect of a transient electron population. They stressed that in isotropic self-consistent current sheet models the number density of transient electrons is not a free parameter; its local value depends on basic sheet parameters such as B_{n}/B_0 and on the distance z from the neutral plane. Using an energy principle analysis, they found a new version of the stability condition (3.67):

$$k_x \lambda > (4/\pi)(T_{\mathrm{i}}/3T_{\mathrm{e}})^2 B_{\mathrm{n}}/B_0. \tag{3.69}$$

Since $(T_{\mathrm{i}}/3T_{\mathrm{e}})^2 \sim 5$ in the magnetotail, it is now possible to reach the marginal stability limit for modes that are consistent with the WKB approximation, leaving open the possibility that the tearing mode could be unstable. In a subsequent explicit nonlocal Vlasov linear stability analysis, Sitnov *et al.* (2002) found instability with $T_{\mathrm{e}}/T_{\mathrm{i}} \ll 1$ when the current sheet was sufficiently long so that the electrons leaving it could be treated as transient particles. The specific dependence of the marginal wavenumber on $T_{\mathrm{i}}/T_{\mathrm{e}}$ turned out to be less pronounced than given by (3.69). This new result suggests that while the tearing mode is unlikely to be excited in the transition region between the dipole and tail-like magnetic fields, it may very likely be unstable at distances further down the tail where the length of the tail current sheet is much larger than its thickness.

3.3.3 Effects of the third dimension

When the restriction to 2D systems is removed and variations in the cross-tail (y) direction are permitted, the canonical momentum P_y is no longer conserved. It then follows that the particle density along a flux tube need no longer be constant. With the inclusion of the y dependence, a much larger class of instabilities becomes possible, and many of these have been proposed as mechanisms for disrupting the tail current sheet. This subject is treated in detail in Section 3.5 of this work. Here we consider only the rather limited number of investigations that have looked at cross-tail instabilities in the presence of a finite normal field component.

One member of the class of kinetic cross-field instabilities has the character of a kink mode in the y, z plane. This mode was first identified in 2D PIC simulations by Zhu *et al.* (1992), and they found that its growth rate in a thin current sheet could be faster than that of the collisionless tearing instability in the Harris sheet. Pritchett and Coroniti (1996) showed from a two-fluid analysis with finite electron inertia that the long-wavelength kink mode ($k_y\lambda < 1$) is linearly unstable. Since the growth rate is proportional to the magnitude of the relative electron–ion cross-field drift, they referred to the mode as a drift-kink mode. The behavior of this mode in the presence of a normal field component was investigated in 3D PIC simulations by Pritchett *et al.* (1996). They considered the case of a $\rho_{\mathrm{i0}}/\lambda = 1$ current sheet with a constant value of $B_{\mathrm{n}}/B_0 = 0.06$ at $z = 0$ and used $m_{\mathrm{i}}/m_{\mathrm{e}} = 16$. In a pure 2D geometry this configuration would be stable to tearing due to the combined effects of electron stabilization and ion gyromotion. In the early stage of the simulation (up to $\Omega_{\mathrm{i0}}t\sim 60$), there was clear growth of the drift-kink modes with $k_y\lambda \sim 0.8$–1.2, although their growth rates were reduced compared to the case of $B_{\mathrm{n}} = 0$. There was no indication for any growth of shorter-wavelength lower-hybrid drift modes (Section 3.5.2). Beginning at $\Omega_{\mathrm{i0}}t \sim 50$, pure tearing modes began to grow and there was an increase in the B_z^2 field energy, indicating that reconnection was occurring. This initial stage of reconnection led to a further reduction in the local value of B_{n}. This field finally reached zero in one location by $\Omega_{\mathrm{i0}}t \sim 100$, and this event signaled the onset of a highly nonlinear stage which was characterized by the formation of a conventional island configuration. It thus appeared that the kink mode could trigger the onset of reconnection.

It turns out, however, that, unlike the case of the tearing mode, the drift-kink growth rate is extremely sensitive to the value of $m_{\mathrm{i}}/m_{\mathrm{e}}$. Daughton (1999b) showed that while the growth rate of the kink mode exceeds that of the tearing mode by about a factor of two for $m_{\mathrm{i}}/m_{\mathrm{e}} = 16$, for the realistic proton mass ratio of 1836 the kink growth rate is smaller than the tearing rate by about a factor of 25. Thus low mass ratio simulations probably greatly overestimate the effect of the drift-kink mode. Daughton (1999b) also noted, however, that another type of kink mode could be strongly excited ($\gamma/\Omega_{\mathrm{i0}} \sim 0.1$) at realistic mass ratios. This second type of kink mode is driven by the relative drift between two ion species and has been referred to as the ion–ion kink mode (Karimabadi *et al.*, 2003a,b). The maximum growth rate occurs for $k_y\lambda \sim 0.7$, the real frequency is $\omega_{\mathrm{r}} \approx k_y v_{\mathrm{d}}$ (where v_{d} is the effective single fluid drift velocity at $z = 0$), and the growth rate is always larger than that for the tearing mode. 3D simulations with $m_{\mathrm{i}}/m_{\mathrm{e}} = 100$ (Karimabadi *et al.*, 2003b) showed that the growth of the ion–ion kink mode is not sensitive to the presence of a (weak) normal field component, unlike the case of the electron–ion kink mode. Thus the ion–ion kink mode is still a possible candidate to reduce or eliminate the effects of electron stabilization.

3.3.4 Externally driven reconnection

Despite its long history, it is by no means clear that the spontaneous tearing instability is the relevant process for explaining substorm onset in the magnetotail. Considerable attention has also been paid to the possibility that substorms could be triggered by external perturbations (Caan *et al.*, 1975; Rostoker *et al.*, 1983; Lyons, 1995, 1996). It appears that a substantial fraction (~60%) of substorm onsets can be associated with northward turnings of the IMF (Hsu and McPherron, 2003). Prior to onset, a southward IMF imposes an enhanced convection electric field on the magnetotail. A number of MHD and Hall MHD studies (Birn and Hesse, 1996; Rastätter *et al.*, 1999; Birn *et al.*, 1999) have shown that reconnection can be initiated in regions of finite resistivity by such an externally imposed convection electric field. A few studies have considered this possibility in regard to collisionless reconnection.

In a series of 2D and 3D PIC simulations, Horiuchi and collaborators (Horiuchi and Sato, 1994, 1997, 1999; Horiuchi *et al.*, 2001; Pei *et al.*, 2001) considered the effect of applying a very strong driving electric field with $E_y/v_{\rm A}B_0 \sim 0.5$–$1.0$ to a Harris neutral sheet. For the case of open downstream boundary conditions, they found that it was possible to achieve a steady-state reconnection configuration. These studies were not relevant to the onset problem, however. In 2D and 3D studies of the effect of imposing a more realistic ($E_y/v_{\rm A}B_0 \sim 0.1$) convection electric field on a near-Earth plasma sheet equilibrium configuration, Pritchett and Coroniti (1995) and Pritchett *et al.* (1997) found that this process resulted in the formation of a thin current sheet accompanied by the development of a deep minimum in the equatorial B_z field. There was no apparent difficulty in actually driving B_z negative, which then resulted in the tailward expulsion of a plasmoid. Possible limitations of this study were that $m_{\rm i}/m_{\rm e}$ was only 16 and that the reconnection occurred fairly close to the inner (near-Earth) boundary of the simulation.

Here we present some results from a recent 3D PIC simulation (Pritchett, 2005) in which a spatially localized convection electric field is applied to a current sheet equilibrium with $B_{\rm n}/B_0 = 0.04$ at the center of the sheet. The system size is $L_x \times L_y \times L_z = 25.6\,c/\omega_{\rm pi} \times 12.8\,c/\omega_{\rm pi} \times 12.8\,c/\omega_{\rm pi}$, and the driving field is localized near the center of the system in x with a half-width of $3.2\,c/\omega_{\rm pi}$. The field is applied at the z boundaries uniformly in y, and its peak magnitude is $E_y/v_{\rm A}B_0 = 0.2$. The mass ratio is $m_{\rm i}/m_{\rm e} = 100$, $c/v_{\rm A} = 20$, $\omega_{\rm pe}/\Omega_{\rm e} = 2.0$, the temperature ratio is $T_{\rm i}/T_{\rm e} = 5$, and there is a uniform background density $n_{\rm b} = 0.2n_0$. The initial half-thickness of the sheet is moderately large, with $\lambda = 1.6\,c/\omega_{\rm pi}$. The boundary conditions in the x direction are open for particles and magnetic flux. The peak number of particles is 412 million per species, and the maximum particle density per cell is 50 per species. The initial field line configuration is shown in Fig. 3.19a.

It has become traditional to describe the evolution of the reconnection process by the reconnection flux ψ (e.g., Birn *et al.*, 2001, and references therein), which is defined as the difference between the maximum and minimum values of the vector potential $A_y(x, z)$ on the axis $z = 0$. In the presence of the normal field component,

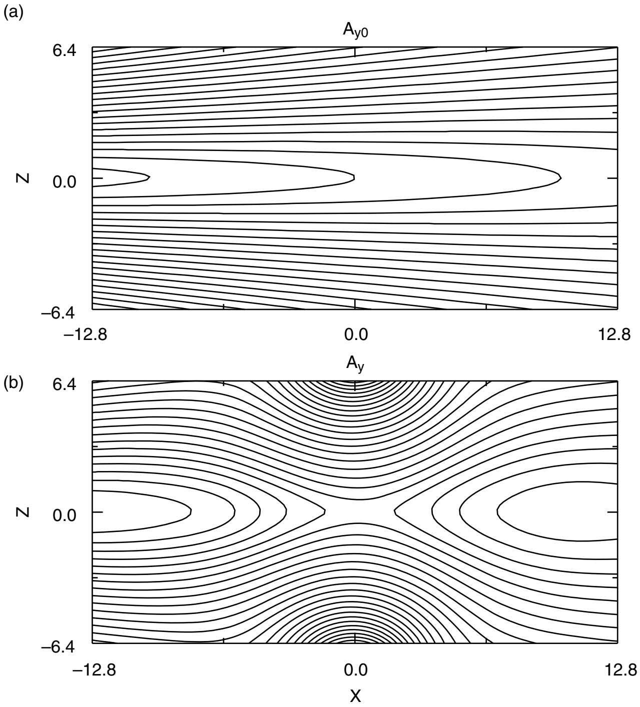

Fig. 3.19. Field line configuration at time (a) $\Omega_{\mathrm{i0}}t = 0$ and (b) $\Omega_{\mathrm{i0}}t = 36$.

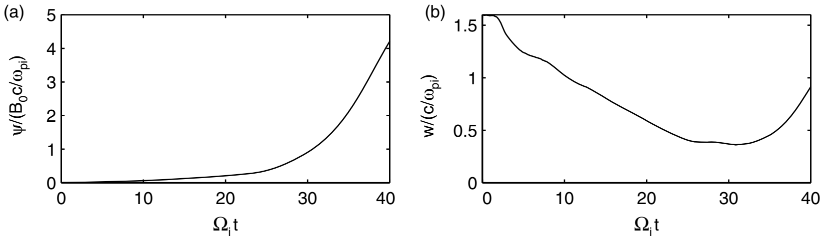

Fig. 3.20. Time histories of (a) the reconnected flux ψ and (b) the current sheet half-thickness w.

the equilibrium function $A_{0y}(x, z = 0)$ itself has a finite ψ value, and so it is necessary to measure ψ in terms of the perturbed $\delta A_y(x, z = 0)$ only. Figure 3.20a shows the development of ψ so defined. The initial noise level in the simulation corresponds to $\psi/(B_0 c/\omega_{\mathrm{pi}}) \sim 1 \times 10^{-3}$. There is a relatively long development period of $\Omega_{\mathrm{i0}}t \sim 20$ during which ψ grows slowly as the perturbation fields propagate in from the boundary. As shown in Fig. 3.20b, the width of the current layer, defined as the value w_J where $|B_x(0, w_J)| = 0.76B_0$, decreases during this period from its initial value of $1.6\,c/\omega_{\mathrm{pi}}$ to a minimum of $\sim 0.4\,c/\omega_{\mathrm{pi}}$. Subsequently, the value of ψ increases much more rapidly, with the peak slope at $\Omega_{\mathrm{i0}}t \sim 35$ corresponding to a reconnection field $E_y/v_A B_0 \approx 0.44$. This is more than twice as large as the driving value $E_{0y}/v_A B_0 = 0.2$, and it is somewhat larger than the value of ≈ 0.26 which was obtained from the GEM Reconnection Challenge simulations (Birn *et al.*, 2001) where a $\lambda = 0.5\,c/\omega_{\rm pi}$ current sheet was perturbed by an internal flux perturbation.

The thinning of the overall current layer is the result of the formation of an embedded thin electron current layer. Figure 3.21 shows a series of profiles in z at $x = 0$ and averaged over all values of y at various times for (a) the magnetic field B_x and (b) the total current density J_y. The overall thinning is apparent from the increasing magnitude of the slope of B_x through $\Omega_{\rm i0}t = 24$ and from the current density profiles. During this same time interval, the ion profiles $n_{\rm i}$, $v_{y\rm i}$, and $J_{y\rm i}$ (not shown) show relatively little change; there is only a modest steepening of the density profile. In contrast, the electron current density shows a dramatic thinning and increase in magnitude. At $\Omega_{\rm i0}t = 24$, the peak electron current density is about three times as large as that of the ions. This represents an increase by a factor of 15 in the relative electron to ion current value. The half-width at half-maximum of the electron current density at $\Omega_{\rm i0}t = 32$ is only $0.14c/\omega_{\rm pi}$, which is slightly above the local value of the electron inertial length of $\approx 0.12c/\omega_{\rm pi}$.

Figure 3.22a shows the development of the normal field profile $B_z(x, 0)$ averaged over all values of y. As noted before, the initial value is $B_z(x, 0)/B_0 = 0.04$. During the developmental phase this value is enhanced for negative values of x and reduced for positive values. $B_z(x, 0)$ is first driven to zero at $\Omega_{\rm i0}t \approx 21$ at $x \approx 2\,c/\omega_{\rm pi}$. At this time, there is only a weak y dependence in the equatorial B_z field (not shown); the growth rate for mode 1 in y is $\gamma/\Omega_{\rm i0} {\sim} 0.09$, which is consistent with the linear theory prediction for the ion–ion kink (Karimabadi *et al.*, 2003a). Overall, however, the cross-field modes do not seem to play a major role in the dynamics that force B_z to 0. Shortly after B_z is reversed, there is a significant increase in the reconnection flux ψ (Fig. 3.20a) and hence in the rate of reconnection. At this stage the reconnection proceeds much as for the case of a neutral sheet, and the late nonlinear stage (see Fig. 3.19b for the field lines at $\Omega_{\rm i0}t = 36$) shows little resemblance to the initial normal field configuration.

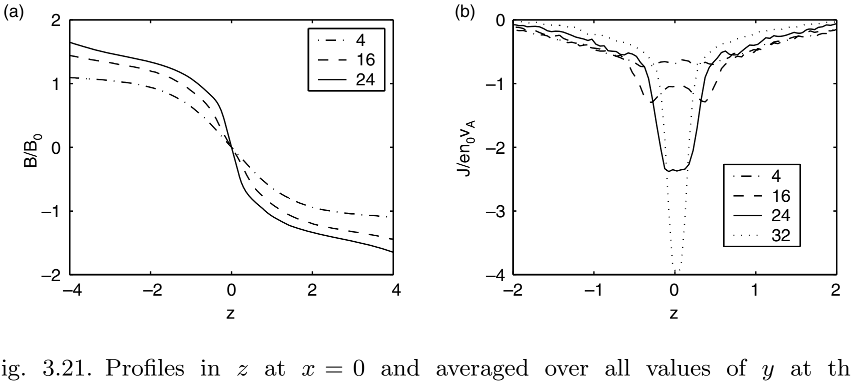

Fig. 3.21. Profiles in z at $x = 0$ and averaged over all values of y at the indicated times $\Omega_{\rm i0}t$ for (a) the magnetic field B_x and (b) the total current density J_y.

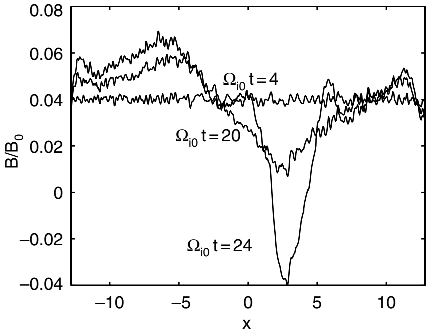

Fig. 3.22. Profiles in x at $z = 0$ and averaged over all values of y at the indicated times $\Omega_{\mathrm{i0}}t$ for the magnetic field B_z.

3.3.5 Summary and outlook

Investigations of collisionless magnetic reconnection in the terrestrial magnetotail must, at least for the near-Earth portion of the tail, confront the underlying 2D nature of the tail current sheet. Studies of magnetic reconnection in 1D current sheets do not suffice. This has led to the long history of the onset problem for reconnection in the tail. There are two basic issues associated with the presence of the normal field B_{n}. The first is that the ion gyromotion in B_{n} can disrupt the free-streaming motion that provides the collisionless damping to drive the tearing instability. Only if B_{n}/B_0 is smaller than its typical value of 0.1 and/or the current sheet is unusually thin ($\rho_{\mathrm{i0}}/\lambda \approx 1$) can one expect the spontaneous ion tearing instability to survive. Even this limited parameter space is probably excluded by the second effect, namely the electron stabilization. The various kinetic treatments based on the 2D analysis are now in general agreement that the ion tearing mode cannot exist in the transition region between dipole and tail fields where significant disruptions associated with substorm onset occur. The situation further down the tail is less clear.

The linear 2D tearing analysis, however, cannot provide the full story regarding reconnection in the magnetotail. A key feature of magnetospheric reconnection is that it occurs in bounded spatial regions which are, however, topologically open. Particles can ballistically enter the reconnection region, transit through it, and escape, perhaps never to return. The reconnected magnetic flux is also free to flow away from the reconnection region. The initial studies by Sitnov *et al.* (2002) suggest that these effects can alter significantly the previous results. The reconnection community has barely begun to address the consequences of a 3D open topology for reconnection.

A further complication of reconnection in real systems is its bimodal character. Not only does the kinetic physics near the X-line, which breaks the frozen-in condition, lead to large-scale consequences in terms of particle energization and magnetic flux reconfiguration, but the large-scale system reacts back on the local reconnection region in terms of the boundary conditions that are exerted on this region. Thus there is compelling statistical evidence that northward turnings of the IMF are frequently involved in triggering of substorms. Again, our quantitative understanding of the relevant physical processes is still at an elementary level.

Thus, while at one level the onset problem has been answered – the spontaneous ion tearing instability is unlikely to be operative in the magnetotail – at the more basic level we still do not understand the causal sequences that result in the large-scale reconnection processes associated with a substorm.

3.4 Hall MHD reconnection

A. Bhattacharjee and J. C. Dorelli

As discussed in Section 3.1, the classical models of Sweet–Parker and Petschek leave us with a quandary for low-resistivity plasmas (corresponding to high Lundquist numbers S; Section 2.1). On the one hand, the Sweet–Parker time scale is realizable dynamically in the high-S regime in high-resolution resistive MHD simulations, but it is too slow to explain dynamic processes such as solar flares or magnetospheric substorms. On the other hand, the Petschek model, which yields a faster time scale, appears not to be realizable in the high-S regime.

In addition, steady-state resistive models can provide but one time scale – that of steady reconnection (proportional to $S^{1/2}$ for Sweet–Parker and $\ln S$ for Petschek). However, steady reconnection is not a generic condition. It is a strong theoretical assumption and one that is frequently violated in many dynamical situations of great physical interest. In particular, there are phenomena involving magnetic reconnection in laboratory as well as space plasmas where the dynamics exhibits an impulsiveness, that is, a sudden increase in the time derivative of the growth rate. This is often referred to as the *trigger problem* – the magnetic field configuration evolves slowly for a long period of time, only to undergo a sudden dynamical change over a much shorter period of time. As the classical steady-state reconnection models of Sweet–Parker and Petschek do not include time dependency, they cannot account for the time evolution of the reconnection rate.

In this section, we present recent Hall MHD reconnection models that address the regime of very high Lundquist numbers S. We consider thin current sheets whose width Δ falls into the collisionless range between the electron and ion skin depths, that is, $d_\mathrm{e} \equiv c/\omega_\mathrm{pe} < \Delta \leq c/\omega_\mathrm{pi} \equiv d_\mathrm{i}$ (or $d_\mathrm{e} < \Delta \leq \rho_\mathrm{s}$ in the presence of a guide or toroidal field, where $\rho_\mathrm{s} = \sqrt{\beta} d_\mathrm{i}$). In this regime dissipation is governed by the generalized Ohm's law (3.4)

$$\mathbf{E} + \mathbf{v} \times \mathbf{B} = \eta \mathbf{j} + \frac{m_\mathrm{e}}{ne^2} \frac{\mathrm{d}\mathbf{j}}{\mathrm{d}t} + \frac{\mathbf{j} \times \mathbf{B}}{ne} - \frac{\nabla p_\mathrm{e}}{ne}. \tag{3.70}$$

Here the electron pressure p_e is assumed to be a scalar, and only a portion of the electron inertia term, $\mathrm{d}\mathbf{j}/\mathrm{d}t = \partial \mathbf{j}/\partial t + \mathbf{v} \cdot \nabla \mathbf{j}$, is retained. In contrast to the discussion of Section 3.2, we retain the Ohmic term (first term on the RHS), providing dissipation in competition with the electron inertial term (second term on the RHS). The last two terms on the right-hand side of Eq. (3.70), collectively referred to as the Hall MHD terms, do not contribute to the dissipation in this model. But, as discussed in Section 3.1, they govern whistler and kinetic Alfvén wave dynamics and may thus be responsible not only for fast reconnection but also for a plausible explanation of the trigger problem.

In the following sections we describe some recent analytical and numerical models that focus on the issue of scaling of Hall MHD reconnection in impulsive as well as quasi-steady regimes. It is difficult to determine scaling results by numerical computations alone simply because the range of parameters (such as the electron-to-ion mass ratio and the system size) that can be explored by nonlinear Hall MHD codes is still quite limited. It is therefore useful to consider reduced systems which are amenable to analytic treatment, can be tested and benchmarked numerically, and can be extrapolated to yield scaling results in realistic plasma regimes. In Section 3.4.1, we present results from a reduced collisionless model in which electron inertia provides the dominant mechanism for breaking field lines, and strongly time-dependent current singularities drive impulsive reconnection. In Section 3.4.2, we present results from a semi-collisional 2D Hall MHD model in which resistivity provides the mechanism for breaking field lines.

3.4.1 Impulsive Hall MHD reconnection

Here we present some analytical and numerical results from the so-called two-field model, which is deduced from the primitive Hall MHD equations by means of analytical approximations. The basic assumptions are a large guide field and low beta, so that the compressional wave propagates faster than any other wave in the system and the fluid motion is essentially incompressible. It is assumed that the resistivity is zero, and electron inertia breaks field lines. This model, which is simpler than the full two-fluid or Hall MHD equations, is amenable to analytical treatment in the linear as well as nonlinear regimes, and captures certain essential features of impulsive Hall MHD reconnection dynamics in collisionless plasmas. By a combination of analytical and numerical studies, we are able to obtain scaling results on the reconnection rate that can be compared with results obtained from other computational studies.

The dynamics is two-dimensional, and depends only on the coordinates x and z, with y as an ignorable coordinate. The magnetic field is represented as

$$\mathbf{B}(x,z,t) = B_0\hat{\mathbf{y}} + \nabla\Psi(x,z,t)\times\hat{\mathbf{y}}, \tag{3.71}$$

where B_0 is a constant and large guide field, and $\Psi(x,z,t)$ is a flux function. The velocity is represented as

$$\mathbf{v}(x,z,t) = \hat{\mathbf{y}}\times\nabla\Phi(x,z,t), \tag{3.72}$$

where $\Phi(x,z,t)$ is a stream function. The two-field equations are given by (Grasso *et al.*, 1999)

$$\partial F/\partial t + [\Phi, F] = \rho_{\mathrm{s}}^2[U,\Psi], \tag{3.73}$$

$$\partial U/\partial t + [\Phi, U] = [J,\Psi], \tag{3.74}$$

where $J = -\nabla_\perp^2\Psi$, $U = \nabla_\perp^2\Phi$, $F = \Psi + \mathrm{d}_\mathrm{e}^2 J$, and the Poisson bracket is defined by $[\Phi, F] \equiv \hat{\mathbf{y}}\cdot\nabla\Phi\times\nabla F$. In Eqs. (3.73) and (3.74), all quantities have been made dimensionless. In particular, distance is normalized by the characteristic equilibrium scale L_z in the z direction, and time is normalized by the Alfvén time scale $\tau_\mathrm{A} = \sqrt{\mu_0 n_0 m_\mathrm{i}}L_z/B_{y0}$ based on the magnetic field component B_{y0}. The two dimensionless parameters are the (normalized) electron skin depth $d_\mathrm{e} = c/(\omega_{\mathrm{pe}}L_z)$, where ω_{pe} is the electron plasma frequency, and the (normalized) ion sound gyro radius $\rho_{\mathrm{s}} = \sqrt{T_{\mathrm{e}}/m_{\mathrm{i}}}/(\Omega_{\mathrm{i}} L_z) = \rho_{\mathrm{i}}\sqrt{T_{\mathrm{e}}/T_{\mathrm{i}}}$ where T_{e} and T_{i} are the electron and ion temperatures, Ω_{i} is the ion cyclotron frequency, and ρ_{i} is the ion Larmor radius (also normalized by L_z). The term proportional to ρ_{s}^2 on the right of Eq. (3.73) is due to finite electron compressibility, and can be traced to the electron pressure gradient term in the generalized Ohm's law (3.70). The linearized versions of Eqs. (3.73) and (3.74) support kinetic Alfvén waves.

For the purpose of the present study, periodic boundary conditions are imposed in both x and z directions, with the domain of a single periodic cell given by $-L_x \leq x \leq L_x$, and $-L_z \leq z \leq L_z$. We choose $L_z = \pi$ and $L_x = \pi/\epsilon$, where $\epsilon = L_z/L_x$ is the slab aspect ratio. Due to the symmetry properties of Eqs. (3.73) and (3.74), we can consider $\Psi(\Phi)$ to be an even (odd) function in both x and z for all time, if it is so initially. In the following discussion we consider the linear and nonlinear evolution of the equilibrium given by $J_0 = \Psi_0 = \cos z$, $U_0 = \Phi_0 = 0$. It is doubly periodic, and is unstable with respect to double tearing modes, which grow around resonant surfaces, located at $z = 0$ and $\pm\pi$ in the periodic cell. Despite its apparent simplicity, the two-field model is computationally challenging, because it involves tracking near-singular and dynamic current sheets that grow near-explosively in the nonlinear regime. We use the Magnetic Reconnection Code (MRC) which is a massively parallel code in an Adaptive Mesh Refinement (AMR) framework (Bhattacharjee *et al.*, 2005).

To determine the linear instability of equilibria that depend only on z, we write $\Psi = \psi_0 + \psi_k(z,t)\cos(kx)$, where $k = m\epsilon$, m is an integer and ϵ is the aspect ratio defined earlier. The linear dispersion relation and growth rate of collisionless tearing modes in the two-field model have been obtained analytically using boundary-layer and asymptotic matching techniques (Porcelli, 1991). The analytic theory is mostly based on the large-Δ' approximation, i.e., $\Delta' d_{\mathrm{e}} \gg \min[1, (d_{\mathrm{e}}/\rho_{\mathrm{s}})^{1/3}]$, where $\Delta' = 2\sigma\tan(\sigma\pi/2)$, $\sigma = \sqrt{1-k^2}$.[2] The parameter Δ' is positive for $0 < k \leq 1$, which is necessary for instability. The large Δ' regime generally requires small k because Δ' is proportional to k^{-2} for small k, that is, small $m\epsilon$. When $0.5 \leq \epsilon < 1$, only the $m = 1$ mode is linearly unstable. For $\epsilon < 0.5$, a larger range of m-numbers are destabilized, up to a maximum mode number equal to integer (ϵ^{-1}). Bhattacharjee *et al.* (2005) have presented fairly comprehensive results on the linear instability of the system for arbitrary values of the parameters d_{e}, ρ_{s}, and k. These results generally confirm the predictions of analytic linear theory in the regime of large Δ' which generally requires small k. In the case $d_{\mathrm{e}} \gg \rho_{\mathrm{s}}$, when Δ' is large, the analytic theory predicts the linear growth rate $\gamma_{\mathrm{L}} \approx k d_{\mathrm{e}}$. For the case $d_{\mathrm{e}} \ll \rho_{\mathrm{s}}$, the analytic theory predicts $\gamma_{\mathrm{L}} \approx k(d_{\mathrm{e}}\rho_{\mathrm{s}}^2)^{1/3}$ in the large-Δ' regime. We note that the linear growth rates depend quite strongly on the aspect ratio (proportional to k), the parameter ρ_{s}, and even the electron inertia, which enters the parameter d_{e}, and provides the mechanism for breaking field lines. An important question is how these dependencies are altered in the nonlinear regime.

---

[2] The parameter Δ' governs the matching of a linear tearing mode between the external, ideal-MHD, solution and the internal solution in the dissipative layer (see, e.g., Biskamp, 2000). $\Delta' > 0$ is a necessary and sufficient condition for linear instability.

It can be shown, under certain strong assumptions (Ottaviani and Porcelli, 1993; Grasso *et al.*, 1999; Bhattacharjee *et al.*, 2005), that when $d_{\mathrm{e}} \neq 0,\ \rho_{\mathrm{s}} \neq 0$ the island half-width w, defined by the relation $\psi(0,0,t) = 1 - w^2(t)/2$, obeys the nonlinear equation

$$\frac{\mathrm{d}^2\hat{w}}{\mathrm{d}\tilde{t}^2} \approx \frac{1}{4}(\hat{w} + c_J \hat{w}^4), \tag{3.75}$$

where $\tilde{t} = \gamma_{\mathrm{L}} t$ is the time variable normalized by the linear growth rate γ_{L}, $\hat{w} \equiv w/\delta_{\mathrm{L}}$ where δ_{L} (equal to $d_{\mathrm{e}}^{1/3}\rho_{\mathrm{s}}^{2/3}$ in the large-Δ' regime) is the linear boundary-layer width, and c_J is a positive quantity, slowly varying in time, of the order of unity. We note that $\psi(0,0,t=0) = 1$ and $w(0) = 0$, and we have included a factor of 1/4 in the first term of Eq. (3.75) because w grows exponentially with half of the linear growth rate γ_{L}. Equation (3.75) predicts that the island width grows near-explosively in the nonlinear regime. By the time w becomes of the order of the system size, most of the magnetic flux is reconnected, and the near-explosive growth of the island is quenched. (The quenching process is not described by Eq. (3.75), which breaks down when w becomes of the order of the system size.)

It is worth noting that the tendency for the formation of a current singularity and island blow-up is already inherent in this problem due to the presence of finite electron inertia even when $\rho_{\mathrm{s}} = 0$. It is in this sense that we describe the current singularity as a driver of impulsive reconnection. The analytical model also predicts that the linear as well as the nonlinear reconnection rate does depend on the system size (that is, k). In what follows, we will test the predictions of this analytical model with numerical simulations using the MRC.

Figure 3.23 is a typical image plot of the current density $J(x,z,t) = -\nabla_\perp^2 \psi$ in the nonlinear regime. This picture illustrates the usefulness of AMR grids in resolving intense and thin current sheets produced during collisionless reconnection dynamics. The magnified images in the smaller inserts show clearly the detailed spatial structure

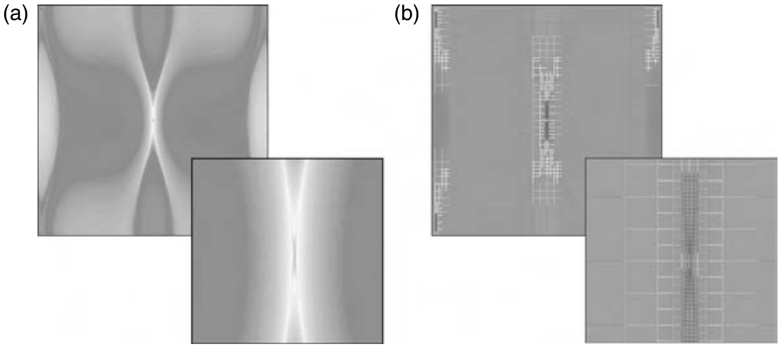

Fig. 3.23. (a) Current density in the nonlinear phase. The smaller inserts are magnified images of the near-singular current sheet at the X-point, showing how AMR enables resolution of the fine structure. (b) We overlay the plot with a visualization of the adaptive grids, as they provide higher resolution near the small-scale structures as needed. See also color plate.

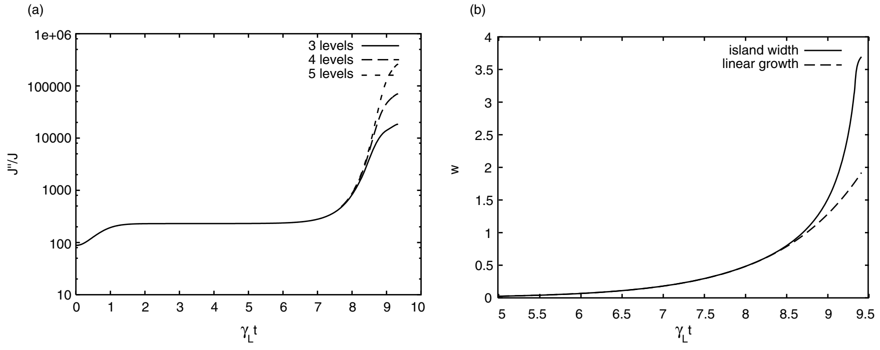

Fig. 3.24. (a) Plot of $J^{-1}(\partial^2 J/\partial x^2)$ at the origin, which is inverse square of the thin current sheet width. Very high resolution is needed to follow the rapidly shrinking current width. (b) Plot of the time evolution of the island width.

in the vicinity of an X-point, which is a signature of collisionless fast reconnection, and the AMR grids used to resolve them.

Figure 3.24a shows a plot of $J^{-1}(\partial^2 J/\partial x^2)$ at the origin, which is essentially the reciprocal of the square of the current sheet width. After a period of exponential growth, this quantity tends to increase very rapidly, consistent with the analytical prediction given by Bhattacharjee *et al.* (2005). We show this plot for three different levels of AMR. It is clear by inspection that the higher the level of AMR, the longer is the blow-up phase, before the process saturates. Figure 3.24b shows a plot of the time evolution of the island width.

In Fig. 3.25, we compare the simulation result from the MRC with the island equation (3.75) for the same parameters as Fig. 3.24. (Note that the ordinate is plotted on a logarithmic scale.) As mentioned above, the constant c_J is not fixed by our analysis. We find that $c_J \approx 0.1$ provides a reasonably good fit for the simulation results.

Shay *et al.* (1999, 2004) have presented extensive numerical results in support of their claim that the reconnection eventually evolves into a late nonlinear phase, which they call the *asymptotic phase*, when the reconnection rate becomes of the order of one-tenth of the Alfvén speed (based on the magnetic field just upstream of the reconnection layer), independent of the electron and the ion skin depth as well as the system size. (See also Section 4.1.) We revisit this question here because the initial condition for the magnetic field used by Shay *et al.* is very similar to the one used here for the field in the x, z plane, perpendicular to the guide field. There are, however, significant differences between our model and theirs. Shay *et al.* use the full Hall MHD equations and take the equilibrium guide field to be zero. We consider an equilibrium with a large and constant guide field, and integrate the reduced two-field equations which are obtained from the full Hall MHD equations in the limit of large toroidal field and low beta. Despite these differences, it is instructive to compare our results with those of Shay *et al.*, because there is no doubt that both simulations exhibit an asymptotic phase. (In these simulations, we explore parameter regimes in which reconnection proceeds nonlinearly to form islands with widths of the order of the system size so that the inequality $z \ll \rho_s, d_e$ is realized.) We suggest that the

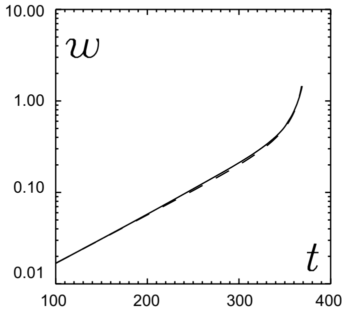

Fig. 3.25. Island half-width $\hat{w}$ as a function of time from numerical simulation (solid curve) and from Eq. (3.75) with $c_J = 0.1$ (dashed curve), for the case with $\rho_s = 0.2$, $d_e = 0.1$, $k = 0.5$, $\gamma_L = 0.0024$.

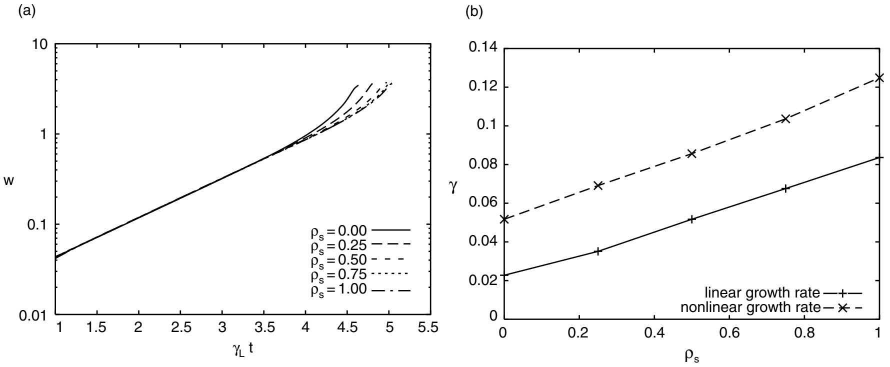

Fig. 3.26. (a) Island width time evolution for different values of ρ_s for $d_e = 0.25$, $\epsilon = 0.5$, in rescaled (with linear growth rate) time. (b) Linear and nonlinear growth rates (at fixed island size) for the runs in Fig. 3.26a.

instantaneous reconnection rate, as measured by the rate of change of the island width (which is proportional to the inflow velocity towards the X-point) is a good diagnostic with which we can test the claim regarding asymptotic reconnection rates.

Figure 3.26a shows five plots of the island width as a function of $\gamma_L t$, where γ_L is the linear growth rate, determined numerically from the MRC for the parameters $d_e = 0.1$ and $\rho_s = 0$, 0.25, 0.5, 0.75, 1.0, holding the aspect ratio ϵ fixed at the value 0.5. We observe that the five plots essentially lie on top of each other for most of the time interval during the evolution of the instability. In other words, the equation $w = w(\gamma_L t)$ is a reasonably good description for the island width evolution for most of the time interval. Had this been the whole story, the issue of scaling of the reconnection rate would be completely settled, and we could claim, following Ottaviani and Porcelli (1993, 1995), that the instantaneous reconnection rate at all times scales as the linear growth rate, which is given by $\gamma_L = k(d_e \rho_s^2)^{1/3}$ in the large-Δ' regime. In turn, this would imply that the reconnection rate is not a "universal constant," and depends on the aspect ratio as well as d_e and ρ_s. Under these conditions, the dependence on the electron mass, which provides the mechanism breaking field lines, is weak (proportional to $m_e^{-1/6}$) but nonetheless significant because it establishes the point of principle that the reconnection rate is not independent of the parameter that breaks field lines and controls the structure of the current sheet.

We note, however, that the equation $w = w(\gamma_L t)$ is not quite the whole story. The five curves in Fig. 3.26a do not lie on top of each other in the late nonlinear phase, although they tend to be quite close to doing so as the ratio d_e/ρ_s becomes larger. In order to determine numerically the scaling behavior of the time-dependent growth rate in the late nonlinear (or asymptotic) phase, we choose to examine the nonlinear growth rate at a fixed size of the island width ($w = 2$), which falls right in the middle of the late nonlinear phase. (The choice $w = 2$ is admittedly ad hoc, but our qualitative conclusions regarding the late nonlinear phase do not depend on this specific choice.) Figure 3.26b shows the plots of γ_{NL} for the five values of ρ_s given above at fixed island size. For comparison, we also plot γ_L for the same values of ρ_s. From inspection of Fig. 3.26b, we conclude that although the growth rate in the late nonlinear regime shows deviation from the equation $w = w(\gamma_L t)$, this growth rate scales with ρ_s in approximately the same way as γ_L does. A similar conclusion holds for the dependence of the growth rate on d_e in the late nonlinear phase.

We now investigate the dependency of the asymptotic growth rate on the aspect ratio ϵ. Figure 3.27a shows five plots of the island width as a function of $\gamma_L t$, where γ_L is the linear growth rate, determined numerically for fixed $d_e = 0.25$ and $\rho_s = 0.75$, and five different values of the aspect ratio given by $\epsilon = 0.1$, 0.2, 0.3, 0.4, 0.5. Once again, we observe that the five plots essentially lie on top of each other for most of the time interval during the evolution of the instability. In other words, in this case too the equation $w = w(\gamma_L t)$ is a reasonably good description for the island width evolution for most of the time interval. This would imply a strong dependence of the reconnection rate on k, in contrast with the conclusion of Shay and coworkers. However, as in Fig. 3.26a, we note that the five curves in Fig. 3.27a do not lie on top of each other in the late nonlinear phase. So in order to determine numerically the dependence of the time-dependent growth rate on the aspect ratio in the late

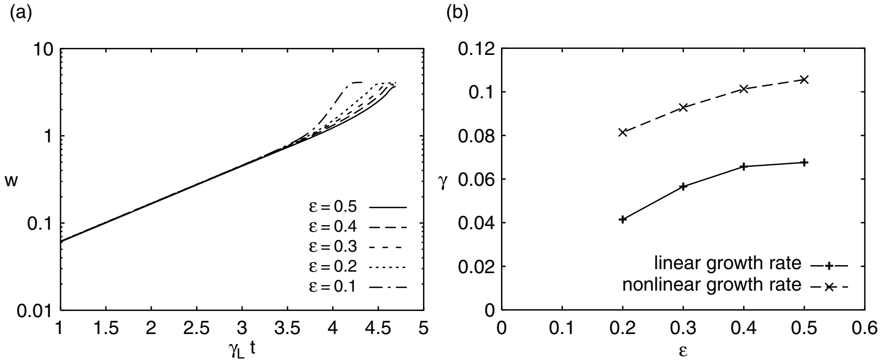

Fig. 3.27. (a) Island width time evolution for different values of ϵ for $\rho_s = 0.75$, $d_e = 0.25$ in rescaled (with linear growth rate) time. (b) Linear and nonlinear growth rates (at fixed island size) for the runs in Fig. 3.27a.

nonlinear phase, we choose to examine the nonlinear growth rate at a fixed size of the island width ($w = 2$).

Figure 3.27b shows the plots of γ_{NL} for four values of ϵ at fixed island size. For comparison, we also plot γ_{L} for the same values of ϵ. From inspection of Fig. 3.27a, we conclude that although the growth rate in the late nonlinear regime shows deviation from the equation $w = w(\gamma_{\mathrm{L}} t)$, this growth rate clearly exhibits a definite dependency on ϵ. However, this dependency of the nonlinear growth rate on ϵ appears to be a little weaker than the dependency of γ_{L} on ϵ.

In summary, we have presented linear and nonlinear results on collisionless reconnection in a two-field model, valid in the regime of high guide (or toroidal) field and low plasma beta. In this model, electron inertia breaks field lines, and two-fluid (or Hall MHD) effects enter via the electron pressure gradient term in the generalized Ohm's law. The two parameters representing electron inertia and pressure gradient are d_{e} and ρ_{s}, respectively. Even if $\rho_{\mathrm{s}} = 0$, the system of equations exhibits near-explosive nonlinear growth of current sheet amplitude and magnetic island width. In the regime $\rho_{\mathrm{s}} > d_{\mathrm{e}}$ the tendency for near-explosive growth persists, but we repeat for emphasis that this tendency is already inherent in the system without ρ_{s}. Thus, in the present model, current singularities drive impulsive reconnection, and it is not surprising that the scaling properties of this system exhibit dependency not only on ρ_{s} but also on d_{e}, which breaks field lines and controls the structure of the current sheet. This type of dynamics has been studied by Shay *et al.*, who have suggested that the reconnection rate tends to a "universal" rate of the order of one-tenth of the Alfvén speed (where the Alfvén speed is calculated using the upstream magnetic field strength) in the late nonlinear regime. We have demonstrated that the reconnection rate in the late nonlinear regime of the two-field model attains no such "universal" behavior, but depends on d_{e} and ρ_{s} in approximately the same way as the linear growth rate. We have also demonstrated that this reconnection rate depends on the aspect ratio (or the system size), although this dependency is a little weaker in the late nonlinear regime than it is in linear theory. These dependencies cast some doubt on heuristic analyses which use linear wave dispersion relations to make strong conclusions regarding "universal" reconnection rates in nonlinear regimes.

As discussed above, one of the significant qualitative consequences of the present study is that the dynamics and scaling properties of Hall MHD or two-fluid collisionless reconnection models are not independent of the mechanism that breaks field lines. In the present context, electron inertia is that mechanism, and it introduces filamentary and rapidly time-varying current density structures that persist through the linear as well as nonlinear regimes, and produce dynamics that is quite different than resistive MHD dynamics. That this is so for linear theory has been known for a long time, but the effect persists also in the nonlinear regime of the present model. Thus, in problems of time-dependent collisionless reconnection, current singularities that are dominantly controlled by electron inertia cannot, in general, be assumed to be a sideshow to ion-controlled reconnection. As the nature and dynamics of the current singularities do depend on whether resistivity or electron inertia breaks field lines, the sensitivity of the reconnection rate to these rather different mechanisms can be different.

3.4.2 Resistive Hall MHD reconnection scaling: Role of flux pile-up

We now present analytical and numerical results in a quasi-steady Hall MHD reconnection model where resistivity is the mechanism that breaks field lines. (This complements the study in Section 3.4.1, where electron inertia breaks field lines and the system is strongly time-dependent and impulsive.) While the results of the GEM Reconnection Challenge (Birn *et al.*, 2001) suggest that Hall electric fields can, by themselves, allow magnetic reconnection to occur on time scales which are much shorter than the Sweet–Parker time scale, the question of how this reconnection rate scales with the system size was not addressed by the GEM challenge. Answering this question is particularly important in the context of the solar corona, where the ion inertial length can be smaller than the length of a typical coronal arcade by a factor of ten million. As discussed in Section 3.1.2, Shay *et al.* (1999, 2004) have argued that the *ion inertial region* – the spatial region over which electron and ion bulk velocities decouple – in a 2D reconnection process should have a thickness of the order of an ion inertial length, and a width of the order of ten ion inertial lengths. Thus, they argue that a Sweet–Parker analysis of the ion inertial region implies that the reconnection inflow speed should be about a tenth of an Alfvén speed and insensitive to the system size. In an earlier paper, Biskamp *et al.* (1997) had pointed out that, although the quasi-steady reconnection rate may be insensitive to the mechanism that breaks field lines (consistent with the GEM challenge results), the formation of a macroscopic *ion inertial sheet* (analogous to the Sweet–Parker current sheet in resistive MHD) cannot be ruled out. Subsequent studies (Wang *et al.*, 2001; Dorelli and Birn, 2003; Fitzpatrick, 2004) seem to be consistent with the conjecture advanced by Biskamp *et al.*

In this section, we will approach the problem from a different perspective that draws on an analogy between the current debate about system size scaling and the Petschek versus Sweet–Parker debate of the last several decades. In particular, Biskamp's (Biskamp, 1986) numerical experiments suggested that driven magnetic reconnection occurs, in the context of resistive MHD, via a process of magnetic flux pile-up (see also Parker, 1973b; Sonnerup and Priest, 1975; Priest and Forbes, 1986) rather than in a Petschek configuration. In flux pile-up reconnection, magnetic energy accumulates upstream of a Sweet–Parker current sheet to accommodate a sub-Alfvénic inflow velocity. As the plasma resistivity is decreased, the magnetic pile-up increases, compensating for the resulting decrease in the inflow velocity (which scales like the square root of the resistivity in the Sweet–Parker model); thus, the reconnection rate is insensitive to the plasma resistivity.

However, momentum conservation considerations prevent this resistivity-independent reconnection rate from being realized at arbitrarily small resistivities (Priest, 1996; Litvinenko, 1999). Since the plasma inflow Alfvén Mach number is much less than one, and there is a finite upstream pressure available to drive this sub-Alfvénic inflow, there must be an upper limit to the amount of magnetic energy which can accumulate upstream of the current sheet. Thus, one expects to observe two distinct regimes of flux pile-up reconnection: a presaturation phase, in which the reconnection rate is insensitive to the plasma resistivity; and a postsaturation phase, in which the reconnection rate scales strongly with plasma resistivity.

In principle, one can generalize the above arguments to address the scaling of Hall MHD reconnection with system size. Just as the strong scaling of magnetic pile-up with resistivity in resistive MHD implies that the reconnection rate scales strongly with resistivity in the postsaturation regime, a strong scaling of magnetic flux pile-up with the ion inertial length in Hall MHD implies (by arguments very similar to those made by Litvinenko, 1999) that the reconnection rate scales strongly with the system size (i.e., the ratio of the characteristic system length to the ion inertial length). We illustrate this argument with a simple example (see Dorelli, 2003, for details).

Consider the following incompressible stagnation point flow field:

$$U_x = U_0(x/\lambda), \tag{3.76}$$

$$U_z = -U_0(-z/\lambda), \tag{3.77}$$

where U_0 is a constant with dimensions of speed, and λ is a length scale characterizing the stagnation point flow. If we assume that the magnetic field is unidirectional, $\mathbf{B} = B_x(z)\hat{\mathbf{x}}$, and that $B_x(0) = 0$, then the flow field (3.76) and (3.77) describes the annihilation of antiparallel magnetic fields (in the x, z plane) at a one-dimensional current sheet, with the current flowing in the y direction. One can demonstrate (see, for example, Parker, 1973b; Sonnerup and Priest, 1975) that such a flow field solves the momentum and continuity equations; the magnetic field profile is then determined from Ohm's law, and the thermal pressure, $p(x, z)$, is determined by the conditions of pressure balance:

$$p(x,z) = p_0(x) - \frac{1}{2}\rho U^2 - \frac{B^2}{2\mu_0}, \tag{3.78}$$

where ρ is the plasma density (hereafter assumed to be constant), and p_0 is a constant. As described by Dorelli (2003), one can generalize the analysis of Sonnerup and Priest (1975) to obtain solutions which describe the pile-up of magnetic energy upstream of the current sheet:

$$B_x(\zeta) = E_y\left(\frac{S}{U_0}\right)^{1/2} \exp\Big(-\frac{1}{2}\alpha\zeta^2\Big)\int_0^{\zeta} \exp\Big(-\frac{1}{2}\alpha u^2\Big)\,\mathrm{d}u \tag{3.79}$$

where $\zeta = (SU_0)^{1/2}z$, $\alpha = 1 + S\delta_\mathrm{i}C$, S is the Lundquist number ($S = \mu_0\lambda v_\mathrm{A}/\eta$), $\delta_\mathrm{i} = d_\mathrm{i}/\lambda$, and C is an arbitrary constant.

Figure 3.28 shows the magnetic field profile given by (3.79) for various values of the ion inertial scale; clearly we can see that, for a fixed Lundquist number, the pile-up scales with δ_i. Thus, if we define "system size" to be the scale of the stagnation point flow, then we see that the flux pile-up required to support a given inflow decreases as the system size decreases. Specifically, if $B_x^{\max}$ is the magnitude of B_x at the location of its local maximum, then:

$$B_x^{\max} = E_y\left[\frac{2S}{U_0(1+S\delta_\mathrm{i}C)}\right]^{1/2} D_+(\chi), \tag{3.80}$$

where $D_+(\chi)$ is Dawson's integral (Abramowitz and Stegun, 1964),

$$D_+(u) = \mathrm{e}^{-u^2}\int_0^u \mathrm{e}^{t^2}\,\mathrm{d}t, \tag{3.81}$$

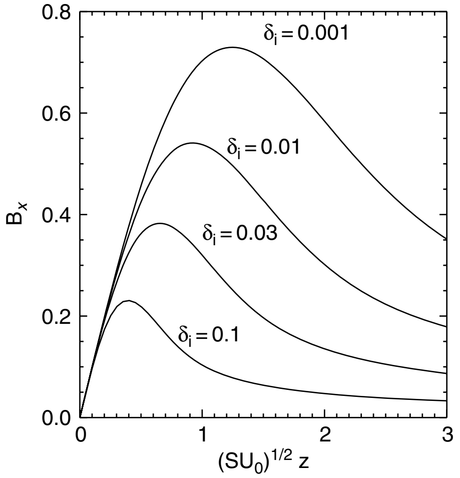

Fig. 3.28. The $(x, z$ plane) magnetic field component (3.79) is shown for several values of δ_i.

and the current sheet thickness χ follows from $1/(2\chi) = D_+(\chi)$. Thus, as the Lundquist number approaches infinity, the magnetic flux pile-up saturates at a level which is independent of the Lundquist number:

$$B_x^{\rm sat} = E_y\Big(\frac{2}{\delta_{\rm i}C}\Big)^{1/2} D_+(\chi). \tag{3.82}$$

Figure 3.29a shows the maximum upstream magnetic field, given by (3.81), as a function of S, where we have set $E_y = 0.009$, $U_0 = 0.1$, and $C = 0.01$. As shown in Fig. 3.29b, a similar pile-up saturation effect, with the saturation level strongly dependent on the ion inertial length (and insensitive to the Lundquist number) in the high-Lundquist number limit, was observed in resistive Hall MHD simulations of magnetic island coalescence (Dorelli and Birn, 2003).

While the observation of flux pile-up in an island coalescence process is not surprising, since such pile-up has been observed previously in the context of resistive MHD (Biskamp, 1986), the δ_i-dependent saturation of the pile-up observed in the Hall MHD runs has implications for the scaling of the reconnection rate with system size. Following Litvinenko (1999), the maximum flux pile-up reconnection rate may be estimated by constraining the upstream plasma pressure to be positive. One obtains (Dorelli, 2003):

$$E_y \approx 1.31(\beta U_0)^{1/2}\Big(\frac{1+S\delta_{\rm i}C}{S}\Big)^{1/2}. \tag{3.83}$$

When the system size is very large (i.e., when $\delta_{\rm i}$ approaches 0), the maximum reconnection rate decreases as the square root of the Lundquist number; however, for any finite system size, a limit is always reached (for large enough S) in which the reconnection electric field becomes insensitive to S. In this limit, however, the electric field scales strongly with system size ($E_y \propto \delta_{\rm i}^{1/2}$). This dependence of the asymptotic (as

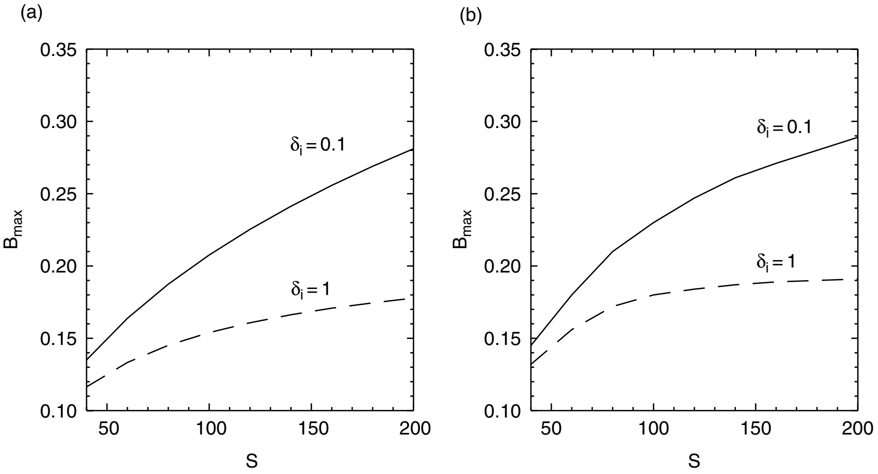

Fig. 3.29. The local maximum of the magnetic field B_x in the pile-up region as a function of the Lundquist number S: (a) from the analytic model given by (3.81); (b) obtained from a simulation of magnetic island coalescence, upstream of the current sheet between the coalescing islands (Dorelli and Birn, 2003).

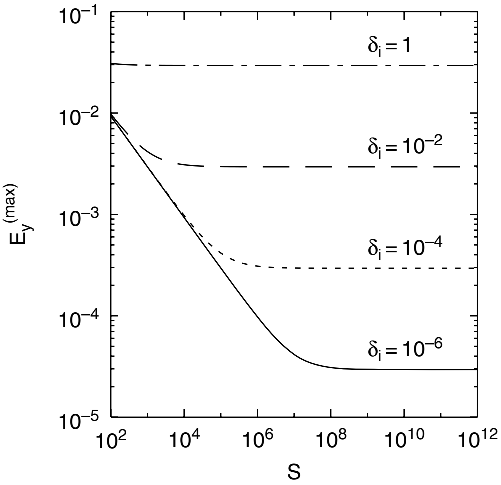

Fig. 3.30. Maximum reconnection electric field (3.83) as a function of S and system size.

S approaches infinity) maximum reconnection electric field on system size is shown in Fig. 3.30.

The physical reason for the reduction in pile-up in Hall MHD flux pile-up reconnection can be understood as a consequence of the spatial structure of the guide field. This field has the form (Dorelli, 2003) $B_y = C\xi\zeta$, where C is an arbitrary constant, $\xi = (SU_0)^{1/2}x$, and $\zeta = (SU_0)^{1/2}z$. From Ampère's law, we can interpret the guide field as a stream function for the current density in the x, z plane. Thus, if the ion inflow velocity is fixed, then the guide field describes an electron stagnation point flow, the magnitude of which is determined by the first derivatives of B_y near the origin. Thus, if C is independent of the plasma resistivity (i.e., if the first derivatives of the guide field scale inversely with the plasma resistivity), then the magnitude of the electron flow in the x, z plane scales like the square root of S, and less pile-up of magnetic energy is required upstream of the current sheet to support a given reconnection electric field. In other words, fast electron flows may transport magnetic flux into the current sheet without requiring a compensating drop in plasma pressure (so long as the large first derivatives of B_y are spatially localized within the ion inertial layer).

What, then, can we say about the scaling of the Hall MHD reconnection rate with system size? It appears that if Hall MHD reconnection occurs via a magnetic flux pile-up mechanism, where the magnetic pile-up is sensitive to the system size (see for example Wang *et al.*, 2001; Dorelli and Birn, 2003), then one expects to observe, in the large Lundquist number limit, a pile-up saturation effect which renders the reconnection rate sensitive to the system size. To settle this question conclusively, we will have to extend our analytic work to address much more general classes of problems than the one addressed in this section.

3.5 Role of current-aligned instabilities

J. Büchner and W. S. Daughton

In this section we return to the discussion of collisionless mechanisms that might generate nonideal contributions to the electric field $\mathbf{E} + \mathbf{v} \times \mathbf{B} = \mathbf{E}'$, providing dissipation $\mathbf{j} \cdot \mathbf{E}' \neq 0$. Section 3.2 focused on mechanisms that operate even in the absence of modes in the direction of the main current in a reconnecting current sheet. Here we discuss the particular role of current-aligned modes, that is, modes with a wave vector component k_y in the direction of the main current. (Since most of the applications are made to the magnetotail current sheet, we continue to use a magnetospheric coordinate system with x in the direction of the main magnetic field, y in the direction of the current, and z perpendicular to the current sheet.) There are several ways in which such modes might play a role.

Current-aligned modes might directly generate dissipative electric fields. In contrast to the DC electric fields discussed in Section 3.2, this influence involves net effects of alternating or fluctuating electric fields. This represents the classical concept of *anomalous resistivity*, which also entails the idea that the dissipative electric field depends on the local plasma properties, most specifically, the local current density. In the simplest case, this relationship would be governed by Ohm's law, with $\mathbf{E}'$ proportional to $\mathbf{j}$. However, more generally the factor between $\mathbf{E}'$ and $\mathbf{j}$ need not be a constant nor a scalar. Anomalous resistivity due to low-frequency plasma turbulence was considered in numerous papers, based, for instance, on ion-acoustic waves or lower-hybrid drift (LHD) waves (see, e.g., Rowland and Palmadesso, 1983).

But there is also the possibility that unstable current-aligned plasma waves may indirectly and nonlinearly interact with reconnection. Current-aligned modes might alter the structure of the current sheet and thereby change the stability properties and the early (linear) evolution or they might play a role in the nonlinear dynamic evolution. Modes of particular interest in this kind of interaction are unstable kink- or sausage-type modes of the current sheet and the lower-hybrid drift instability.

In the following we review key theoretical and simulation results and discuss their applicability to experimental and observational findings of current-aligned instabilities as well as their potential importance for reconnection. We focus particularly on lower-hybrid drift modes and kink modes, which are well observed in the magnetosphere. Ballooning modes, driven by pressure gradients in the direction of the magnetic field curvature, will be discussed in Section 4.3. These modes operate also in the ideal MHD limit, although collisionless effects might provide important modifications.

3.5.1 Ion-acoustic instability

A current-driven instability which may cause anomalous resistivity in current sheets is the *ion-acoustic* (also called *ion-sound*) instability (e.g., Manheimer and Flynn, 1971). For space applications it was considered by Kan (1971). Ion-acoustic waves are unstably excited by a resonant interaction of drifting electrons or ions with the electric field oscillations of ion-sound waves (e.g., Krall, 1977), thereby providing momentum exchange between ions and electrons. Ion-sound waves propagate in plasmas with $T_\mathrm{e} \gg T_\mathrm{i}$ but become strongly Landau-damped when $T_\mathrm{e} \approx T_\mathrm{i}$. In the Earth's magnetosphere, the proton temperature is typically about 5 to 10 times larger than the electron temperature, so that ion-acoustic waves are strongly damped. As a result anomalous resistivity due to dissipation of ion-acoustic waves was expected mainly in laboratory plasmas, e.g. theta-pinch experiments (Liewer and Krall, 1973) and solenoidal fusion systems (Davidson *et al.*, 1977). Considering space plasmas, Coroniti (1985) concluded that anomalous resistivity resulting from the quasi-linear saturation of ion-acoustic instability is much too small to account for fast reconnection.

Considerably larger wave amplitudes could, however, be expected for stronger driven currents, for which ion-acoustic instabilities may develop even in plasmas with $T_\mathrm{i} \approx T_\mathrm{e}$. Also, instead of the usually applied one-dimensional quasi-linear theory which leads to plateau formation stopping wave generation, two-dimensional scattering of the electrons at ion fluctuations should be considered. The investigation of such systems can be carried out, however, only by means of numerical simulations, for which Vlasov-code simulations are most appropriate. Even one-dimensional recent Vlasov-code simulations (Watt *et al.*, 2002; Petkaki *et al.*, 2003) claimed a much stronger wave excitation than the one predicted by the one-dimensional quasi-linear theory. These findings revived the interest in the ion-acoustic instability as a possible mechanism for collisionless dissipation in space plasmas. Since these simulations were restricted to low mass ratios, Hellinger *et al.* (2004) and Büchner (2005) repeated the simulations for the same parameters as Watt *et al.* (2002) and Petkaki *et al.* (2003), but for the realistic proton/electron mass ratio $m_\mathrm{i}/m_\mathrm{e} = 1836$, using more accurate Vlasov solvers (see, e.g., Elkina and Büchner, 2005). As a result it appeared that for realistic mass ratios the old quasi-linear estimate can be recovered within an order of magnitude. It has still to be investigated, however, whether dissipation becomes sufficient to support reconnection in more realistic two- and three-dimensional cases, which permit pitch-angle scattering, or under, quasi-stationary, continuous current flow conditions, driven by external forces.

3.5.2 Lower-hybrid drift instability

Waves in the lower-hybrid frequency range,

$$\Omega_{\mathrm{LH}} = \omega_{\mathrm{pi}}(1+\omega_{\mathrm{pe}}^2/\Omega_{\mathrm{e}}^2)^{-1/2}, \tag{3.84}$$

where ω_{pi} and ω_{pe} are the ion and electron plasma frequencies, respectively, and Ω_{e} is the electron cyclotron frequency, are commonly observed in the current sheets at the Earth's magnetopause (e.g., Vaisberg *et al.*, 1983; André *et al.*, 2001; Lucek *et al.*, 2001; Bale *et al.*, 2002; Vaivads *et al.*, 2004a), the magnetotail (e.g., Gurnett *et al.*, 1976; Pu *et al.*, 1981) and in laboratory plasmas (e.g., Takeda and Inuzuka, 2000; Carter *et al.*, 2002b). They arise from the *lower-hybrid drift* (LHD) instability driven by diamagnetic drifts associated with strong pressure gradients, particularly in the boundary regions of the current sheets (Gary and Eastman, 1979; Labelle and Treumann, 1988).

The kinetic LHD instability (LHDI) requires gradients $L/\rho_{\mathrm{i}} \lesssim (m_{\mathrm{i}}/m_{\mathrm{e}})^{1/4}$ where L is the characteristic density scale length. This condition is easily satisfied in magnetospheric plasmas (Huba *et al.*, 1978). For weaker gradients $(m_{\mathrm{i}}/m_{\mathrm{e}})^{1/4} < L/\rho_{\mathrm{i}} < (m_{\mathrm{i}}/m_{\mathrm{e}})^{1/2}$, the LHDI transforms into the *drift cyclotron* instability (Freidberg and Gerwin, 1977). In the opposite limit of strong plasma pressure gradients $L \lesssim \rho_{\mathrm{i}}$, the LHDI becomes a fluid instability, excited through the coupling of a lower-hybrid wave with a drift wave (Huba *et al.*, 1978).

In magnetospheric plasmas, where usually $\omega_{\mathrm{pe}}^2 \gg \Omega_{\mathrm{e}}^2$, the expression for the lower-hybrid frequency simplifies to $\Omega_{\mathrm{LH}} \approx (\Omega_{\mathrm{i}}\Omega_{\mathrm{e}})^{1/2}$. Simple linear theory predicts that the fastest growing LHD waves are on the electron gyroscale $k_y\rho_{\mathrm{e}} \sim 1$, while more generally, due to nonlinear effects, a broad spectrum of wavelengths may be excited, reaching up to $k_y\sqrt{\rho_{\mathrm{e}}\rho_{\mathrm{i}}} \sim 1$. Unstable LHD waves propagate with diamagnetic drift velocity perpendicular to the local magnetic field (Krall and Liewer, 1971; Liewer and Krall, 1973; Huba *et al.*, 1977).

Perhaps the most attractive feature of LHDI over other current-driven instabilities such as ion-acoustic or Buneman instability, is that it persists for a much broader range of interesting parameters (i.e., weaker drifts and $T_{\mathrm{e}} < T_{\mathrm{i}}$). The quasi-linear saturation of the LHDI and the corresponding anomalous dissipation is well known (e.g., Davidson and Gladd, 1975). The LHDI therefore has been considered extensively as a possible candidate to enable reconnection through anomalous resistivity generated by wave–particle interactions (Huba *et al.*, 1977, 1980; Winske, 1981; Tanaka and Sato, 1981). However, for a typical current sheet structure, nonlocal kinetic theory predicts that the fastest growing modes are well localized on the edge of the current layer while enhanced fluctuations are required in the central region to produce significant anomalous resistivity (Huba *et al.*, 1980). The effects of finite plasma β and the electron ∇B drift-wave resonance damp the mode in the central region and limit the penetration to distances greater than $\sim L(T_{\mathrm{e}}/2T_{\mathrm{i}})^{1/2}$, where L is the half-thickness of the sheet. For the fastest growing short-wavelength modes $k_y\rho_{\mathrm{e}} \sim 1$, this conclusion is supported by kinetic simulations (Tanaka and Sato, 1981; Winske, 1981; Brackbill *et al.*, 1984), observations at the magnetopause (Bale *et al.*, 2002), in the magnetotail (Shinohara *et al.*, 1998), and also by laboratory experiments (Carter *et al.*, 2002a,b).

Although the fastest growing linearly unstable LHD modes are on the electron gyroscale $k_y \rho_\mathrm{e} \sim 1$, LHD modes are actually unstable over a broad range of wavelengths and frequencies ($\Omega_\mathrm{i} < \omega \leq \Omega_\mathrm{LH}$). Several of the early simulation papers on the LHDI report longer-wavelength electromagnetic instabilities near the center of the sheet after the saturation of the short-wavelength modes (Winske, 1981; Tanaka and Sato, 1981). Two explanations for these waves were recently proposed, one based on a new approach to the nonlocal linear stability (Daughton, 2003) and another based on the nonlinear excitation of a drift resonance between LHD modes generated at the edge of the current sheet and meandering ions at the center of the current sheet (Silin and Büchner, 2003a). Both predict that longer-wavelength LHD modes with wavelengths intermediate between the electron and ion gyroscale $k_y \sqrt{\rho_\mathrm{i} \rho_\mathrm{e}} \sim 1$ can penetrate into the central region, whereas the fastest growing modes with $k_y \rho_\mathrm{e} \sim 1$ are confined to the edge of the current sheet. These new predictions have been confirmed in two dimensions by fully kinetic particle-in-cell (PIC) simulations at high mass ratio (Daughton, 2003).

Figure 3.31 demonstrates these effects, showing the current density $j_y(y,z)$ from a 2D PIC simulation at a realistic mass ratio for a hydrogen plasma, $m_\mathrm{i}/m_\mathrm{e} = 1836$ (Daughton, unpublished). The initial state is a thin Harris sheet with parameters

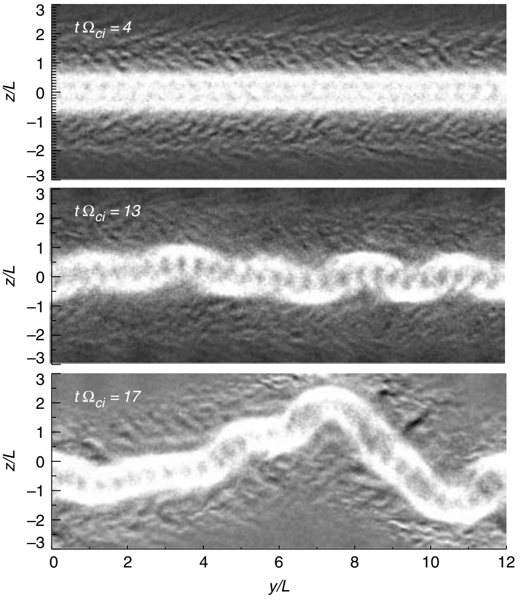

Fig. 3.31. Evolution of the current density $j_y(y,z)$ (grayscale) from a 2D PIC simulation at realistic mass ratio for a hydrogen plasma, $m_\mathrm{i}/m_\mathrm{e} = 1836$. The three panels demonstrate the transition from the saturation of the fastest growing, short-wavelength, LHD modes with $k_y \rho_\mathrm{e} \sim 1$ (top) through intermediate-scale ($k_y(\rho_\mathrm{i}\rho_\mathrm{e})^{1/2} \approx 0.8$) modes (center) to long-wavelength ($k_y L \approx 0.5$) ion–ion kink instability (bottom).

$\rho_i/L = 2$, $T_i = T_e$, $\omega_{pe}/\Omega_e = 4$ with a background density of $n_b/n_0 = 0.1$ and box size $12L \times 12L$, where L is the current sheet half-thickness. The grid size is 1024×1024 with 150×10^6 computational particles for each species and a time step of $t\Omega_e = 0.03$. At early time, $t\Omega_i = 4$ (top), the fastest growing, short-wavelength, LHD modes with $k_y \rho_e \sim 1$ have saturated leading to the turbulent fluctuations on the edge of the current layer. At intermediate time, $t\Omega_i = 13$ (middle), growth of the intermediate scale $k_y(\rho_i \rho_e)^{1/2} \approx 0.8$ LHDI is clearly evident in the growing $m = 5$ structure, while at late time, $t\Omega_i = 17$ (bottom), a long-wavelength $k_y L \approx 0.5$ ion–ion kink instability is observed in conjunction with the intermediate LHDI (see also Karimabadi *et al.*, 2003b, and Section 3.5.4).

These simulations have shown that for a current sheet thickness near or less than the ion inertial length, LHD modes may penetrate and modify the central region of the current sheet, initiating long-wavelength modes that saturate at large amplitudes. Similar results have been found by Vlasov-code simulations in three dimensions, but with smaller mass ratio (Silin and Büchner, 2003b). This suggests the possibility that these fluctuations may influence the development of magnetic reconnection. Consistent with these results, Silin and Büchner (2005a) also found that the growth rate increases with the sheet thinning as shown in Fig. 3.32.

It is important to note that the penetration of longer-wavelength LHD modes into the central region appears to require very thin current layers $L \lesssim 0.6\rho_i (\rho_i/L > 1.6$, see Fig. 3.32). Although current sheets in this parameter regime are clearly observed in laboratory plasmas (Yamada *et al.*, 2000; Ji *et al.*, 2004), current layers observed in the magnetosphere are only occasionally that thin (André *et al.*, 2004) but typically somewhat thicker $L \gtrsim \rho_i$. In this parameter regime, the theoretical results consistently predict that the LHDI is confined to the edge region of the current layer, where it is in the wrong location to directly produce the anomalous resistivity needed for reconnection. However, recent explicit 2D kinetic simulations for this parameter regime, using the realistic ion to electron mass ratio $m_i/m_e = 1836$, indicate that the LHDI may, nevertheless, play an important role in the onset of magnetic reconnection (Daughton *et al.*, 2004; Ricci *et al.*, 2004a). Although the unstable LHDI modes

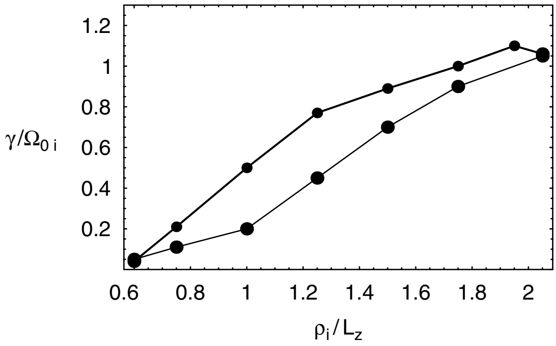

Fig. 3.32. Dependence of the global current-aligned mode (thick line) and tearing-mode instability (thin line) growth rates on the current sheet thickness. After Silin and Büchner (2005a).

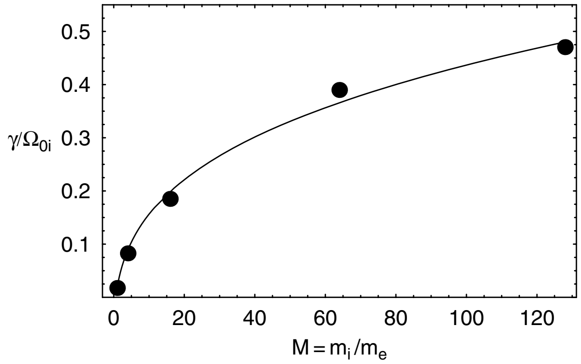

Fig. 3.33. Mass-ratio dependence of the current-aligned mode. Büchner and Kuska (1998a).

are clearly localized on the edge of the layer in these simulations, the nonlinear evolution induces a dramatic bifurcation of the current density and leads to significant anisotropic heating of the electrons in the central region of the sheet. The essential physics involves a resonant scattering of the crossing ion orbits into the noncrossing region of phase space which creates an electrostatic potential structure across the layer. The basic predictions from this model are in good agreement with observations concerning the electron flow velocity, bifurcated current structure and the electron anisotropy.

Since most of the kinetic simulations necessarily still use artificially small ion–electron mass ratios, the mass-ratio dependence of the nonlinear simulation results was investigated by Büchner and Kuska (1998a). Figure 3.33 shows that the growth rate increases mainly for small mass ratios and then saturates towards the realistic mass ratio of 1836.

3.5.3 Lower-hybrid drift instability in non-antiparallel fields

Huba *et al.* (1982) first theoretically considered the lower-hybrid drift instability in non-antiparallel reversed fields. Indeed, while not changing the current sheet equilibrium, a uniform externally imposed current-aligned magnetic guide field introduces a serious change in the current sheet instabilities. While in the generic Harris (1962) sheet with antiparallel magnetic fields the particles crossing the current sheet center may be nongyrotropic and therefore may easily become accelerated by electric fields of unstable modes, in the presence of the guide field this is no longer the case (Büchner and Zelenyi, 1991). Thus, the Hall currents, which play an important role in collisionless reconnection of antiparallel fields, are suppressed in the configurations with sufficiently large guide fields. Also, the structure of the reconnected magnetic field lines changes from closed O-type field lines in the case of antiparallel reconnection to helical (corkscrew) type in the presence of the guide field, i.e., there are no classical X- or O-points as in two-dimensional reconnection (Büchner, 1999).

For the case of finite guide fields Galeev *et al.* (1985) and Kuznetsova and Zelenyi (1985, 1990a) proposed obliquely propagating nonlinearly unstable *drift-tearing* modes, which could lead to stochastic reconnection. Indeed, in the presence of guide fields, tearing-mode reconnection islands cannot grow coherently to large amplitudes due to the rotation of the wave vector with increasing distance from the central plane. Instead, the authors proposed that small-scale reconnection coupled to a drift mode would lead to *magnetic percolation* (Kuznetsova and Zelenyi, 1990b). These drift-tearing modes, which cause small-scale reconnection, become unstable first near the current sheet center, where they resemble the classical tearing instability. Later, oblique modes arise further away from the current sheet center. The authors speculated that after the magnetic field perturbations exceed a critical level, magnetic islands overlap and the small-scale reconnection might even grow algebraically with time to large amplitudes (Galeev *et al.*, 1985).

Pressure-gradient-driven unstable LHD waves always propagate perpendicular to the local magnetic field (Krall and Liewer, 1971; Liewer and Krall, 1973; Huba *et al.*, 1977). To investigate their possible consequences for reconnection, Silin and Büchner (2003b) recently reconsidered the influence of a guide magnetic field on the resonant LHDI. They found that the unstable LHD waves become decoupled from each other in the presence of the guide field, because they always propagate perpendicular to the local magnetic field. The number of resonant ions becomes smaller as the guide field becomes stronger, and hence the resulting growth rate of the combined mode decreases as well (see Fig. 3.34). Silin and Büchner (2005b) investigated the LHDI in a rotating magnetic field, typical for magnetopause current sheets. They found that in their model the instability saturates at low levels, unable to provide a sufficient amount of anomalous resistivity.

3.5.4 Kink instability

Kink modes are frequently observed in thin current sheets in the magnetotail (e.g., Sergeev *et al.*, 2003, 2004); however, their relation to reconnection remains unclear. They may provide a means to initiate reconnection, they may be excited simultaneously but independently, or they may grow as a consequence of reconnection. Here we discuss particularly their potential role in the initiation of reconnection.

The drift-kink instability is a long wavelength $k_y L \lesssim 1$ electromagnetic mode driven by the relative drift between ions and electrons. It was originally uncovered from fully kinetic simulations of current sheets (Ozaki *et al.*, 1996; Pritchett and

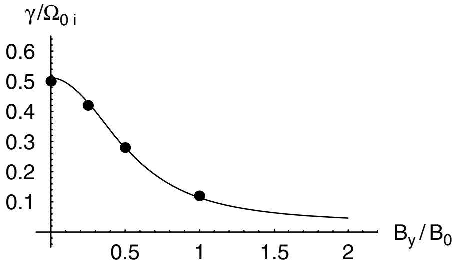

Fig. 3.34. Growth rate of the nonlocal long-wavelength LHDI at the center of the current sheet with a finite guide field B_y for $L = \rho_\mathrm{i}$.

Coroniti, 1996; Pritchett *et al.*, 1996; Zhu and Winglee, 1996; Lapenta and Brackbill, 1997) and gives rise to a large-scale undulation of the layer. Linear Vlasov theory (Daughton, 1999b) predicts substantial growth rates for the artificial mass ratios typically employed in PIC simulations $m_\mathrm{i}/m_\mathrm{e} \lesssim 100$. However, the growth rate is drastically reduced for realistic mass ratio (Daughton, 1999a,b). Comparison between the predicted theoretical scaling and fully kinetic simulations is excellent for relatively modest mass ratio $m_\mathrm{i}/m_\mathrm{e} \lesssim 100$ but deviates significantly at larger mass ratio (Daughton, 2002). The apparent reason for this discrepancy is the presence of the LHDI in these simulations which generates significant ion velocity shear which drives a kinking of the current layer by a Kelvin–Helmholtz type mode (Hesse *et al.*, 1998; Daughton, 2002; Lapenta and Brackbill, 2002; Lapenta *et al.*, 2003).

It is interesting to note that the original linear Vlasov theory of the drift-kink mode also explored the possibility of adding a uniform background plasma to the standard Harris sheet equilibrium (Daughton, 1999b). This introduces a relative drift between the current-carrying and background ion populations and the linear theory predicts large growth rates that are independent of the electron mass. This so-called ion–ion kink instability (Karimabadi *et al.*, 2003a,b) has features which are very similar to the drift-kink mode in terms of wavelength, frequency, and mode structure, but the driving factor is the relative drift between two ion populations. Within a single fluid picture the bulk fluid velocity is sheared, so the mode appears to be closely related to the Kelvin–Helmholtz instability (Hesse *et al.*, 1998) but the typical regime of interest is highly kinetic so there are important modifications. An example of the ion–ion kink mode in a PIC simulation at realistic mass ratio is shown in the bottom panel of Fig. 3.31.

To summarize, the drift-kink mode is very weak in the limit of realistic mass and is not physically interesting. However, the ion–ion kink mode has significant growth rates over a broad range of interesting parameters and is easy to excite with either shear or multiple drifting ion components. The primary stabilizing factor for the mode is the presence of a finite guide field. For the parameter regime relevant to the magnetotail, the properties of the ion–ion kink mode have been systematically examined using a combination of linear Vlasov theory (Karimabadi *et al.*, 2003a) along with full PIC and hybrid simulations (Karimabadi *et al.*, 2003b). Some of the essential properties of the ion–ion kink instability are consistent with recent magnetotail observations (Karimabadi *et al.*, 2003b; Ricci *et al.*, 2004b).

Although it has been suggested that kink instabilities may perhaps play a role in the onset of magnetic reconnection (Lapenta *et al.*, 2003), the precise mechanism by which this would occur has not been identified. To complicate matters, the LHDI is also typically present in 3D kinetic simulations, and there is now fairly convincing evidence that it does play a role in the onset. It is interesting to note that the LHDI modes can be suppressed with the introduction of a sufficient background plasma which increases the plasma β in the edge region. Recent fully kinetic 3D simulations with 20% background density have simulated the simultaneous evolution of an unstable kink mode in conjunction with collisionless tearing (Karimabadi *et al.*, 2003b). Although there are a number of interesting effects observed during the initial phase of these simulations, the final stage of evolution in these 3D simulations is quite similar to the usual 2D tearing scenario.

3.5.5 Drift-sausage instability

Sausage modes in a current sheet are symmetric modes, characterized by periodic thinning and thickening. The localized thinning makes them rather attractive as a means to initiate reconnection. However, results on the existence of such modes are contradictory, so that their importance has not been established.

A threshold of a sausage-type electromagnetic instability of a current sheet was first obtained by Yamanaka (1978), who took into account specifics of the particle motion in antiparallel fields. Neglecting electrostatic effects, Lapenta and Brackbill (1997) solved the linear dispersion relation for a drift-sausage instability based on a straight orbit integration of the linearized Vlasov equation. Their simulation, reported in the same paper, however, revealed only a kink-instability of the sheet. A nonlocal linear theory based on a full orbit integration (Daughton, 1999a, 2003) of the linearized Vlasov equation also did not find evidence for a drift-sausage mode. Likewise, the particle-in-cell simulations of current sheet dynamics listed in Section 3.5.4, which found clear evidence of kink modes, did not observe drift-sausage modes.

In contrast, Büchner and Kuska (1998a,b, 1999) investigating unstable drift-sausage modes also by means of PIC simulations, concluded that drift-sausage modes are nonlinearly unstable, the wavelength of the most unstable mode depending on the mass ratio as $k_y L_z \sim (m_\mathrm{i}/m_\mathrm{e})^{1/4}$. Wiegelmann and Büchner (2000) showed that electrostatic contributions are indeed necessary to cause a nonlinear drift-sausage sheet instability in the current flow direction. Otherwise, if the electrostatic perturbations are artificially suppressed, the tearing-mode instability dominates the current sheet decay. Considering global eigenmodes, Yoon and Lui (2001) found a preference for the sausage mode. According to Yoon *et al.* (2002), for small particle mass ratios $m_\mathrm{i}/m_\mathrm{e}$ asymmetric kink modes should dominate, while for higher mass ratios the sausage mode was more probable. Analytically considering the long-wavelength limit, Silin *et al.* (2002) demonstrated that for the correct consideration of the electrostatic (charge-separation) effects the sausage mode can directly couple into reconnection via the current-aligned longitudinal electric field E_y at the center of the current sheet. The resulting reconnection perturbations have finite wave vectors k_x and k_y. This way, magnetic reconnection in thin current sheets becomes intrinsically three-dimensional, propagating together with the global current sheet instability (*reconnection wave*) as predicted by Büchner and Kuska (1996, 1998b).

Observationally, sausage modes have been identified in the magnetotail current sheet by the Cluster satellite tetrahedron (Volwerk *et al.*, 2004; Fruit *et al.*, 2004). However, the propagation direction of these modes was along the tail, rather than across. Furthermore, they seemed to be a consequence of substorm onset rather than leading into it. Therefore, the role of sausage modes in the onset of reconnection remains unclear, both theoretically and observationally.

3.5.6 Modified two-stream instability

The modified two-stream instability (MTSI) (McBride *et al.*, 1972) and the closely related ion-Weibel instability (IWI), which represents the special case of propagation along the magnetic field (Chang *et al.*, 1990), share many of the features of the lower-hybrid drift instability, including similar frequencies, growth rates and wavelengths. As discussed in Section 3.5.2, the LHDI is considered as being driven by a density gradient, has maximum growth for $\mathbf{k}\cdot\mathbf{B}=0$ and operates predominantly in the boundary layers of a current sheet. In contrast, the MTSI/IWI is considered as being driven by the cross-field drift of unmagnetized ions even in the absence of a density gradient. It is predicted to have maximum growth for oblique propagation and to operate predominantly in the region of strongest current, that is, near the center of the current sheet (McBride *et al.*, 1972; Lemons and Gary, 1977; Wu *et al.*, 1983; Chang *et al.*, 1990; Lui *et al.*, 1991; Yoon and Lui, 1993; Lui, 2004).

The distinction between the drivers is somewhat arbitrary, because in self-consistent current sheet models current-associated drifts are typically related to magnetic field and density gradients as well. Using a local approach that includes weak inhomogeneity of both density and magnetic field, Silveira *et al.* (2002) obtained a unified local kinetic treatment of these instabilities, while Yoon and Lui (2004) investigated the transition between LHDI and MTSI on the basis of certain non-Harris type current sheets with signficant $\mathbf{E}\times\mathbf{B}$ drifts, incorporating the spatial variation through varying parameters such as the plasma β and the ion drift speed. In both of these investigations, LHDI and MTSI were distinguished according to the resulting dispersion properties, particularly the wave vector direction of the most unstable modes. Thus, LHDI is predicted to be dominant for Harris-type equilibria, where the relative electron–ion drift is entirely diamagnetic, and for the low-β boundary regions of non-Harris type models (Yoon and Lui, 2004). In contrast, the MTSI is predicted to be dominant in the high-β central region of non-Harris equilibria.

It is important to note that these predictions are based on local kinetic theory which may not be applicable to the central region of a current sheet. Further investigation of these linear predictions requires a nonlocal kinetic treatment in conjunction with 2D and 3D kinetic simulations.

3.5.7 Summary and conclusions

Current investigations have shown that kinetic instabilities in model current sheets might, in principle, provide the plasma nonideality necessary for reconnection in collisionless space plasmas. While the classical one-dimensional $T_{\mathrm{e}} \gg T_{\mathrm{i}}$ ion-acoustic instability does not operate under realistic space plasma conditions, the lower-hybrid drift instability is more likely to operate and play a significant role. While it may be a source of anomalous resistivity under drastic thinning, under less stringent conditions it may alter the current sheet structure and thereby destabilize it and couple to reconnection. Kink instabilities are likely to operate, and are indeed observed in thin magnetotail current sheets (while results on sausage modes are still controversial). However, it is not clear whether and how they might affect reconnection. More realistic 3D model calculations are necessary to further clarify the relationship between current-driven, current-aligned instabilities and fast reconnection in space plasmas.

3.6 Nonthermal particle acceleration

M. Hoshino

Nonthermal particle acceleration in magnetic reconnection is a long-standing problem in cosmic plasmas. In fact, the possibility of accelerating charged particles by an electric field along a magnetic neutral line or, more generally, along a magnetic field line in reconnecting magnetic fields was the reason for introducing the concept of magnetic reconnection, although not the term, by Giovanelli (1946) as a mechanism for particle acceleration in solar flares. The relationship between flares and particle energization by reconnection has been widely recognized after Yohkoh and SOHO observations (e.g., Tsuneta *et al.*, 1992; Sterling *et al.*, 2000). RHESSI observations reported substantial electron acceleration and a double power-law X-ray spectrum in association with flares (Lin *et al.*, 2003).

In the astrophysical context, it is known that almost all young stellar objects emit X-rays with light curves that are quite similar to those of solar flares, characterized by a fast rise and exponential decay, even though the luminosities are very much higher than those of solar flares (Koyama *et al.*, 1996; Montmerle *et al.*, 2000). Furthermore, a good correlation between the emission measure and the plasma temperature can been seen (Feldman *et al.*, 1995; Shibata and Yokoyama, 1999). Therefore, those flares are believed to be related to magnetic reconnection.

Pulsars and their surrounding nebulae are another example of magneto-active objects, and ultra-relativistic particles are known to be generated in the form of synchrotron radiation. The shock acceleration by the interaction of a relativistic pulsar wind with the nebula is the most widely accepted scenario of generation of ultra-high energy particles (Kennel and Coroniti, 1984), but magnetic reconnection is also suggested as another important acceleration process in a *striped magnetic field* in pulsar winds (Coroniti, 1990; Lyubarsky and Kirk, 2001). In fact, on the basis of Chandra X-ray satellite observations, Mori *et al.* (2004) concluded that magnetic energy dissipation is necessary to explain the luminosity of the synchrotron radiation in the Crab nebula. Zenitani and Hoshino (2001, 2005) and Jaroschek *et al.* (2004) suggested that ultra-relativistic particles can be quickly generated by relativistic reconnection.

In most cosmic plasmas, the nonthermal, high-energy spectra are often described by a power-law energy spectrum. Over the last several decades, considerable effort has been devoted toward understanding the formation of such high-energy power laws and the origin of nonthermal particles in reconnection. However, there are many outstanding questions regarding particle acceleration that motivate continuing research in the field. Plasma heating and acceleration in magnetic reconnection is now a frontier subject of plasma astrophysics. In this section, we review the physics of particle acceleration in reconnection by focusing on the Earth's magnetosphere where many key observational data are available. Since the underlying basic physics of reconnection should be universal, it can be expected that properties of reconnection and particle acceleration in the well-studied terrestrial magnetosphere are applicable to other astronomical objects, too.

3.6.1 Basic plasma parameters in the magnetosphere

Before discussing observations of energetic particles, it is useful to discuss typical thermal plasma properties in the terrestrial magnetosphere and specifically the magnetotail. We focus on the tail region around 20 to 30 $R_{\rm E}$ distance from Earth where near-Earth reconnection related to substorms is now believed to occur (e.g., Hones, 1979; Nishida *et al.*, 1981; Baumjohann *et al.*, 1991; Nagai *et al.*, 1998).

The ion temperature is always higher than the electron temperature; typical values are a few keV and several hundred eV, respectively. This preferential ion heating is believed to be associated with the primary magnetotail acceleration mechanism at the boundary between the lobe and the plasma sheet.[3] The plasma sheet density is $0.1 \sim 1\,{\rm cm}^{-3}$, but during an active reconnection period the density may decrease below $\sim 0.01\,{\rm cm}^{-3}$ in the vicinity of an X-type neutral line. The gas pressure of the hot plasma inside the plasma sheet balances the magnetic pressure of the very tenuous lobes with a magnetic field of about 20 nT. The thickness of the electric current sheet which supports the antiparallel lobe magnetic field is usually about $1 \sim 3\,R_{\rm E}$, but before the onset of substorms the thickness can become as small as the ion inertia length of the order of 1000 km (e.g., Asano *et al.*, 2003).

Based on the above plasma parameters, let us estimate characteristic limits for the electric potential induced in the magnetotail. The Alfvén speed estimated by using the lobe magnetic field and the plasma sheet density is given by

$$v_{\rm A} = 620 \left(\frac{B_x}{20\ {\rm nT}}\right) \left(\frac{0.5\ {\rm cm}^{-3}}{n}\right)^{1/2}\ {\rm km/s}. \tag{3.85}$$

The reconnecting magnetic field in the plasma sheet may be approximated by

$$B_z = 2 \left(\frac{B_x}{20\ {\rm nT}}\right) \left(\frac{M}{0.1}\right)\ {\rm nT}, \tag{3.86}$$

where M is the reconnection rate, assumed to be of order 0.1. Therefore, the motional electric field during reconnection in the magnetotail can be estimated as

$$E_y = 1.2 \left(\frac{v_{\rm A}}{620\ {\rm km/s}}\right) \left(\frac{B_x}{20\ {\rm nT}}\right) \left(\frac{M}{0.1}\right)\ {\rm mV/m}. \tag{3.87}$$

Multiplying Eq. (3.87) by the scale length L of the magnetotail cross-section of about $30\,R_{\rm E}$, the maximum potential difference induced in the tail in the dawn–dusk direction becomes of the order of

$$e\phi = 240 \left(\frac{v_{\rm A}}{620\ {\rm km/s}}\right) \left(\frac{B_x}{20\ {\rm nT}}\right) \left(\frac{M}{0.1}\right) \left(\frac{L}{30\ R_{\rm E}}\right)\ {\rm keV}. \tag{3.88}$$

Thus the plasma in the Earth's magnetotail is characterized by thermal energies well below the available potential energy estimated by Eq. (3.88). On the other hand, there are many observations that show that plasma particles can be effectively accelerated to energies of 1 MeV. These energetic particles are the continuous extension of the thermal population, forming a supra-thermal tail beginning at several multiples of the thermal energy. Most energetic particles seen in the magnetotail seem to be roughly consistent with the available potential energy (see also Section 4.4.4), but the highest energy particles seem to exceed the available potential energy.

---

[3] However, a similar ratio is also found in the magnetosheath surrounding the magnetosphere (Fig. 1.5), so that an acceleration mechanism that preserves this ratio from this source region is also plausible.

3.6.2 Energetic particle observations and magnetic reconnection

Let us discuss in more detail the energetic particle observations in the Earth's magnetotail. In early satellite observations anisotropic energetic particle bursts have been reported by Sarris *et al.* (1976) and Hones *et al.* (1976). An energetic electron burst with 0.3–1.0 MeV was identified in association with a southward turning of the B_z magnetic field at $x \approx -20$ to $-30\,R_{\rm E}$ in the magnetotail (Terasawa and Nishida, 1976). The southward turning of B_z suggests that magnetic reconnection is occurring in the magnetotail, because the tail magnetic field during nonreconnection time intervals should have a northward B_z component.

Similar events were also discussed at $x \approx -30\,R_{\rm E}$ based on a survey of electrons of $\varepsilon \geq 200\,\text{keV}$ by Baker and Stone (1976, 1977), who reported that electron flux enhancements at energies $\varepsilon \geq 1\,\text{MeV}$ are usually associated with neutral sheet crossings. Sarris *et al.* (1981) reported ion distribution over the energy range 100 eV to a few MeV even though the bulk flow speed is not necessarily fast. Möbius *et al.* (1983) analyzed energetic protons of 30–500 keV and energetic electrons of $\varepsilon \geq 75\,\text{keV}$, and suggested that reconnection near an X-type neutral line is a candidate for the acceleration of the energetic particles.

Although the relationship between the energetic particles and reconnection was plausible, there was no direct evidence of energetic particle production at an X-type neutral line. The spatial extent of the region around the X-line where non-MHD processes take place is of the order of an ion inertia length, so that the observational chance of a satellite traversing this region is very rare. However, Øieroset *et al.* (2002) have recently reported the successful observation of energetic particles in the vicinity of an X-type region. As shown in Fig. 3.35, the fluxes of energetic electrons up to ∼300 keV increased approaching the diffusion region, and the energy spectrum has a power-law signature above ∼2 keV with the power-law index of −5. Since the single, power-law population is extended up to 300 keV, all energetic particles are

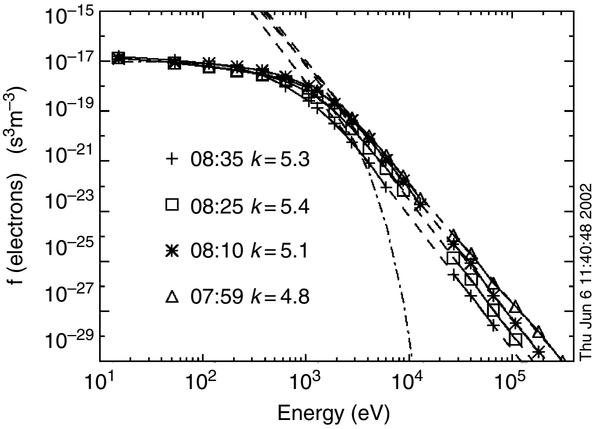

Fig. 3.35. Electron energy spectra observed just on the tailward side of an X-type region. The power-law indexes k of four different time periods are shown in the plot. Adapted from Øieroset *et al.* (2002).

thought to be generated in the same acceleration process. The high-energy electrons of ~ 300 keV seem to be consistent with the available potential energy estimated by Eq. (3.88).

The maximum available potential energy, however, may be overestimated, because the reconnection region is believed to be localized within a few Earth radii in the y direction (e.g., Angelopoulos *et al.*, 1994), so that such a large electric potential of $e\phi \sim 240$ keV is not easily induced. The relationship between the observed maximum energy and the available potential energy remains a controversial issue.

Another important issue is the distribution of the energetic particles. In association with magnetic reconnection in the magnetotail, plasma is transported away from the X-type region. During the plasma transport, ions/electrons are drifting toward dusk/dawn and should gain energy. As shown in Fig. 3.36, however, this is not supported by observations. Figure 3.36 shows suprathermal particle observations by the Geotail satellite in the tail (Imada *et al.*, 2002). Electron fluxes of 3.2 keV (right-bottom) and 9.3 keV (left-bottom), the integrated electron flux of energies greater than 38 keV (left-top), and the energetic ion flux of 39.5 keV (right-top) are shown as a function of the dawn–dusk position. The nominal electric field is directed toward the positive y axis, which is the dawn to dusk direction. One can observe asymmetry of the energetic particle distributions, but this asymmetry is not very distinct. We can find the energetic electrons (protons) even in the dusk (dawn) side region. The observed energetic

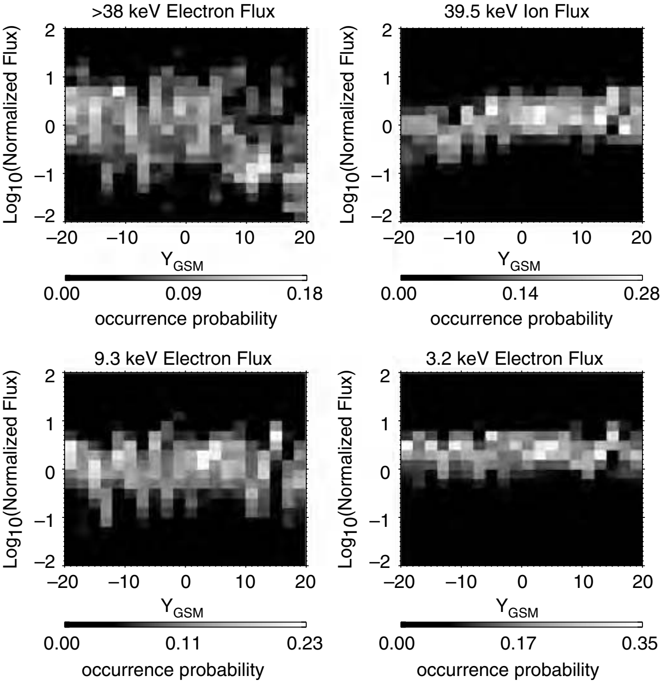

Fig. 3.36. The dawn–dusk distribution of energetic particles. The gray scale shows occurrence probability of particle flux in each $\mathrm{Y_{GSM}}$ bin.

particle distribution is not simply described by a model of the dawn–dusk potential energy gain. A possible explanation is that diffusion processes of particles play an important role in the magnetotail. If the spatial diffusion in the dawn–dusk direction is effectively occurring, the asymmetry of the energetic particle distribution will be smeared out. There is no energy gain during the diffusion process caused by elastic scattering, because the potential energy gain/loss can be compensated by the energy loss/gain from the waves whose scattering centers are embedded in the convecting plasma. In this case, the maximum energy of particles might even exceed the available potential energy under the reconnection acceleration with the diffusion process.

3.6.3 Acceleration of test particles under MHD reconnection fields

The direct energization of charged particles in reconnection is provided by the interaction of the particles with an electric field around the X-type region. In the earliest exploration of particle acceleration during reconnection, people used test particle modeling, where a model of the spatial variation of the time-dependent magnetic and electric fields is given, and they calculated the particle motion and its energization by integrating the Lorentz equation in time. The test particle calculations based on the magnetic and electric field structure obtained by a resistive MHD simulation demonstrated the production of suprathermal particles by moving in the direction of the electric field over a substantial distance (e.g., Sato *et al.*, 1982; Scholer and Jamitzky, 1987; Birn and Hesse, 1994). Time-dependent, strong electric fields generated near the X-type reconnection region in association with a pair of slow shocks are demonstrated as a primary energy source of the reconnection acceleration. In addition to the above acceleration mechanism, Ambrosiano *et al.* (1988) suggested that small-scale MHD turbulence generated in the plasma sheet under a high magnetic Reynolds number enhances the particle acceleration through stochastic scattering.[4]

Frequently, reconnection is considered to evolve in a steady-state manner, with the amplitude of the reconnection electric field more or less constant in time. But it is also postulated that reconnection is nonstationary, and in such a nonsteady reconnection regime the particle acceleration efficiency may be boosted up. Sakai and Ohsawa (1987) discussed a driven reconnection scenario by assuming that the lateral magnetic influx increases in time, and showed the transition to explosive reconnection. Bulanov and Sasorov (1975), Zelenyi *et al.* (1984, 1990), and Deeg *et al.* (1991) have demonstrated the formation of a power-law type energy spectrum from inductive electric fields that grow exponentially in time.

While the above theoretical studies of particle acceleration basically assume that the main acceleration occurs around an X-type region, a more general current sheet may involve multiple X-points in a filamentary current sheet, which also implies intervening magnetic islands with O-points. The magnetic islands might play an important role in trapping particles inside the islands, and if a finite electric field

---

[4] In Section 4.4 we will discuss test particle simulation results that indicate that, in the geomagnetic tail, betatron or Fermi-type acceleration in the collapsing magnetic field earthward of an X-type neutral line may be more significant than the acceleration in the immediate vicinity of the neutral line.

exists over the plasma sheet, strong particle acceleration can be expected in and around the magnetic islands as well (Kliem, 1994).

3.6.4 Turbulence and wave scattering

Processes responsible for nonthermal high-energy particles are likely to violate adiabatic particle motion, and several waves may contribute to nonadiabatic processes through wave–particle scattering. As noted in Section 3.6.2, the energetic particle distributions do not show clear dawn–dusk asymmetry in the magnetotail, which may be suggestive of a diffusion process across the magnetic field. There has been accumulating evidence that the plasma sheet is in a turbulent state (e.g., Kennel, 1995), and the electric and magnetic field turbulence is believed to be the primary mechanism by which heating and dissipation takes place through scattering of particles.

The frequency band of the turbulence ranges from below the ion cyclotron frequency (of the order of 0.1 Hz in the Earth's magnetotail) to the plasma frequency (of the order of 10 kHz). The observed Fourier power spectral density of the magnetic fields can be approximated by a double power-law spectrum in the MHD range (Hoshino *et al.*, 1994; Bauer *et al.*, 1995). Above MHD frequencies, three different types of wave modes are observed (Gurnett *et al.*, 1976). The most intense waves are broadband electrostatic noise bursts observed in the outer plasma sheet boundary layer (PSBL) in association with large plasma flows, the other two are whistler mode magnetic noise bursts and electrostatic electron cyclotron waves. The whistler waves are also observed in the same region as the broadband electrostatic noise, and are thought to be associated with regions carrying substantial field-aligned currents.

Concerning the large number of waves observed in the Earth's magnetotail, we briefly mention the current understanding of two main generation mechanisms. In the outer plasma sheet boundary regions, an anisotropic ion beam velocity distribution function is often observed during the reconnection phase. The distribution consists of cold incoming ions streaming toward the diffusion region and accelerated outgoing ions. The outgoing ions are thought to be generated in the diffusion region and to be ejected along the reconnecting magnetic field lines (e.g., Hoshino *et al.*, 1998). This outgoing distribution is called the PSBL ion beam. It is expected that the PSBL ion beams can excite Alfvénic/whistler waves propagating along the magnetic field due to the firehose/ion beam cyclotron instability. Arzner and Scholer (2001) performed a large-scale hybrid simulation of reconnection and demonstrated the generation of the PSBL ion beams and the emission of the Alfvénic/whistler waves in the plasma sheet boundary layer, which in turn lead to the evolution of MHD turbulence and the resultant ion thermalization.

Inside the plasma sheet and around the plasma sheet boundary, broadband waves with frequencies from the lower-hybrid frequency to the plasma frequency are also believed to be important for particle scattering (Okada *et al.*, 1994; Cattell *et al.*, 1994). Modern, high-time-resolution satellite measurements show that the broadband electrostatic waves are localized, large-amplitude, electrostatic waves with a series of coherent wave forms, now called *ESW* (Kojima *et al.*, 1994). The scale of ESW is probably tens of electron Debye lengths, but the amplitude is 10 to 100 times that of a large-scale reconnection electric field induced by the global MHD flow (Cattell *et al.*, 1999). Therefore, the small-scale ESW might appear to control the global dynamics including the electron heating and acceleration. The emission mechanism may be attributed to the electron beams generated around the diffusion region in a similar way to the PSBL ion beams, and the waves are excited by either electron bump-in-tail instability (Omura *et al.*, 1994) or Buneman instability (Drake *et al.*, 2003).

3.6.5 Strong acceleration during reconnection

As stated in Section 3.6.3, the earliest particle acceleration studies were done in the framework of prescribed fields or fields computed from resistive MHD reconnection models. It is important to explore the particle acceleration in a self-consistent system of a full particle simulation where the feedback of particle motions via the electric current into the electric and magnetic fields is taken into account. Larger amplitude waves could be generated through kinetic instabilities in the collisionless plasma system. As discussed earlier, the thickness of the plasma sheet is known to become as small as the ion inertia scale before onset of magnetic reconnection, and the plasma sheet that governs the macrodynamics also governs the microscale phenomena. Therefore the microscale plasma dynamics will strongly couple with the macroscale physics. Then we need kinetic modeling of particle acceleration beyond the MHD description. Here we discuss energetic electron acceleration processes obtained by using a full-particle simulation (Hoshino *et al.*, 2001b).

This particle simulation was carried out in two-dimensional (x, z) coordinate space, assuming the Harris solution (Harris, 1962) as the initial condition. In the early phase, a localized external electric field drives the evolution from the outer boundary to initiate reconnection in the center of the simulation box. As time goes on, an X-type neutral line is formed, and in association with the energy conversion from magnetic to kinetic energy, the reconnection outflow in the plasma sheet is ejected from the X-type neutral point. In contrast to resistive MHD models, the energy dissipation around the X-type magnetic diffusion region is provided by particle inertia due to inverse Landau resonance of particles with the reconnection electric field and by the resultant electron pressure anisotropy (Section 3.2).

Figure 3.37 shows a snapshot of the nonlinear evolution of reconnection at $t/\tau_{\mathrm{A}} \sim 48.8$, where τ_{A} is the Alfvén transit time for crossing the plasma sheet. The top panel shows magnetic field lines in the x, z plane (i.e., the reconnection plane), and the bottom panel shows the magnetic field component perpendicular to the reconnection plane B_z, which is generated by Hall electric currents in the thin plasma sheet (Section 3.1).

Figure 3.38 shows energy spectra of electrons integrated over all pitch angles in the whole simulation domain. In the early phase of reconnection before $t/\tau_{\mathrm{A}} \sim 41.7$, we find that the electrons are gradually thermalized with time, and the spectra are approximated by a thermal Maxwellian. In the late phase at $t/\tau_{\mathrm{A}} \sim 48.8$, the enhancement of suprathermal electrons above the thermal Maxwellian can be clearly seen. By analyzing the positions of those energetic particles, we found that most energetic electrons of $\varepsilon_{\mathrm{ele}}/(m_{\mathrm{e}}c^2) \geq 0.1$ are situated in the X-type region and around the boundary between the lobe and the plasma sheet, i.e., around the separatrix of reconnecting magnetic field lines.

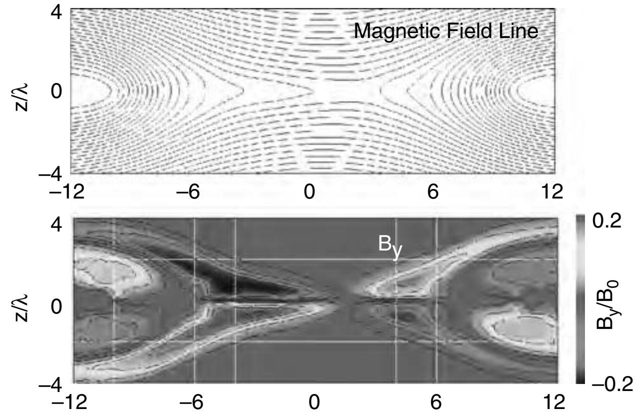

Fig. 3.37. Magnetic field lines in the x, z plane (top) and the contour of the Hall current generated magnetic field B_y (bottom), at $t/\tau_A = 48.8$.

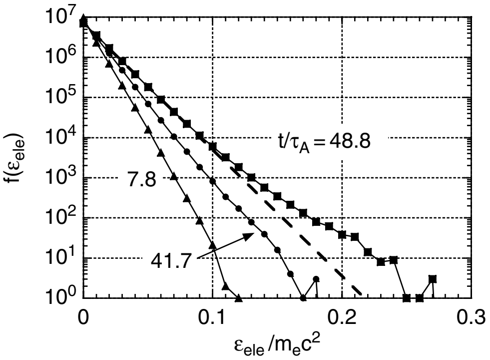

Fig. 3.38. Evolution of electron energy spectra at $t/\tau_A = 7.8, 41.7, 48.8$. The dashed line shows the Maxwellian fit as reference.

In order to understand how and where the electrons get their energies, we have analyzed electron trajectories in the reconnection region. Figure 3.39 shows several typical trajectories. The starting points of the trajectories are denoted S1, S2, etc., while the end points are labeled E1, E2, etc. The S1–E1 curve is one of the most typical orbits showing particle acceleration. The electron is initially accelerated near the X-type region by moving in the negative electric field direction, and is ejected along the magnetic field line at the separatrix boundary. The particle with the S2–E2 trajectory gains much larger energy than the S1–E1 electron does, during several bounce motions in the reconnecting magnetic fields with mirror geometry. The energy gain is provided by the curvature and ∇B drift motions toward the negative y direction. It is important to note that the ratio between the magnetic field curvature radius and the gyroradius, κ, is almost unity in the central plasma sheet, and that a particle with $\kappa \sim 1$ is effectively scattered toward a weak magnetic field region, and has a tendency to stay for a longer time in the plasma sheet (e.g., Delcourt *et al.*, 1996).

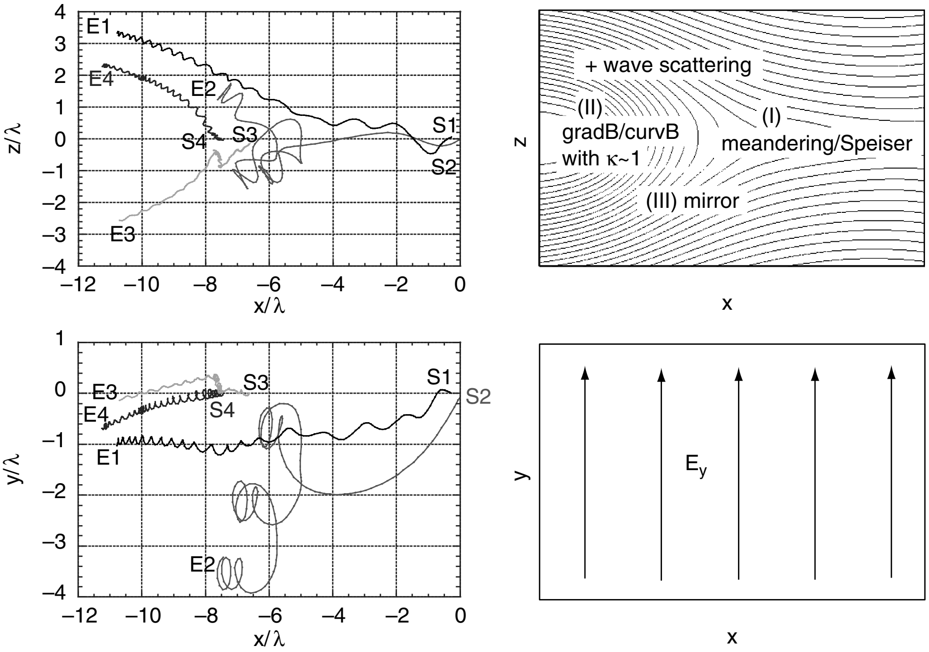

Fig. 3.39. Typical electron trajectories obtained in a particle-in-cell simulation. The left panels show trajectories in the x, z plane (top) and in the x, y plane including the reconnection motional electric fields E_y (bottom). The right-hand panels are a schematic view of the magnetic field lines in the x, z plane and the electric field in the x, y plane.

The S3–E3 trajectory around $x/\lambda = -7.5$ is an example of the cross-field diffusion. The electron is scattered towards the stronger magnetic field region and the positive electric field y direction. The orbit S4–E4 shows pitch-angle scattering, with a change of the pitch of the gyromotion around $x/\lambda = -8$ and -10. We suggest that these trajectories represent the basic scattering processes that play important roles in particle acceleration.

Figure 3.40 shows the wave spectra obtained in the magnetic field pile-up region, where the reconnection outflow plasma collides with the pre-existing plasma. The vertical and horizontal axes are the wave power of $(E_x^2 + E_z^2)$ and the wave frequency, respectively. The wave power is normalized by $(v_{\mathrm{A}} B/c)^2$, and the wave frequency is normalized by the electron plasma frequency at the plasma sheet at $t = 0$. The spectrum denoted by the dashed line is taken at the boundary between the lobe and the plasma sheet at $(x/\lambda, z/\lambda) = (-7, 2)$, while the solid line is the spectrum inside the plasma sheet at $(x/\lambda, z/\lambda) = (-7, 0)$. Inside the plasma sheet, we find that the low-frequency waves are strongly enhanced. Around the plasma sheet boundary layer, a broadband spectrum from the low frequency to the plasma frequency can be seen. The spectrum bump around $\omega/\omega_{\mathrm{pe}} {\sim} 0.7$ corresponds to the local plasma frequency, i.e., Langmuir waves. Since we can see the signature of an accelerated electron beam in the distribution function taken around the boundary (Hoshino *et al.*, 2001a), the

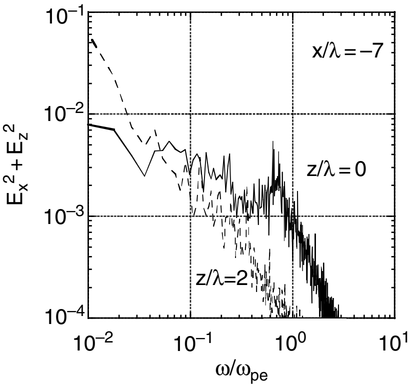

Fig. 3.40. Turbulent wave spectra obtained in the magnetic field pile-up region where the reconnection plasma outflow collides with the O-type magnetic island.

Langmuir waves are thought to be excited by the fast electron beams. The electron beams are generated in and around the X-type region due to the reconnection electric field E_y, and after their energization the accelerated high-speed electrons are ejected along the magnetic field in the boundary between the lobe and the plasma sheet, which in turn excite a strong coherent wave in the plasma frequency band probably through the bump-in-tail instability.

From the above simulation results, we can conclude the following conventional acceleration scenario. The electrons gain their energy around an X-type neutral region during the Speiser/meandering motion (Speiser, 1965; Section 4.4), and those pre-accelerated electrons are transported outward together with the reconnecting magnetic field lines. Around the magnetic field pile-up region formed by the interaction between the fast reconnection outflow and the pre-existing plasma sheet, those unmagnetized particles are further accelerated with the aid of particle scattering which breaks down the adiabatic motion (see Fig. 3.39).

So far we have discussed particle acceleration mainly for (perpendicular) electric fields in the form of the inductive/convection electric field. The electrostatic fields parallel to the magnetic fields may play an important role also, not only for wave–particle scattering but also for strong acceleration. Parallel electrostatic fields have been used to explain particle acceleration in many phenomena such as auroral electron acceleration. They are known to arise from the interruption of the parallel current due to plasma instabilities and from the formation of double layers of electric charge. Recently Drake *et al.* (2003, 2005b) explored the acceleration of particles in a configuration with a guide magnetic field. Magnetized electrons can be efficiently accelerated along the guide field, and those accelerated electrons form an electron beam, which can become faster than the electron thermal speed during reconnection. They showed that the beam electrons can drive strong electrostatic waves in the waveform of ESW in association with electron phase-space holes. The electron hole acceleration may be regarded as one class of field-aligned potential drop acceleration processes. The electron hole acceleration is not static but rather

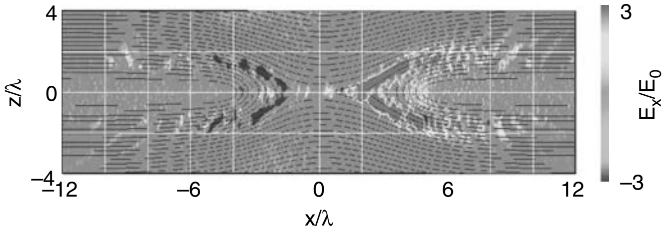

Fig. 3.41. Large-amplitude waves propagating outward from an X-type region along the magnetic field lines. The magnetic field lines and the color contours of E_x are shown, and E_x is normalized by $E_0 = v_A B_0$. See also color plate.

originates in a highly dynamic evolution during the magnetic energy dissipation phase.

A series of large-amplitude electrostatic waves was also found in a reconnection simulation without guide magnetic field. Figure 3.41 shows a snapshot of the electric field E_x obtained in the full particle simulation with a forced boundary condition. The simulation parameters are the same as those discussed in Figs. 3.37 through 3.39, but in addition finite plasma inflow was driven continuously from the top and bottom boundaries. In such a system, one can expect fast and well-developed reconnection with large-amplitude waves. In Fig. 3.41 the amplitudes of the coherent electrostatic waves E_x are found to be several times the magnitude of the inductive electric field E_y, with wavelengths intermediate between electron and ion inertia scales. For spontaneous reconnection in Fig. 3.40, we had already found a signature of Langmuir wave emission, but the amplitudes remained small. The large-amplitude waves in Fig. 3.41 are produced as the result of the nonlinear evolution of the Langmuir waves seen in Fig. 3.40.

In addition to a series of the large-amplitude electrostatic waves propagating along the outer plasma sheet boundary, we also found a pair of polarized V-shape regions near the X-type region. The electric field vectors are directed outward from the X-type region, and ambipolar electric fields are known to be produced in association with Hall electric currents in a thin current sheet (Hoh, 1966; Hoshino, 1987). In the driven system, we find a pair of polarized regions, which has stronger electric field than that seen in spontaneous reconnection, which may play an important role in acceleration. Recently, Hoshino (2005) discussed that some electrons can be trapped by the electrostatic potential well of the polarization field, and during the trapping phase electrons can gain their energies from the convection/inductive reconnection electric field due to the so-called *surfing acceleration* mechanism (e.g., Sagdeev and Shapiro, 1973; Katsouleas and Dawson, 1983). Hoshino (2005) found that relativistic electrons with MeV energies are quickly generated, and the energy spectrum shows a better-developed nonthermal tail than that seen in Fig. 3.38. Although these large-amplitude electrostatic waves are believed to be important for plasma heating and acceleration, there remain many fundamental and theoretical questions to be solved.

3.6.6 Discussions and remaining problems

From the observational and theoretical studies, it is now understood that magnetic reconnection can provide efficient acceleration of particles to suprathermal energies, but in spite of enormous progress many issues still remain unsolved. One of the important issues is whether or not reconnection can generate a power-law energy spectrum. As stated earlier, magnetic energy dissipation is believed to be important for nonthermal particle acceleration in many astrophysical applications. In the terrestrial magnetosphere, the energy spectrum is approximately given by a power law in the high-energy range with a slope of about 3–7 (e.g., Baker and Stone, 1977; Øieroset *et al.*, 2002). In solar flares where reconnection is regarded as one possible acceleration model, the power-law index of suprathermal particles is about 2.5–7 as well. In most space physics and astrophysics contexts, the production of nonthermal particles is more often attributed to the stochastic/diffusive shock acceleration (e.g., Blandford and Ostriker, 1978), because the diffusive shock acceleration can explain the ubiquitous power-law spectrum with an index of 2, which depends weakly on plasma parameters. Contrary to the diffusive shock acceleration, the reconnection acceleration seems to generate softer energy spectra from the observational point of view. Zenitani and Hoshino (2001, 2005) and Jaroschek *et al.* (2004), however, found that reconnection can produce a very hard energy spectrum with a power-law index of unity in the relativistic regime where the Alfvén speed v_A and the thermal velocity are close to the speed of light c. It is still an open question how the nonthermal energy spectrum depends on plasma parameters such as temperature and guide magnetic field, etc.

Another important issue is the spatial energetic particle distribution. The acceleration is basically provided by the inductive/convection electric field in reconnection, and a localization or spatial separation of energetic particles is expected from the fact that ions are accelerated parallel to the electric field and electrons in the antiparallel direction. However, as we stated in Section 3.6.2, dawn–dusk asymmetries of the energetic particles are not clearly seen at least up to several tens of keV. If diffusion due to wave–particle scattering takes effect substantially during acceleration, the asymmetry of the energetic particle distribution in the electric field direction is smeared out, because the potential energy gain/loss is always compensated by the energy loss/gain from the wave during the scattering. Furthermore, for wave–particle interaction, the maximum energy may even exceed the available potential energy. However, it is a controversial issue that the diffusion process plays an important role in plasma transport in the magnetotail. (Another possible explanation, discussed further in Section 4.4, is that betatron and Fermi-type acceleration in the collapsing field earthward of the reconnection site are more important than acceleration near the X-type neutral line.)

Finally we would like to comment on multiscale coupling. It is well known that electric and magnetic field turbulence act to heat the plasma through scattering of particles, but, in addition to this standard paradigm, it has been suggested that coherent, small-scale, large-amplitude electric field waves, often observed in key regions of the terrestrial magnetosphere, are responsible for electron energization. The spatial scale of the small-scale waves is several tens of Debye lengths, but the amplitudes of the waves are 10 to 100 times that of the motional electric field induced in the MHD scale. Then it is proposed that the microscale processes appear to control the global dynamics. This kind of multiscale coupling process is beginning to shed light not only on space plasma phenomena but also on high-energy astroplasma physics. These observational and theoretical studies are also the key problems of future missions such as MMS/NASA and SCOPE/JAXA that focus on the potentially rich multiscale structuring plasma phenomena that result from the coupling of the MHD scale to the scale of electron kinetics.